Development of X-ray Lithography and Nanofabrication Techniques for III-V Optical Devices

by

MICHAEL 홍열 LIM

S.B. Electrical Engineering, Massachusetts Institute of Technology (1993)
M.S. Electrical Engineering, University of Southern California (1995)

Submitted to the Electrical Engineering & Computer Science
in partial fulfillment of the requirements for the degree of

DOCTOR OF SCIENCE IN ELECTRICAL ENGINEERING

at the

MASSACHUSETTS INSTITUTE OF TECHNOLOGY

February 2002

Author . . . .
Electrical Engineering & Computer Science
October 12, 2001

Certified by . . . .
Henry I. Smith
Keithly Professor of Electrical Engineering
Thesis Supervisor

Accepted by . . . .
Arthur C. Smith
Chairman, Department Committee on Graduate Students

Development of X-ray Lithography and Nanofabrication Techniques for III-V Optical Devices

by

Michael 홍열 Lim

Submitted to the Electrical Engineering & Computer Science
on October 12, 2001, in partial fulfillment of the
requirements for the degree of
Doctor of Science in Electrical Engineering

Abstract

This dissertation covers the development of fabrication techniques for Bragg-grating-based integrated optical devices in III-V materials. Work on this rich family of devices has largely been limited to numerical analysis because of the difficulties of their fabrication. The challenges of fabrication are addressed by dividing the problem along two lines: (1) development of an advanced x-ray mask system that addresses future nanolithography needs, and (2) development of fabrication techniques that addresses problems specific to Bragg-grating-based filters. A new x-ray mask configuration is described that improves many aspects of the x-ray mask. A novel means of measuring nondestructively x-ray mask distortion on a global scale was developed, called holographic phase-shifting interferometry (HPSI). This system, in conjunction with appropriate thermal input can potentially provide active correction of x-ray mask distortion. Current microphotonic fabrication issues are presented along with a detailed description of the dual-layer hardmask process (DLHP). The development of the DLHP was specifically geared towards the special requirements of Bragg-grating based microphotonics. Taken as a whole the author hopes that this dissertation serves to facilitate the building of advanced future integrated-optical devices.

Thesis Supervisor: Henry I. Smith
Title: Keithly Professor of Electrical Engineering

Acknowledgments

Many people have helped me as I made my long journey through MIT. Hank Smith has been my advisor since I was a junior in college and through his guidance and encouragement, I have emerged a better scientist and engineer. His lab, the NanoStructures Laboratory, has been a wonderful place to work where one can always try out new and unorthodox ideas with sometimes shockingly little supervision.

The work in this thesis was built on the backs of the many people that I have been fortunate enough to meet. Collaborating with Kenichi Murooka, a visiting scientist from Toshiba, on the adaptive x-ray mask project has been a fantastic experience. Ken made invaluable contributions to the development of the x-ray mask. Tom Murphy is equally ready with a quick joke or a handy perl script. Discussions with Tom have proven valuable to many aspects of this thesis. Juan Ferrera has been my lab, office, and roommate. We have worked together on many projects both in and out of the lab. Tim Savas has always been a great sounding board for ideas. Jalal Khan has provided tremendous insight into the working of integrated optics. Being able to work with Farhan Rana on distributed feedback lasers has been both intimidating and rewarding. David Carter was always enjoyable to work with, whether it was trouble shooting a LabVIEW program or an x-ray vacuum system. Todd Hastings has been a great person with whom to work. Working on the fifth floor interferometers with Mike Walsh has been fun—I am sure that the IL system is in good hands. Mark Mondol gave me a tremendous amount of help with the sputtering system. At the beginning of my graduate school career Jay Damask provided invaluable guidance. I cannot mention enough the hard work of Jim Daley. His diligence has prevented the NSL slipping from a state of controlled chaos into a state of just-plain chaos.

I would like to thank Rajeev Ram and Tayo Akinwande for serving as readers for this thesis. They have provided many valuable comments and insights that made this thesis a stronger document and a better read. I would like to thank the Defense Advanced Research Projects Agency for having the foresight to fund such bluesky projects as optoelectronics and x-ray nanolithography. I am grateful for the award and recognition from the Lemelson Foundation.

My parents have always encouraged me and I am indebted to them. Finally, in many tough instances my wife, Stella Park, has given me the strength to will where alone I might have given up.

Contents

List of Figures

List of Tables

Chapter 1

Introduction

The central theme of this dissertation concerns the development of fabrication techniques for Bragg-grating-based integrated optical devices in III-V materials. Before proceeding any further, the most obvious question is why this topic even needs further exploration, especially in light of all the work that has come before. The short answer is that while some of the previous fabrication attempts have resulted in impressive devices, there are still the dual chasms of fabrication control and manufacturability that must be crossed.

In order to address these two issues this dissertation uses a process development paradigm that has been exploited with great success in the NanoStructures Laboratory (NSL). One first selects a device with novel and challenging fabrication requirements, then identifies the most important processing issues, and finally builds the device. This paradigm has resulted in a wide array of sub-100 nm fabrication techniques, oftentimes using advanced semiconductor devices (*e.g.* quantum-electronics, electron waveguide devices, Coulomb-blockading devices) as the selected technology driver [1, 2, 3].

As the title suggest, instead of using a semiconductor device as the technology driver, this thesis uses a Bragg-grating-based device known as a resonant channel-dropping filter (CDF), which will be discussed in chapter 3. This work is part of a broad effort to leverage the fabrication technologies of the NSL to fabricate Bragg-grating-based microphotonics in response to the explosive growth of optical telecommunications.

Optical Communications

A properly manufactured silica fiber can theoretically transmit 100 terabits [4] of data every second from one point to another. Unfortunately, accessing the full bandwidth of the optical fiber is very difficult. The most obvious technique would be to transmit the data as a stream of extremely short pulses. While the required 10 femtosecond length pulses can be generated in many labs across the world, the nonlinearities generated by such pulses would bring even the best engineered systems to its knees.

Another technique to access the bandwidth of the fiber is wavelength division multiplexing (WDM). WDM exploits the full bandwidth of the fiber by simultaneously transmitting multiple data streams, each centered at a different wavelength. While still much slower than the ultimate capability of the fiber, the data rate of the aggregate channels is beginning to approach 1 Terabit per second transmission rates through careful engineering. Companies have been very successful in exploiting WDM, with some current systems (*e.g.* Lucent Lambdarouter, Cisco 12000) able to multiplex several hundreds of gigabits onto a fiber every second. Meanwhile, several companies have been laying fiber between cities at an extremely rapid rate. It therefore appeared that we were going to soon enjoy low-cost high-speed communications. Unfortunately, due to a number of reasons, most important of which is the high cost of putting and taking data onto and off of the fiber, only 3% of the fiber is currently being used; at current rates, it is estimated that even by 2003 only 11% of the optical-fiber capacity will be in use [5].

Moreover, while an impressive feat of technology, simple point-to-point transmission has only limited utility. A more useful network must have the ability to flexibly and rapidly direct traffic from any source to any destination. This switching should be performed while minimizing the amount of time the optical datastream spends as an electronic datastream; ideally a system would be able to direct traffic without ever having to convert from optical to electronic. Figure 1-1 illustrates the difference between the two networks. An interconnected WDM network would require the ability to add and/or drop signals at selected wavelengths. This sort of ability can be readily accomplished using Bragg-grating-based filters.

Bragg-Grating-Based Devices

The term “Bragg grating” refers to an optical device in which a periodic index modulation or structural corrugation reflects light in a narrow wavelength range. The principle of operation is similar to that of a dielectric mirror, in which a periodic sequence of films, of alternating index, is used to achieve high reflectivity over a narrow bandwidth; we shall exploit the relationship between a grating and a dielectric film more fully in chapter 4.1.

Because of their ability to selectively reflect certain wavelengths, Bragg gratings find widespread application in the rapidly growing field of optical telecommunications, especially in wavelength-division multiplexing (WDM). For example, in distributed-feedback lasers, Bragg gratings are used in place of mirrors or facets to provide wavelength-dependent feedback into the lasing medium [6]. Fiber Bragg gratings, in which a periodic index modulation is induced in the core of a photosensitive optical fiber, are now employed for a variety of applications, including dispersion compensation and wavelength add/drop filters [7].

Moreover, relatively sophisticated optical filters can be constructed using Bragg gratings. By changing the pitch and/or modulation depth of the grating across the length of the device, it is possible to tailor the spectral response of the device. Also, by introducing one or more quarter-wave shifts into the grating, it is possible to construct a rich variety of resonator-based filters, from simple Lorentzian bandpass filters to higher-order Butterworth filters [8, 9].

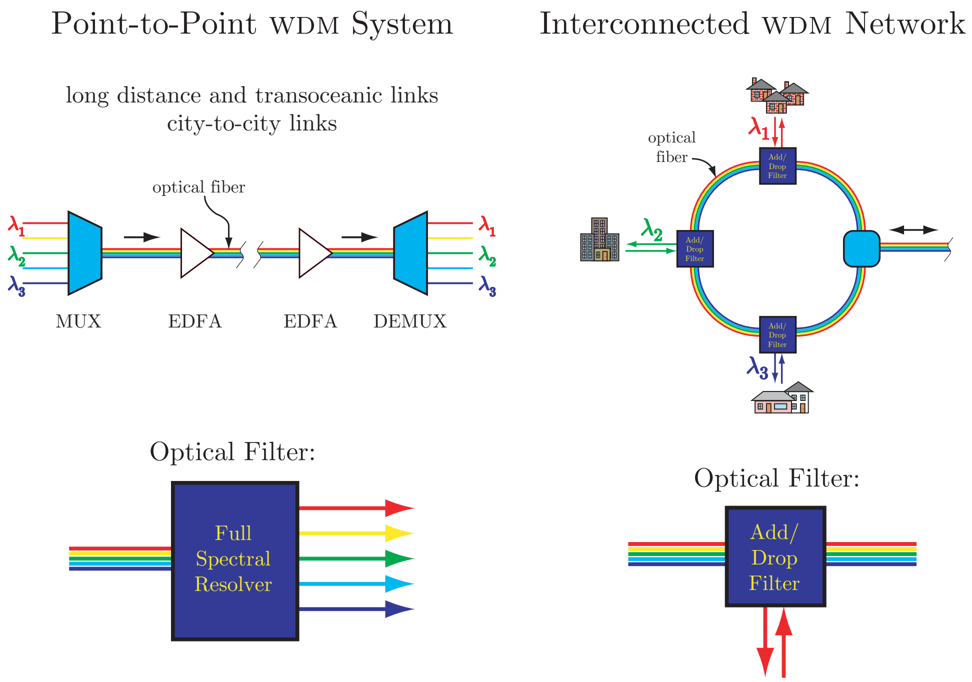

Figure 1-1: Wavelength division multiplexing (WDM) can be used to increase the throughput of simple point-to-point networks. Such systems would use an optical filter device that would fully multiplex and demultiplex the optical signal. A more flexible system would consist of an interconnected WDM network. Such a system would be able route desired signal around the network using an optical filter device that can add and/or drop selected optical wavelengths.

Year	*1999*	*2000*	*2001*	*2002*	*2003*	*2004*	*2005*	*2008*	*2011*	*2014*
Technology Node	*180 nm*			*130 nm*			*100 nm*	*70 nm*	*50 nm*	*35 nm*
Half pitch (nm)	180	165	150	130	120	110	100	70	50	35
Contacts (nm)	200	185	170	150	145	140	130	100	70	50
Overlay (nm, mean + 3σ)	65	58	52	45	42	38	35	25	20	15
CD control (nm, 3σ post-etch)	18	17	15	13	12	11	10	7	5	4

Solutions Exist ☐ *Solutions Being Pursued* 🟨 *No Known Solution* ⬛

Table 1.1: The Semiconductor Association (SIA) roadmap shows the requirements for future lithography for the case of dynamic random access memory (DRAM). This shows the progression of the present day pitch of 300 nm to the ultimate pitch of 70 nm. It should be noted that even though the entire roadmap shows lithography solutions as *being pursued* the primary technology effort for the finest features, *i.e.* extreme ultraviolet (EUV), will fail.

Despite the sophistication flexibility afforded by Bragg gratings, their application in integrated-optical devices has been limited to relatively simple components, in part because of the technical challenges in fabricating such structures. If the functionality and integration-level of microphotonics is to keep pace with the need for future increases in network capacity, *i.e.* if components are to be made that enable the economical use of optical fiber capacity, a concerted effort must be made towards developing an extendable manufacturing technique. The solution to this challenge is planar fabrication.

Planar Fabrication

The entire semiconductor device industry relies on the planar fabrication process to reliably manufacture billions of transistors every year. In this process, one first coats a substrate with a radiation sensitive polymer (called *photoresist*), which is then illuminated with photons or electrons in selected regions; this illumination step is called *lithography*. The lithography step serves to alter the chemical structure of the polymer so that one can next dissolve away the selected portions of the photoresist using a *developer*. With the desired pattern now residing in the photoresist, one can finally use any number of techniques to transfer this pattern into the substrate. These steps are repeated several times in order to make a complete semiconductor device. Figure 1-2 illustrates the major steps of the planar fabrication process.

Continual refinement of the planar fabrication process has enabled extraordinary advances in processor speed, memory density, and computer functionality. In 1971, the minimum feature size of a transistor was 10 μm—this has been driven down to 0.18 μm in present-day devices. The Semiconductor Industry Association (SIA) roadmap, summarized in table 1.1, continues this drive down to 35 nm. This relentless development has left a wake of numerous highly specialized technologies, many of which have been exploited by fields outside of the semiconductor industry.

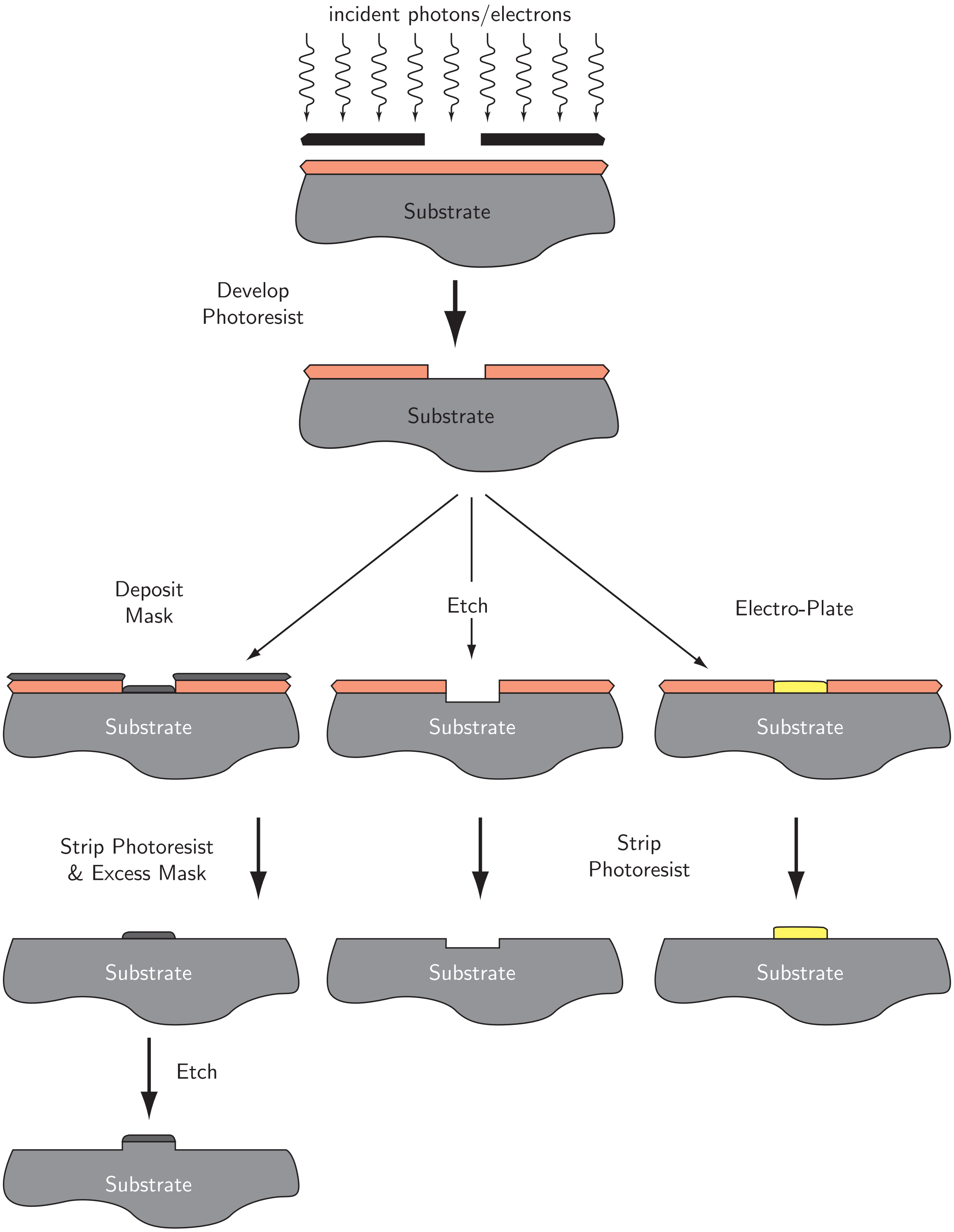

Figure 1-2: Planar fabrication begins with the lithography step which defines patterns. After the patterns are defined in photoresist, any number of steps can be used to transfer the pattern into the underlying substrate. These steps are repeated until one forms the desired structure.

Lithography Technology

Though figure 1-2 implies that the pattern of incident photons (or electrons) are taken for granted, in actuality this initial lithography step is the most critical and difficult step of the planar fabrication process[1]. Without lithography improvements Moore's law would have been dismissed long ago as the inane ramblings of a semiconductor cheerleader.

There are a number of lithography techniques used throughout the industry, the most common being optical projection. The lithography requirements for Bragg-grating-based microphotonics in III-V materials is governed by the index of refraction, which can range from 3.17 to 3.6; this requires that the minimum feature size required ranges from 95 nm to 125 nm. As shown in table 1.1, common lithography equipment will not be able to reproduce the features necessary for Bragg-grating-based microphotonics until around 2005, if then.

Since standard industrial lithography tools are designed specifically for the fabrication of semiconductor devices, they are typically not appropriate for the fabrication of microphotonics. The advanced lithography tools that are described below have been developed in the NSL have been used in a number of advanced device efforts, and are the best lithography tools available for building microphotonics.

Optical-Proximity Lithography

During optical-proximity lithography (OPL), depicted in figure 1-3, a mask, containing the pattern in chrome, is brought in close proximity to the photoresist covered substrate. Unlike optical projection lithography, where the features on the mask are typically reduced by a factor of five, the features on the OPL mask are the same size as the features to be printed on the substrate. This type of mask referred to as a 1× mask.

A lamp shines light through the 1× mask and the chrome pattern casts a shadow over the substrate. OPL is the simplest lithography technique, though if used with great care it is capable of reproducing extremely fine features. More typically, one uses OPL to print features that are larger than 1 μm.

The advantage of OPL is its simplicity and speed. The photomasks can be quickly generated by a number of vendors. If the patterns are larger than 100 μm the masks can be generated at a printshop using standard photo-offset printers.

Interferometric Lithography

Interferometric lithography (IL) has been used in the NSL to produce gratings since 1973. Figure 1-4 shows the IL system in the Space Nanostructures Laboratory (SNL) that has been used to produce grating with a pitch as fine as 200 nm. The SNL IL system splits a laser beam (wavelength λ=351 nm) and forms two mutually coherent

---

[1] Lithography was first used by the Hohokam tribe in the American southwest to decorate shells, stones, and rocks. One could easily argue that this was the first commercially successful lithography technique since the decorated objects were most certainly of higher value than the plain objects. It is unclear whether the detail of their artwork doubled every 18 months.

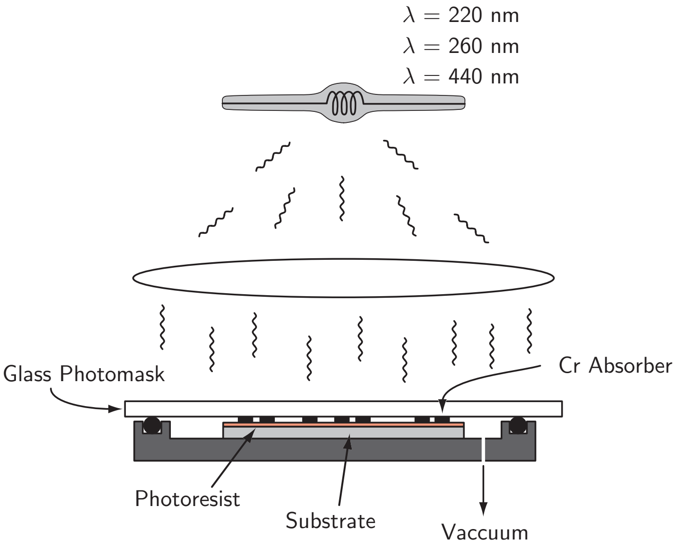

Figure 1-3: Optical proximity lithography is the simplest lithography technique. As practiced in the NSL, a lamp (with a choice of wavelengths) shines light through a mask consisting of glass (or quartz) plate with a Cr pattern. The pattern casts a shadow onto the photoresist-covered substrate. If used with great care, it is capable of producing extremely fine features though most typically one uses OPL for features that are 1 μm and larger. This tool is appropriate for defining waveguide features.

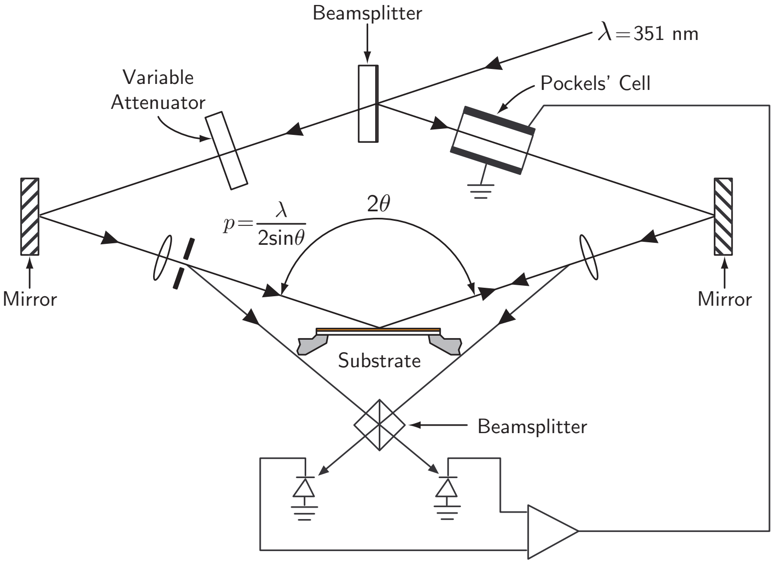

Figure 1-4: Schematic depicting the interferometric lithography (IL) system used to produce the gratings for several NASA observatories. The IL system splits a laser beam, of wavelength $\lambda = 351$ nm, forming two mutually coherent spherical waves, which then interfere at the substrate surface at a half-angle θ. The standing wave formed has a periodicity of $\frac{\lambda}{2\sin\theta}$.

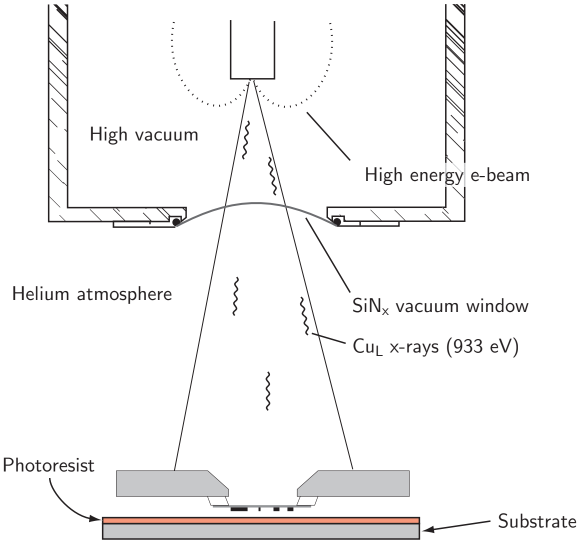

Figure 1-5: Schematic depicting the Cu$_L$(933 eV) based x-ray lithography system commonly used in the NSL. A Roentgen source produces x-rays that travel to a 1× mask. This mask casts a shadow onto the substrate.

spherical waves, which interfere at the substrate at a half-angle θ. The standing wave created at the substrate surface is used to expose a grating or grid in photoresist. In principle IL is quite simple; in practice, maintaining a stable standing wave pattern over the time it takes to expose the photoresist is quite difficult. In the SNL IL system this problem is solved by using an active fringe-locking system that consists of a beam-splitter, differential amplifier, and a Pockels' cell. The beam-splitter recombines a small portion of each arm to form a fringe pattern on the the two detectors. A Pockels' cell locks this fringe pattern by varying the phase in one of the arms. In the NSL we use a simpler system that will be described in chapter 2.

IL is capable of producing high-quality gratings with long-range spatial coherence. While it is possible to create gratings with variations, *e.g.* chirped gratings, it is impossible to directly produce abrupt phase-shifts in the gratings.

X-ray Lithography

Proximity x-ray lithography (PXL) is conceptually very similar to OPL, *i.e.* casting a shadow through a 1× mask, except for the fact that it uses much shorter wavelength photons that range in wavelength from 0.4 nm to 1.4 nm. PXL is capable of fabricating devices with deep sub-100 nm feature sizes [10]; there are current efforts to push PXL to reliably print features down to 25 nm [11]. In the NSL we use an electron bombardment source to generate x-ray photons (wavelength of $\lambda = 1.3$ nm). These photons pass through a non-absorbing atmosphere, typically vacuum or He, and onto an x-ray mask. The x-ray mask contains the absorber patterns which cast a shadow onto the substrate. The mask is held less than 5 μm from the substrate. PXL can easily reproduce patterns that are greater than 50 nm under these conditions. The particulars of PXL will be explained in more detail in chapter 2.

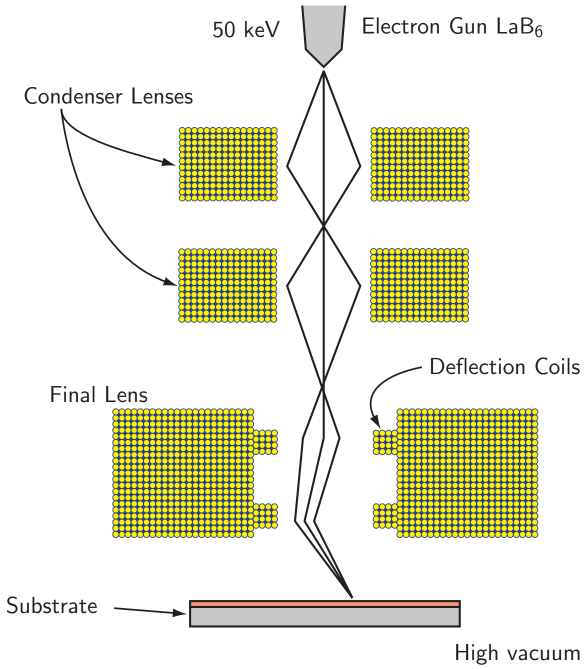

Figure 1-6: Schematic depicting the VS-2A, which is an e-beam lithography system used within the NSL

E-beam Lithography

Electron-beam lithography EBL is capable of producing fine features of arbitrary geometry. Because of the field-by-field writing nature of EBL, however field-stitching poses a significant impediment to writing large area patterns. The NSL has developed a technique, called spatially phased-locked e-beam lithography (SPLEBL)[12], that solves this field-stitching problem. The SPLEBL technique in combination with IL is capable of producing high-quality gratings with long-range spatial-phase coherence and abrupt phase shifts.

Planar Fabrication and Microphotonics

The work in this dissertation deals with the adaptation, improvement, and invention of tools and fabrication techniques geared specifically towards Bragg-grating-based microphotonics. The work is divided along two broad lines:

1. improvement of the x-ray lithography mask,
2. development of process and fabrication techniques for Bragg-grating-based devices.

Chapter 2 describes x-ray lithography and the efforts to improve the x-ray lithography mask. It begins by describing x-ray lithography and reviewing the NSL's initial approaches to solving the x-ray mask distortion problem, *i.e.* depositing a low-stress absorber. It next describes a new x-ray mask configuration, as well instructions for fabrication, that addresses many of the issues that have plagued the current x-ray mask designs. The chapter then describes a new measurement tool, called the holographic phase-shifting interferometer (HPSI), that can nondestructively measure in-plane distortion on a global scale. The chapter ends by describing how the HPSI can be incorporated into an adaptive approach for correcting x-ray mask distortion.

Chapter 3 describes the development of fabrication processes that are specifically designed to address the needs of microphotonics. It first describes the unique fabrication requirements of Bragg-grating-based devices. It then describes the reactive-ion etching InP-based materials. Next the chapter describes the epitaxial overgrowth required to clad the devices. Finally the chapter describes a new process, called the dual-layer hardmask process (DLHP), that addresses the unique fabrication issues of microphotonics.

The dissertation concludes by first describing the effects of x-ray mask distortion on the spectrum of Bragg-grating-based microphotonics and then describing how this thesis' work can be carried forward. Additionally, appendix A reviews a variational technique for calculating membrane distortion from absorber stress and appendix B reviews anodic bonding. Taken as a whole this dissertation should enable the reader to fabricate Bragg-grating-based microphotonics.

Chapter 2

X-ray Lithography

Proximity x-ray lithography (PXL) is an attractive approach to large-area lithography for sub-100 nm feature sizes. There are several technical issues that have prevented PXL from being used in a manufacturing setting. These include:

- lack of a bright x-ray photon source that is low-cost, compact, and reliable;
- difficulty of maintaining and controlling the small gaps (10 μm–30 μm with less than 1 μm gap variation) required for extremely fine-feature definition;
- difficulty of writing a 1× mask;
- distortion in the x-ray mask.

After 20 years of continuous development, the latest results from Japan indicate that many of x-ray lithography's primary concerns have been addressed through persistent engineering [13]. Sumitomo has developed a compact synchrotron light source that does not require superconducting magnets. Canon has developed a stepper that can readily handle mask-to-substrate gaps of $<$10 μm and consistently align to better than 20 nm. Nippon Telephone and Telegraph (NTT) has developed a fast and accurate e-beam writing system that has the capability of writing a 1× x-ray lithography mask in about an hour. However, x-ray mask distortion has traditionally been the most problematic and unresolved technical issue.

Because even relatively transparent material still absorb soft x-ray photons significantly, the x-ray mask consists of a thin membrane supported by a larger ring; figure 2-5 illustrates the basic configuration of the x-ray mask used at MIT. X-ray mask distortion is rooted in the flexibility of this thin membrane. The membrane responds to stress in the absorber pattern by displacing both in-plane and out-of-plane. Pattern distortion caused by this motion, especially in-plane, should not exceed a few nanometers if x-ray lithography is to meet the overlay requirements of future devices. To date, four approaches to avoiding x-ray mask distortion have been proposed:

1. control the absorber deposition and annealing processes so that absorber stress is sufficiently low as to cause negligible distortion;
2. predict the distortion and compensate for it in the written pattern [14];

3. use a shorter wavelength x-ray (∼0.5 nm) and a thick (∼5 μm) membrane of diamond [15];
4. compensate for the distortion with an appropriate input stress distribution [16], which may be realized via differential heating.

This chapter will begin by discussing x-rays in general. The chapter will then move on to describe the author's efforts in improving the x-ray lithography mask, especially discussing:

- low-stress sputtering of the x-ray absorber;
- an improved x-ray mask configuration;
- a system to non-destructively measure in-plane x-ray mask distortions.
- initial efforts at stress compensation.

2.1 X-rays

Producing a soft x-ray photon, *i.e.* a photon with a wavelength of about 10 Å, is difficult. The most straight forward technique is to bombard a solid target with electrons. More exotic techniques that produce higher flux are also being pursued. Fortunately, calculating the material absorption for the x-ray photons that are produced is a relatively straightforward task.

2.1.1 X-ray Absorption in Materials

Absorption of x-ray photons is simply described by:

$$I(z) = I_0 \exp\left[-\mu(\lambda)\rho z\right] \quad , \tag{2.1}$$

where ρ is the density of the material, in units of grams/cm^3, and $\mu(\lambda)$ is the mass absorption coefficient, in units of cm^2/grams. The mass absorption coefficient is tabulated for elements 1–92 by Henke *et al.*[17]. For pure materials, the mass absorption coefficient can be described by:

$$\mu = \frac{N_A}{A}\sigma_a \quad , \tag{2.2}$$

where σ_a is the atomic absorption cross section in units (cm^2/atom); N_A is Avogadro's number and A is the atomic weight. Oftentimes we are interested in the amount of x-ray energy absorbed in compound materials, *e.g.* photoresists. We can approximate the mass absorption coefficient of a compound material, containing n different types of atoms, with x_i of type i, through the relation:

$$\mu = \frac{N_A}{\sum_{i=1}^{n} x_i A_i} \sum_{j=1}^{n} x_j \sigma_{a,j} \quad . \tag{2.3}$$

We can use this formula to calculate the absorption curves of various materials of interest, *e.g.* photoresist. Except for certain second-order effects, these simple relations fully describe x-ray photon absorption in matter.

2.1.2 NSL Cu$_L$ Source

In the NSL we use an electron bombardment source, commonly referred to as a Roentgen source[1]. As illustrated in figure 2-1a, we heat a tungsten filament, using a high current, until electrons are thermionically emitted. These electrons are focused by an electrostatic focusing element that is biased to -8 kV, onto a water-cooled copper[2] target that is connected to electrical ground. Figure 2-1b depicts an impinging electron generating an x-ray photon within the x-ray generation region. When an electron strikes a copper atom, it can ionize an electron out of any of the inner shells. Often, this results in the emission of an Auger electron, which simply heats target. However, if an L-shell electron is ionized, and an M-shell electron relaxes to fill the vacancy an x-ray photon, at the characteristic wavelength of 1.3 nm, is generated. The probability of generating an Auger electron is much higher than that of producing a useable photon. This is not really a problem except that this source requires long exposure times.

Ideally a Roentgen source will give off a very sharp line at the characteristic wavelength. Unfortunately some of the electrons, rather than scattering an inner-shell electron, undergo an inelastic Rutherford scattering process. This effect gives rise to ‘braking’ radiation, or *Bremsstrahlung radiation*, that results in photons being generated over a wide range of wavelengths. Bremsstrahlung radiation’s characteristic spectral density can be described by:

$$I(\lambda)d\lambda = Zh^2kc^2\left(\frac{1}{\lambda}-\frac{1}{\lambda_0}\right)\frac{1}{\lambda^2}d\lambda \quad , \tag{2.4}$$

where Z is the atomic number of the target, h is Planck’s constant, c is the speed of light, k is a weakly material-dependent empirical constant, and λ_0 is the minimum photon wavelength corresponding to the highest energy electron. Since we accelerate the electrons to 8 keV, the minimum wavelength is 1.55 Å. As shown in figure 2-1b the x-ray generation volume takes exists within the copper target. Therefore as the x-ray photons emerge from the generation volume, the copper target alters the natural spectrum through its characteristic absorption. Pella *et al.* developed a correction for this effect that accounts for the reabsorption of radiation by the target by incorporating an empirically determined correction factor [18]. Incorporating this

---

[1] Roentgen discovered x-rays on a system that does not differ significantly from the NSL lithography source. While some would consider the source primitive, we consider the source time-tested and reliable.

[2] More precisely, the target is 98% copper and 2% aluminum. This alloy withstands heat better than pure copper.

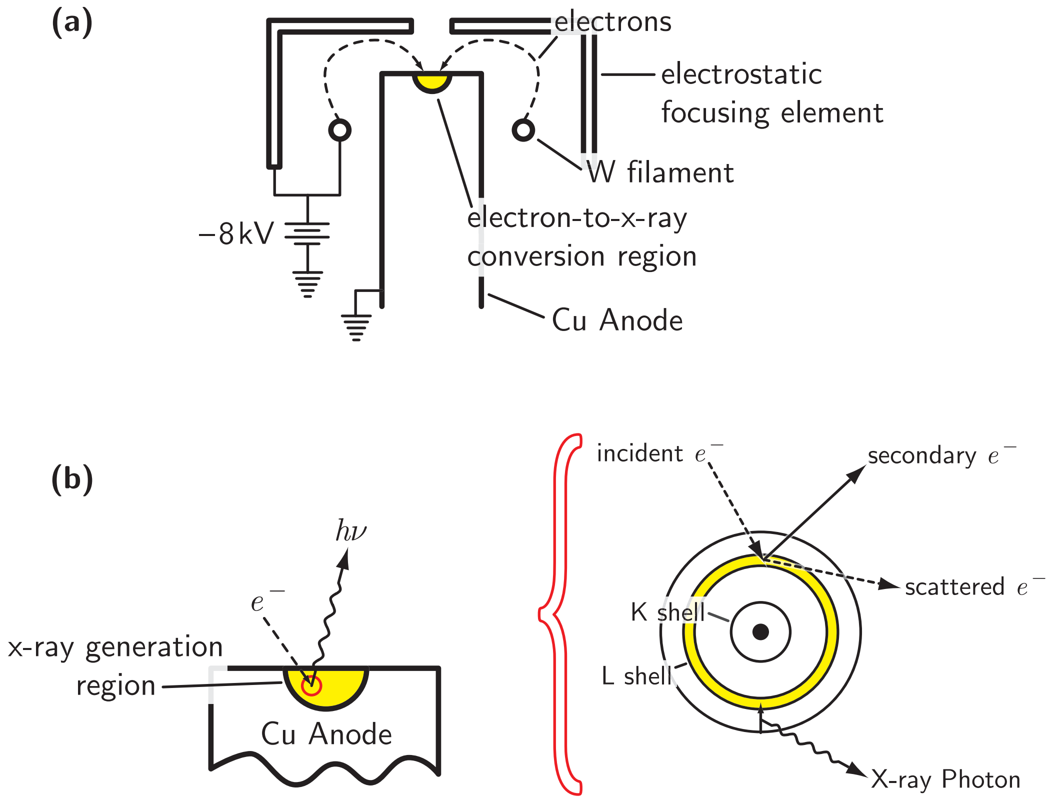

Figure 2-1: (a) basic configuration of the NSL electron-bombardment source. A tungsten filament that is biased to -8 kV is ohmically heated so that it emits thermionic electrons. The electrons are focused by an electrostatic focusing element, that is also biased to -8 kV, onto a water-cooled copper target that is connected to electrical ground. (b) illustrates an impinging electron generating an x-ray photon within the x-ray generation region. When an electron strikes a copper atom, it can ionize an electron from the inner-shells. An x-ray photon is generated when an L-shell electron is ionized and subsequently filled.

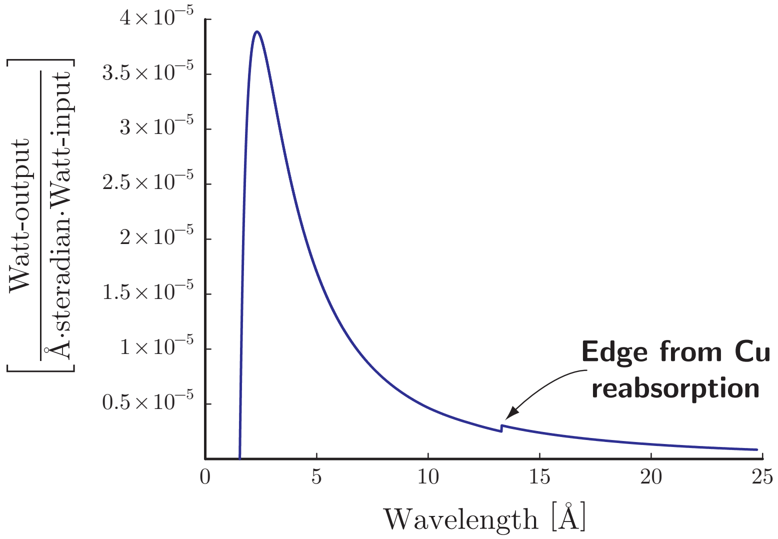

Figure 2-2: The Bremsstrahlung spectrum calculated using equation (2.5).

correction, the Bremsstrahlung can be described by:

$$\frac{\partial}{\partial\lambda\partial\Omega}P(\lambda,\Psi) = (2.72\times10^{-5}Z)f(\lambda,\Psi)\left(\frac{\lambda}{\lambda_0}-1\right)\left(\frac{1}{\lambda}\right) \quad , \tag{2.5}$$

$$\text{with units} \quad \left[\frac{\text{Watt output}}{\text{Å·steradian·Watt input}}\right] \quad ,$$

where $f(\lambda,\Psi)$ is the *target reabsorption factor*, an empirical term that accounts for the photon absorption as it emerges from the target. It can be described by

$$f(\lambda,\Psi) = (1+C\xi)^{-2} \quad , \tag{2.6}$$

where C is a fitting parameter described by

$$C = \frac{1+(1+2.56\times10^{-3}\,Z^2)^{-1}}{\left(1+2.56\times10^{-3}\,\lambda_0 Z^{-2}\right)\left(\frac{\xi}{4}+10^4\right)} \quad . \tag{2.7}$$

In equation (eq:TR.fitting), ξ is a spectral dependent parameter expressed as:

$$\xi = \left(\frac{1}{\lambda_0^{1.65}}-\frac{1}{\lambda^{1.65}}\right)\rho_t\mu_t(\lambda)\csc(\Psi) \quad , \tag{2.8}$$

where ρ_t is the density of copper, and $\mu_t(\lambda)$ is the mass absorption coefficient of copper.

2.1.3 The SRL Plasma-Pinch Source

Z-pinch plasmas were originally developed by bomb scientists in an attempt to induce nuclear fusion. While this attempt proved to be a costly failure, it was found that

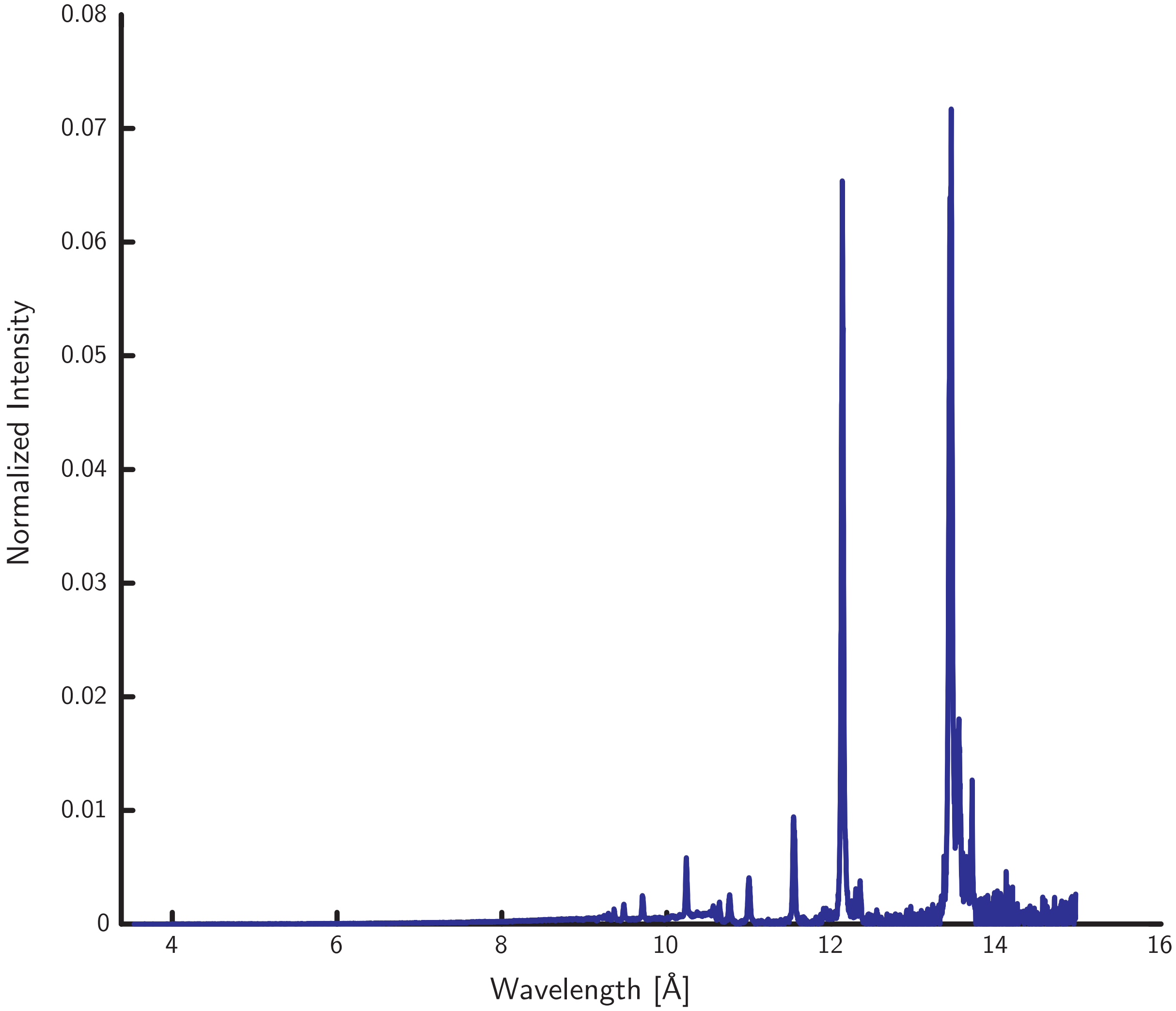

Figure 2-3: The spectrum of the SRL plasma pinch source is very good for x-ray lithography.

z-pinch plasmas were efficient producers of x-rays. Scientific Research Laboratories (SRL) (Somerville, MA) has developed a soft x-ray source based on the principle of the z-pinch plasma. Specifically, the source produces a z-pinched plasma of neon gas producing characteristic x-ray lines around 12.1 and 13.5 Å. Figure 2-3 illustrates the spectrum of the SRL source.

Figure 2-4 shows an x-ray print using the SRL plasma pinch source. The x-ray mask was held at a distance of 50 cm from the source and exposed for approximately 20 minutes. The mask-substrate gap was 3 μm. The x-ray mask printed faithfully and quickly into the PMMA. Under similar exposure, conditions the NSL source would have taken approximately 96 hours. The SRL x-ray source promises to be bright and reliable enough for use in monolithic-microwave integrated circuits. Moreover, there are currently other plasma-based soft x-ray sources in development that should give similar results.

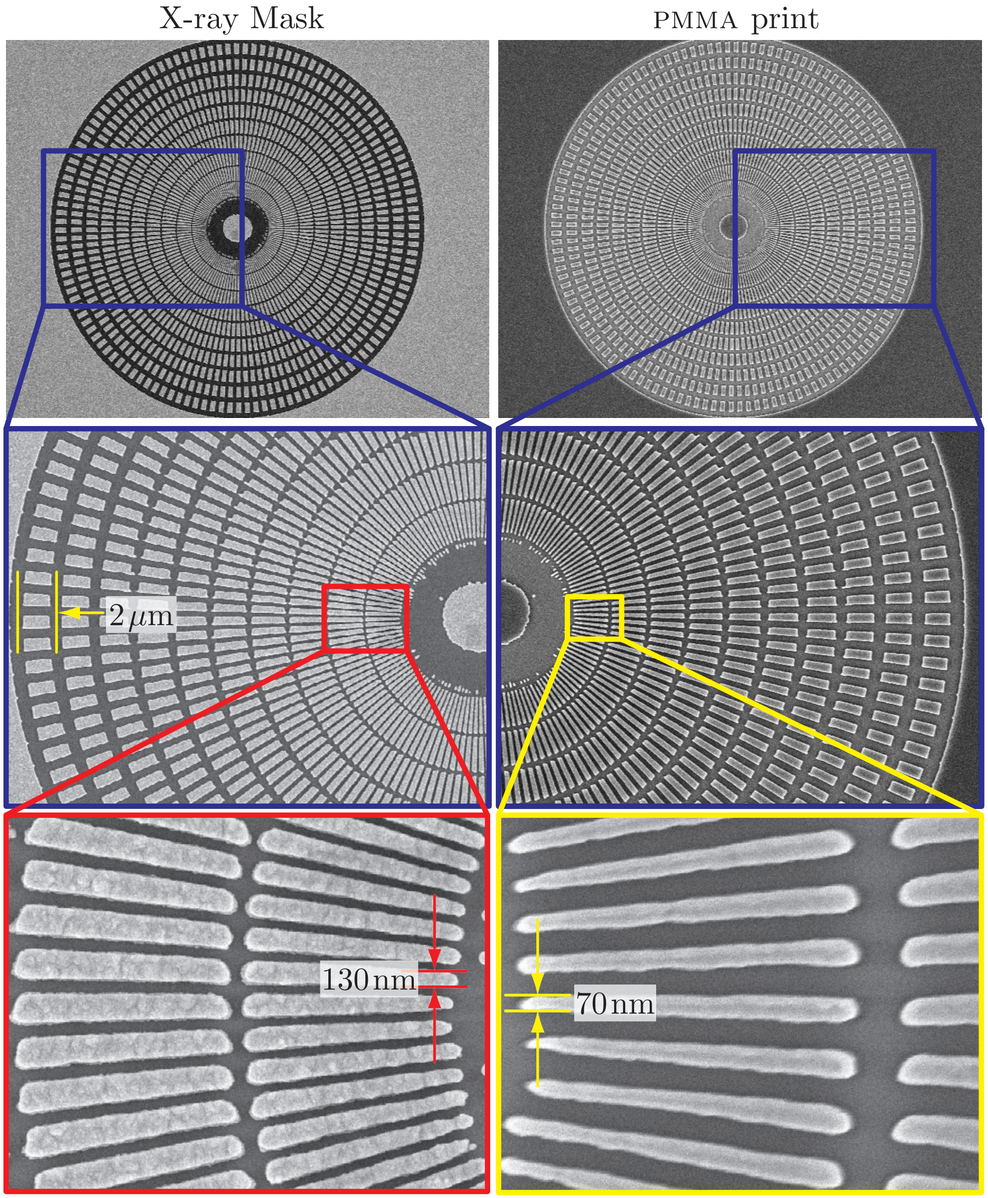

Figure 2-4: X-ray mask and sample exposed on the SRL Z-pinch plasma source. The exposure took place at a gap of 3 μm. The thickness of the PMMA was 300 nm. The sample developed at a rate of 11.5 nm/sec.

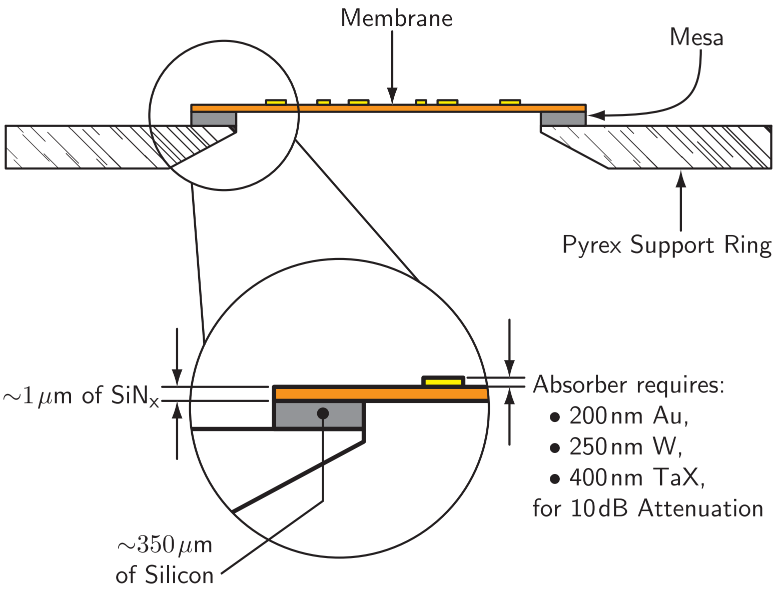

Figure 2-5: The standard NSL x-ray mask configuration was dictated by the needs of PXL within the NSL. The mask consists of a 1 μm thick SiN_x membrane mounted onto a pyrex ring via a silicon mesa-ring. Other material options for the membrane include SiC and diamond; both these materials are superior to SiN_x in every respect (*i.e.* more transparent, stiffer) except for their high cost. Other material options for the absorber include W and Ta-based alloys; these absorbers must be thicker than Au to achieve the same attenuation.

2.2 The X-ray Mask

Since x-ray photons are a precious resource the material that holds the absorber must be as thin as possible in order to minimize photon absorption. The NSL x-ray mask, shown in figure 2-5, consists of a 1 μm-thick SiN_x membrane supported by a pyrex ring. The absorber is electroplated gold[3].

2.2.1 Depositing a Low-Stress Absorber

One of the earliest approaches to decreasing x-ray mask distortion was depositing a low-stress absorber. The internal stress of the absorber must be sufficiently low that it does not contain enough energy to significantly distort the x-ray mask membrane; typically this means that the stress must be $\leq$10 MPa. There are two major strategies for achieving a low-stress absorber film:

1. Deposit compressively stressed absorber onto the x-ray mask and then heat the sample. The heating will anneal the stress out of the absorber [20].

2. Control the sputter deposition conditions well enough that the absorber is deposited with very little stress.

---

[3] Fabrication details for the NSL x-ray mask can be found in reference [19]

Past efforts have focused on depositing the absorber onto the membrane prior to its formation. The NSL effort has focused on depositing the absorber directly onto the membrane, and thereby avoiding many of the complications that occur during the membrane formation step. In the NSL, one attempts to deposit a low-stress absorber film by monitoring the stress during the deposition. This was first performed by monitoring the acoustic resonance frequency of the x-ray mask [21]. Later, a sputtering technique was developed that controls the membrane temperature by flowing helium along its backside, while monitoring the membrane bulge [22]. The helium makes good thermal contact to a temperature controlled heatsink and maintains an even temperature across the membrane during the sputtering run. The membrane bulges in response to both the He-backside pressure and the stress of the deposited absorber [23]. The bulge monitor (precision $\sim$0.5 μm) operates by measuring the amount of specularly reflected light at several points around the surface of the membrane.

The author used the bulge monitoring technique, in conjunction with the temperature control, to reliably deposit low-stress tungsten absorber onto x-ray masks. Figure 2-6 shows the output of a typical sputtering run. When deposition of the absorber begins there is an immediate large measurement offset in the bulge. This occurs because initially the absorber does not evenly cover the membrane; this ‘spotty’ absorber coverage results in higher specular reflection, which makes the membrane seem further away. By the end of the run, the system records a bulge offset of -5.1 μm. This offset value was found to result in a low-stress absorber film.

Measuring Stress

Stress can be measured using a number of techniques. The most commonly used technique to determine film stress, σ_f, is measuring the bow of a silicon wafer and then applying Stoney’s equation:

$$\sigma_f = \frac{E}{1-\nu}\frac{t_s^2}{6Rt_f} \quad ,$$

where E and ν are the Young’s modulus and Poisson’s ratio of silicon, t_s is the thickness of the silicon wafer, and t_f is the thickness of the film, and R is the radius of curvature. Unfortunately this simple technique assumes that the film has the same stress everywhere, which is often not the case. To measure stress on a membrane one can either measure the in-plane or out-of-plane distortion (IPD and OPD respectively). The common technique for measuring IPD employs a metrological measurement tool, such as the LMS-2000, which compares the location of crosses before and after absorber deposition. We will describe an alternative IPD measurement technique in section 2.3.

Measuring OPD is also a very accurate way to measure stress. If one deposits absorber material and then etches away a half-plane of it, the internal stresses of the absorber will cause the membrane to buckle at the absorber/membrane interface. Figure 2-7 depicts how an absorber under tensile stress will cause the membrane to buckle at their interface. The Linnik interferometer is the most appropriate tool for measuring OPD. It is a Michelson interferometer, with the addition of two matched

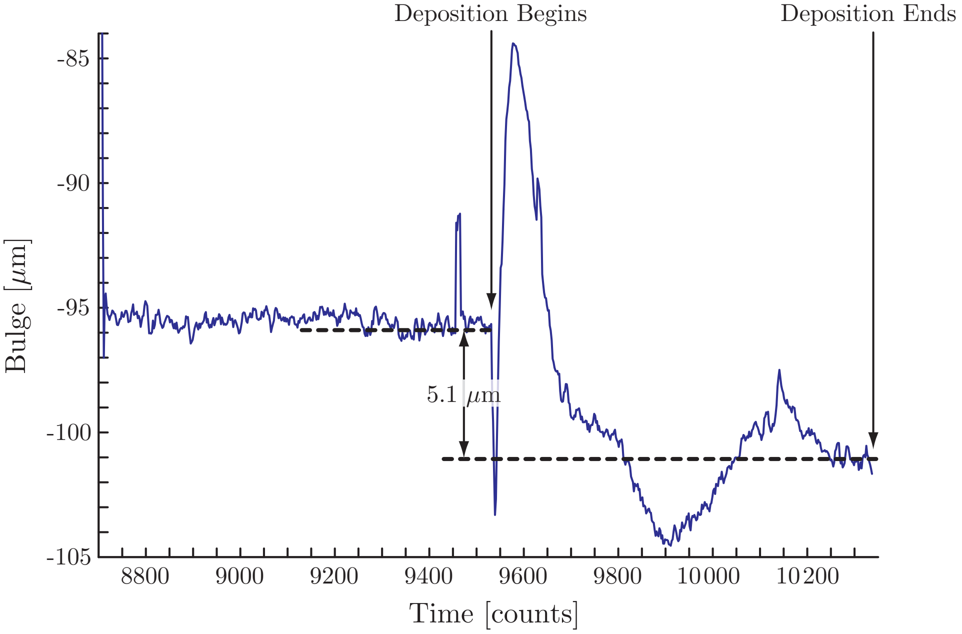

Figure 2-6: The bulge of the membrane is indicative of the stress of the deposited film. When deposition of the absorber begins there is an immediate large measurement offset in the bulge. This occurs because initially the absorber does not evenly cover the membrane; this 'spotty' absorber coverage results in higher specular reflection, which makes the membrane seem further away. By the end of the run, the system records a bulge offset of -5.1 μm. This value was found to result in low-stress absorber.

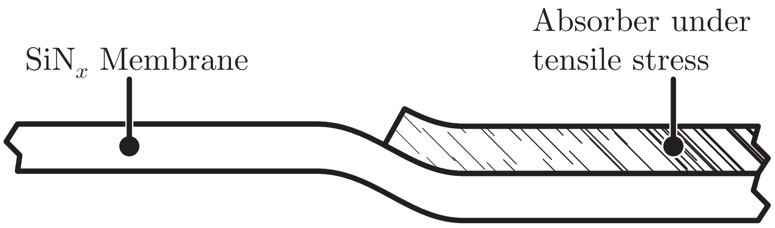

Figure 2-7: Depiction showing an absorber, under tensile stress, causing a membrane to buckle and exhibit OPD.

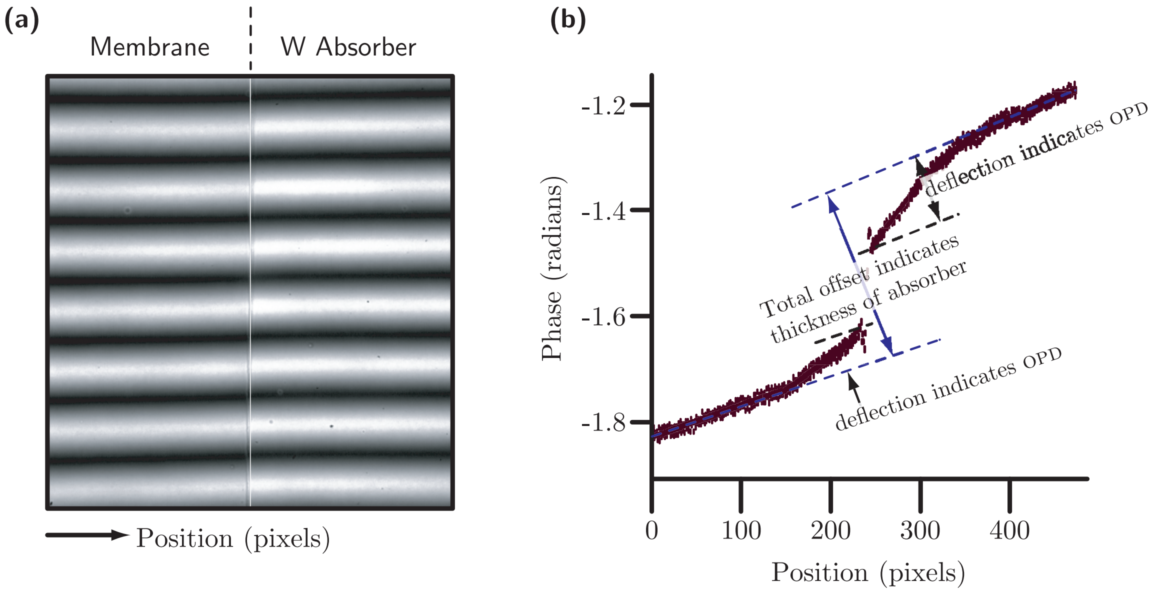

Figure 2-8: Out-of-plane distortion can be accurately measured using a Linnik Interferometer. (a) shows an interferogram of the interface between the tungsten absorber and the SiN_x membrane; the interferogram shows a square that is about 4 μm per side. (b) shows the phase displacement of each fringe. Because we use a narrow band optical filter, centered around 546 nm, we can easily translate the phase data to out-of-plane distortion data: each radian is equivalent to an OPD of $\lambda/2$.

high-power objectives in each arm, that can measure the surface heights very precisely over small areas. Figure 2-8a shows a Linnik interferogram from the sample sputtered during the run shown in figure 2-6; the interferogram shows a square that is about 4 μm per side. Figure 2-8b shows the phase displacement of each fringe which we extract by taking 1D Fourier transforms of each column. Because we use a narrow-band optical filter, centered around 546 nm, we can easily translate the phase data to height data: each radian is equivalent to $\lambda/2$.

From the OPD one can easily calculate the stress of the absorber, σ_a, using the relation [24]:

$$\sigma_a = \frac{2\sigma_m \eta}{t_a\left(1+\frac{t_a}{t_m}\right)} \quad , \tag{2.9}$$

where σ_a is the stress of the membrane (~100 MPa), η is the total OPD, t_a is the thickness of the absorber (250 nm), and t_m is the thickness of the membrane (1 μm). Figure 2-9 shows OPD measurements across the x-ray mask; the absorber deposition run was shown in figure 2-6. A 10 nm chrome adhesion layer is deposited, through e-beam evaporation, prior to the deposition of the tungsten. As the plot shows, the OPD immediately after the sputtering run is very low, indicating an intrinsic stress level below 10 MPa across the membrane surface. The plot also indicates that the chrome adhesion layer does add some tensile stress, but this can largely be ignored since the chrome will never be removed. After heating the x-ray mask for 1.5 hours at

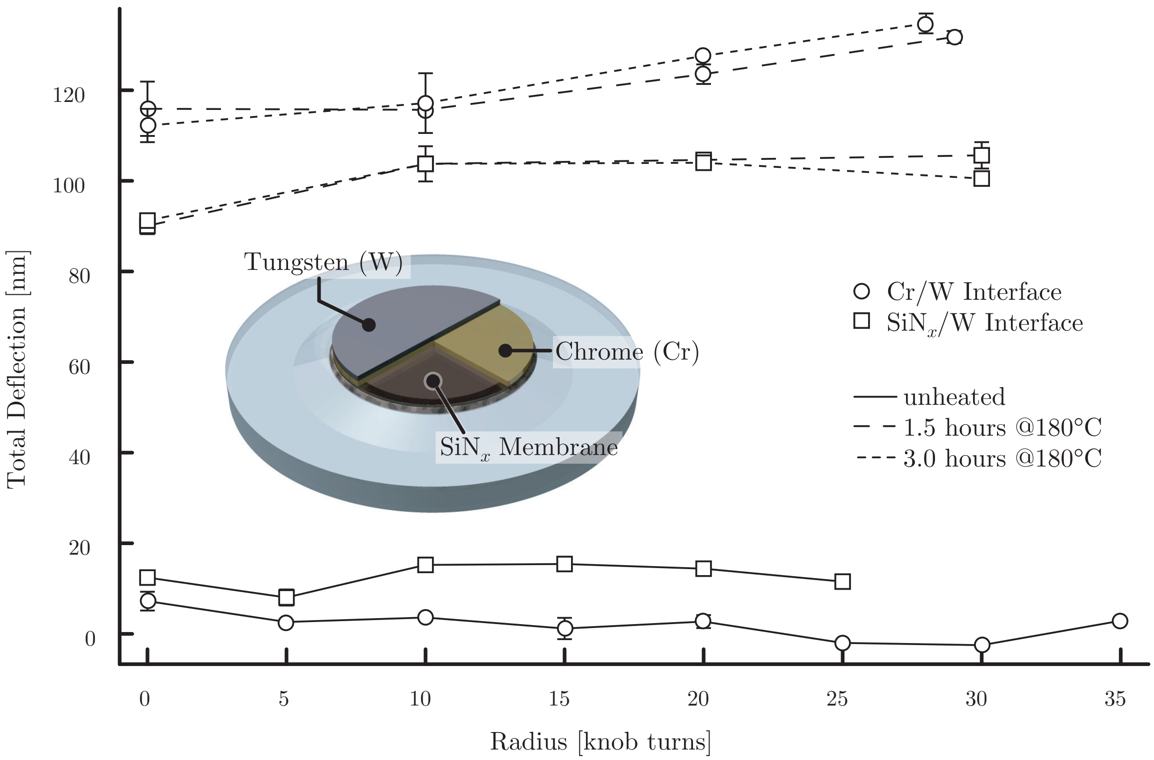

Figure 2-9: Measuring the OPD of an x-ray mask using the Linnik interferometer. The tungsten was deposited using the controlled-bulge technique. Five knob-turns is equivalent to 2 mm. Zero turns is very close to the periphery of the membrane, and 30 turns is the approximate center of the membrane. The W/Cr interface is the measurement of most interest. The stress is low and equal across the surface of the membrane. After heating the intrinsic stress becomes significantly more tensile and uneven.

180°C, the stress of the absorber film becomes significantly more tensile; an additional 1.5 hours of heating does not significantly affect the stress of the film. Then, an alternative deposition technique is to deposit compressively stressed absorber, then anneal to achieve zero-stress films. This confirms that annealing out the stress using heat is a viable alternative to depositing low-stress absorber. One caveat is that the stress is significantly less uniform over the surface of the membrane. This can be attributed to the vastly different thermal masses: the ring takes much longer to heat, while the central membrane region heats quickly with little contact to any heat sinks. This could be remedied by using a film with a much higher thermal conductivity, *e.g.* diamond.

This work was repeated on several masks with similar results. It demonstrates that low-stress absorber can be readily deposited directly onto x-ray mask membranes. It was found that in its current state, post-deposition annealing of the absorber would not evenly affect the entire membrane due to thermal effects. This could be solved by using a diamond membrane, but until then the bulge-monitored deposition, with temperature stabilization, is the best strategy to depositing low-stress absorber. This

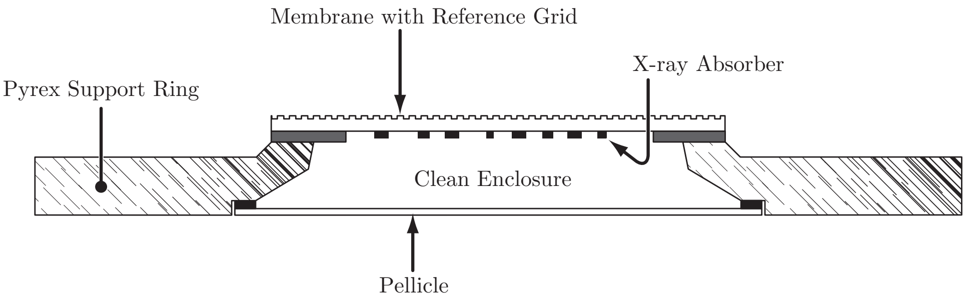

Figure 2-10: The ultimate x-ray mask configuration incorporates several important features to make x-ray lithography more robust. The mesa structure is optically flat, which ensures that the membrane area will be extremely flat. The absorber is protected by a pellicle in order to prevent particulate contamination. A fiducial reference grid is incorporated into the membrane to monitor long term distortion in the membrane. To build this mask configuration, the membrane must be directly bonded to the pyrex ring.

technique goes a long way to solving the distortion problem for the x-ray mask, but there are additional problems with the x-ray mask that must be addressed.

2.2.2 Improved X-ray Mask

Hector *et al.* found that using x-ray lithography for $\leq$100 nm patterns requires the ability to control the mask-substrate gap to $\leq$0.5 μm [25]. Unfortunately, the NSL's current x-ray mask configuration is flat to only 1 μm due to deformations that occur when anodically bonding the silicon quarter-wafer to the pyrex ring. We clearly need to improve the x-ray mask configuration in order to:

1. create an extremely flat surface for the required gap control;
2. protect the x-ray absorber pattern from particulate contamination;
3. incorporate a fiducial system for *in-situ* monitoring of x-ray mask distortions.

Figure 2-10 depicts the ultimate configuration for an x-ray mask. It incorporates several important features to make x-ray lithography more robust. The mesa structure is optically flat, which ensures that the membrane area will be extremely flat. The absorber is protected by a pellicle in order to prevent particulate contamination. A fiducial reference grid is incorporated into the membrane to monitor long term distortion in the membrane. The most obvious feature is that the membrane must be directly bonded to the pyrex ring with the absorber pattern facing inward. There are two ways this can be accomplished:

1. by bonding the membrane to the pyrex ring and then attempt to pattern the features;
2. by patterning the features directly onto the membrane and then bonding it to the pyrex ring.

The latter option is more attractive since patterning on a planar surface is much simpler than patterning within a well-like structure. This requires being able to flip-bond a membrane directly onto a pyrex ring without distortion, which in turn requires being able to non-destructively monitor IPD on a global scale. For this we devised the Holographic Phase-Shifting Interferometer (HPSI).

2.3 Holographic Phase-Shifting Interferometer

The HSPI system, illustrated schematically in figure 2-11, is very similar to the interferometric lithography (IL) system described in figure 1-4. The IL system is configured as a holographic interferometer simply by mounting the IL-generated grating on the substrate platform and placing a fluorescent screen in front of one of the spatial filters, as depicted in figure 2-11. A fringe pattern appears on the screen, which is due to the superposition of two wave fronts: one reflected from the substrate surface and the other back-diffracted from the grating. As figure 2-12a shows, if the grating has suffered no distortion between exposure and reinsertion, the reflected and back-diffracted beams will be identical and no fringes will be observed on the screen. Figure 2-12b shows how any in-plane distortion of the grating will result in a fringe pattern. A CCD camera is used to record the fringe patterns.

In order to increase the sensitivity of the interferometer, a phase-shifting [26] system was implemented. A piezoelectric transducer pushes the beam-splitter, and in so doing drives the Pockels' cell to change the phase of one of the arms [27]. Several images are acquired, recorded, and processed using a symmetric phase-shifting algorithm (SPSA) [28, 29]. Specifically, the SPSA takes $N+1$ images, where N is an even number, that have been equally phase shifted through 2π, to solve for the phase offsets, Φ, using the relation:

$$\tan(\Phi) = \frac{(I_{N+1} - I_1)c_0 + \sum_{n=1}^{N-1} I_{n+1} \sin\left(\frac{2\pi n}{N}\right)}{-\frac{I_1 + I_{N+1}}{2} - \sum_{n=1}^{N-1} I_{n+1} \cos\left(\frac{2\pi n}{N}\right)} \quad , \tag{2.10}$$

where

$$c_0 = \frac{1}{N} \sum_{n=1}^{(N/2)-1} (N - 2n) \sin\left(\frac{4\pi n}{N}\right)$$

is a correction factor that takes any phase error into account, and I_i is the i^{th} image of the series. The acquisition and processing time takes less than one minute. To convert the phase map into a distortion map, we remove the 2π phase jumps through the use of Goldstein's branch cut algorithm [30], which was originally developed for synthetic-aperture radar. The HPSI measurement technique is a rapid, accurate and global. Figure 2-13 is an example of taking 21 images and constructing a phase map using the SPSA algorithm in conjunction with the Goldstein phase unwrapping algorithm.

Other grid-based techniques to measure in-plane distortion have been described by Ruby *et al.* [31] and Ku *et al.* [24]. In both of these techniques the system that generated the grid and the system that measured the grid were not matched; this can

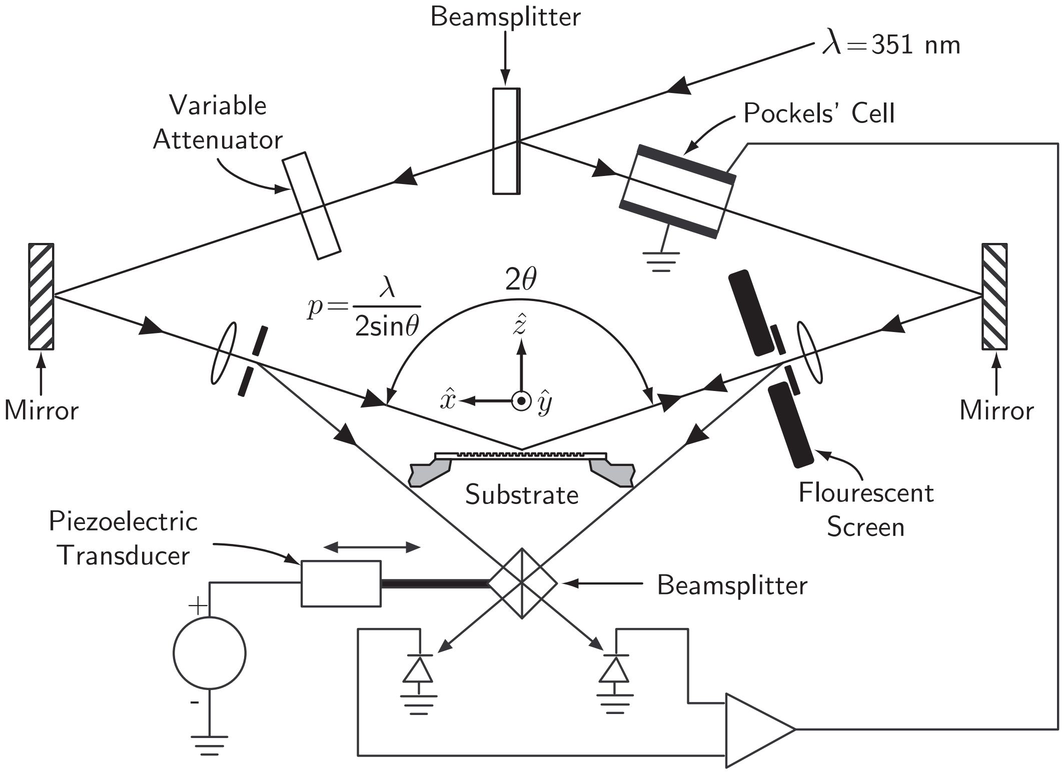

Figure 2-11: Schematic of the interferometric lithography (IL) system, modified to function as a holographic phase-shifting interferometer (HPSI). Three modifications convert the IL system into the HPSI: (1) A screen placed in front of one pinhole to capture the interference pattern between the specularly reflected and back-diffracted beams; (2) A piezoelectric transducer that pushes the beamsplitter—this in turn causes the Pockels' to put a phase shift in one arm; and (3) A CCD camera to record the fringe patterns (not shown).

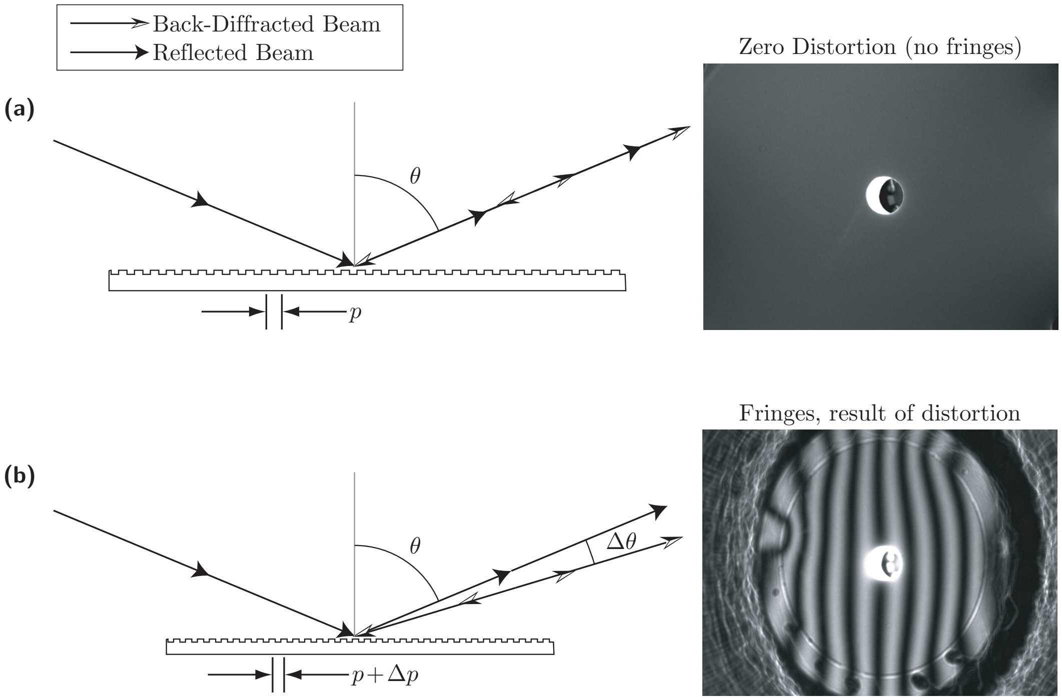

Figure 2-12: The distortion of membrane causes a divergence in the reflected and diffracted beams that gives rise to an interference pattern.

result in ambiguity since one does not know whether the measured in-plane distortion is real or simply an effect of the mismatched systems. In the HPSI system, the gratings or grids are generated in the same system in which they are measured.Using the HPSI to measure IPD has the advantage that only a grating or grid must be placed onto the membrane. Moreover, the HPSI can quickly and accurately measure IPD over a large area. Obviously this technique is well suited to analyzing x-ray mask distortion.

2.3.1 Distortion from Flip-Bonding

Figure 2-14 outlines the beginning steps in the formation of the flip-bonded x-ray mask. The flip-bonded x-ray mask fabrication begins with a silicon wafer (100 mm diameter) uniformly coated with 1 μm of silicon-rich nitride (SiN_x) on both the front and the backside; the SiN_x is deposited by low-pressure chemical-vapor deposition (LPCVD). A 54 mm-diameter circular opening is then reactive-ion etched (RIE) through the nitride on the backside, and the Si is etched in KOH at 90°C. Interferometric lithography was done on the backside of the resulting membrane, using a trilevel process [32], to yield a 400 nm-period grating. This grating is then etched 100 nm deep into the SiN_x membrane. As illustrated in figure 2-14f, the 54 mm-diameter SiN_x membrane, with the shallow grating etched into it, is supported by a Si annulus which remains from the original Si wafer.

In the final step, we flipped the membranes over, and anodically bonded it to pyrex rings using a nickel bonding technique, as illustrated in figure 2-15b. The anodic bonding took place at 350°C–400°C with a bias voltage of 1.1–1.3 kV. We set

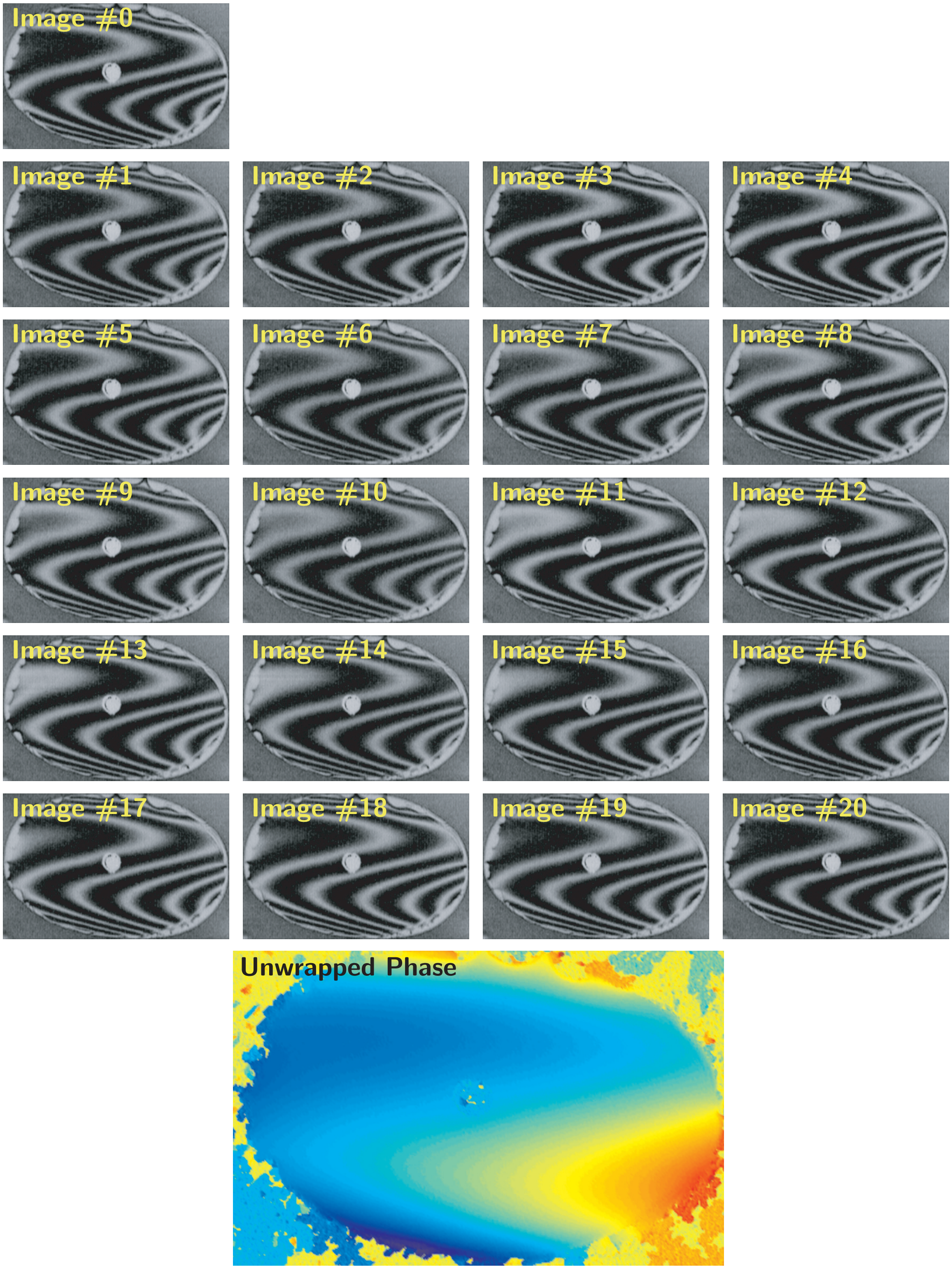

Figure 2-13: The symmetric phase-shifting algorithm uses an even number series of phase-shifted images in order to calculate the phase distortion of the grating surface. Here 21 images have been used to process the phase data, but depending on the signal-to-noise ratio of the images as few as 5 images can be used.

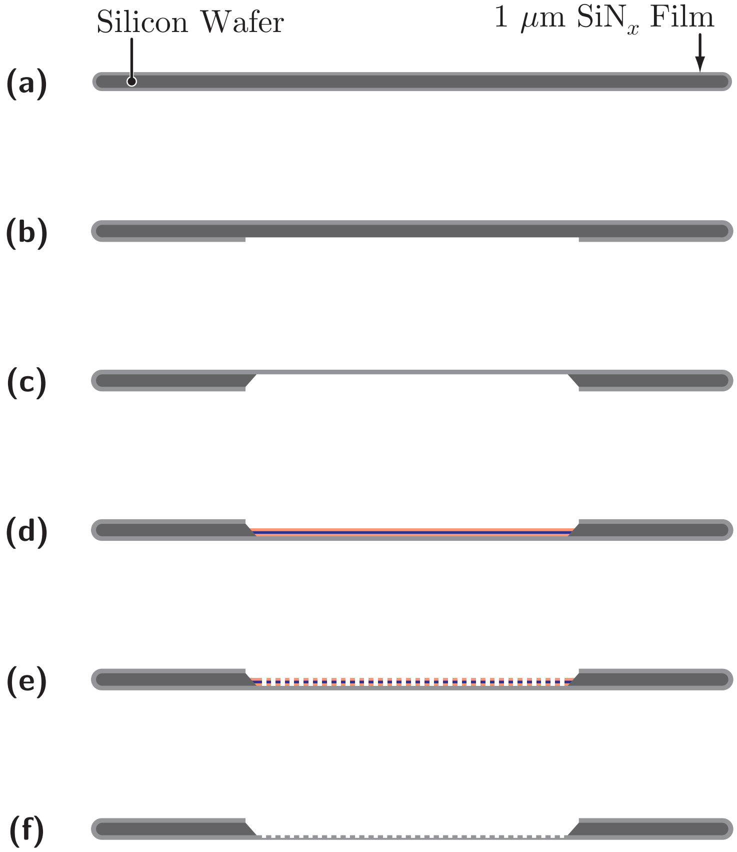

Figure 2-14: The first step in analyzing the distortion due to flip-bonding is creating a membrane with a fiducial grating. (a) the starting material is a silicon wafer with a 1 μm-thick film of SiN$_x$. (b) an opening is created in the film by reactive-ion etching in CHF$_3$ using a stencil mask. (c) the entire wafer is placed in a 90°C KOH bath for several hours which etches through the silicon wafer and results in a membrane. (d) a trilayer (ARC, SiO$_2$, and photoresist) is placed onto the membrane. (e) a grating is patterned using interferometric lithography. (f) the gratings is finally transferred into the SiN$_x$ membrane.

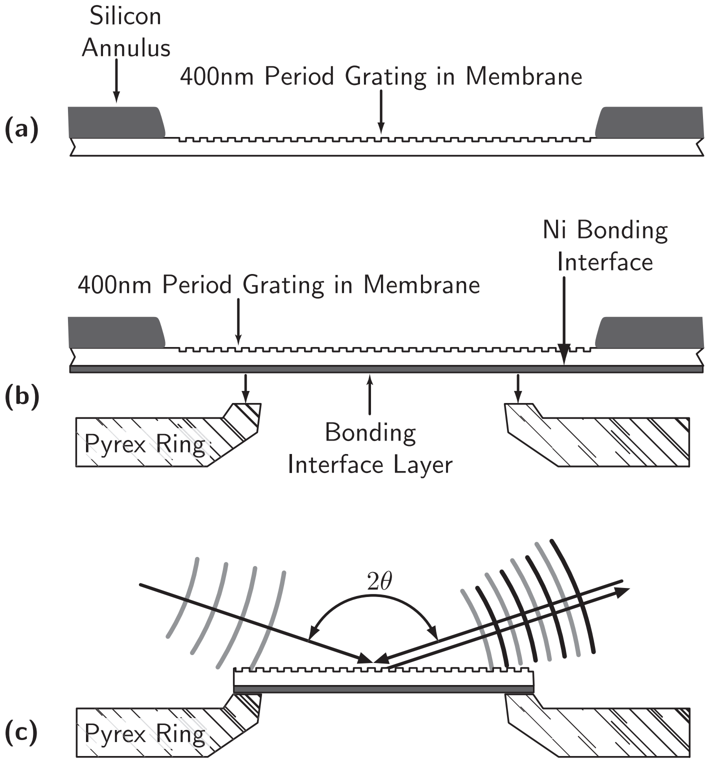

Figure 2-15: Process for completing the flip-bonded x-ray mask

one membrane aside as the reference grating to align the HPSI system, and deposited a 30 nm-thick layer of Ni on the front surfaces of the remaining membranes. To ensure that the distortion measured came from the flip-bonding step, the reference grating was processed identically to the measured samples, with the exception of the final flip-bonding step. We used nickel as the bonding interface layer (BIL), but in principle any metal that oxidizes can be anodically bonded to pyrex (or any other borosilicate glass)[33]. In the past we have used TaB and polysilicon as the BIL; the anodic bonding process is explained in more detail in Appendix B. The silicon annulus and extraneous membranes were removed (figure 2-15c) by breaking the membrane outside of the pyrex ring, while using adhesive tape to retain the shards of SiN_x. As figure 2-16 indicates, the resulting mask has an extremely flat surface.

Because the IL system uses spherical wavefronts the period of the grating exposed depends on the substrate's position along an axis perpendicular to the substrate (*i.e.*, the $\hat{z}$-axis defined in figure 2-11). To ensure that the substrate's position upon reinsertion is exactly the same as when it was exposed, we also expose a reference grating. Prior to measurements on the membranes, the reference grating is reinserted into the HPSI system and its $\hat{z}$-position adjusted until the fringes on the screen are minimized. After the reference grating is positioned and the HPSI system aligned, we use a Michelson interferometer to ensure that the gratings to be measured are in exactly the same plane as the reference grating. The Michelson interferometer uses the surface of the reference grating in one arm and a reference mirror in the other arm. The precision of this adjustment depends on the coherence length of the light

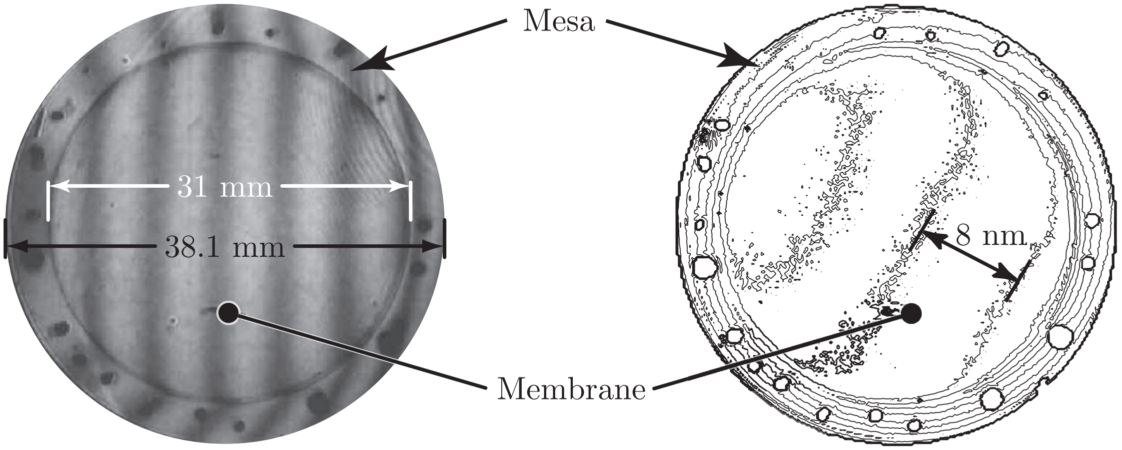

Interferogram of Surface

Contour Plot of Surface

Figure 2-16: The flip-bonded x-ray mask is extremely flat. This mask has a flatness of < 30 nm across the 31 mm diameter membrane. The mesa, *i.e.* thin annulus of pyrex (31 mm inner and 38.1 mm outer diameters) to which the membrane is bonded, is flat to within $\sim$100 nm.

source, *i.e.*, the shorter the coherence length the closer one can match the arms of the Michelson interferometer. Our light source is a semiconductor laser, with a coherence length of 100 μm.

Two samples, MITa598 and MITa599, shown in figure 2-17, were used for the HPSI distortion measurements. A typical measurement, shown in figure 2-18a, illustrates the system's ability to create a map of the in-plane distortion. By separating the distortion data into linear and nonlinear components, shown in figure 2-18b and 2-18c respectively, we can more easily interpret the data. The linear distortion indicates an overall change in period, which represents a magnification distortion. The nonlinear component is indicative of distortion that occurs over a shorter length scale.

The change in period can be extracted from the linear-phase data. The change in linear phase over distance, $\Delta\varphi$, (*i.e.*, the slope of the phase tilt, with units of radians/meter) can be related to the resulting change in period by the simple expression:

$$\Delta p_c = \frac{\Delta\varphi}{2\pi} p^2 \tag{2.11}$$

where p is the period of the original gratings, and Δp_c is the calculated amount that the period has changed. By applying equation 2.11 to the linear data for MITa598, $\Delta\varphi = 1.413 \times 10^3 \frac{\text{rad}}{\text{meter}}$, we can calculate that $\Delta p_c = -0.036$ nm. For MITa599, $\Delta\varphi = 1.210 \times 10^3 \frac{\text{rad}}{\text{meter}}$ which implies that $\Delta p_c = -0.031$ nm. Clearly both samples experienced period compression.

As mentioned above, the period of the standing wave at the substrate surface can be changed by moving the substrate forward or backward, in along the z-axis shown in figure 2-11. The relation between the motion, Δb, and the change in period, Δp_m,

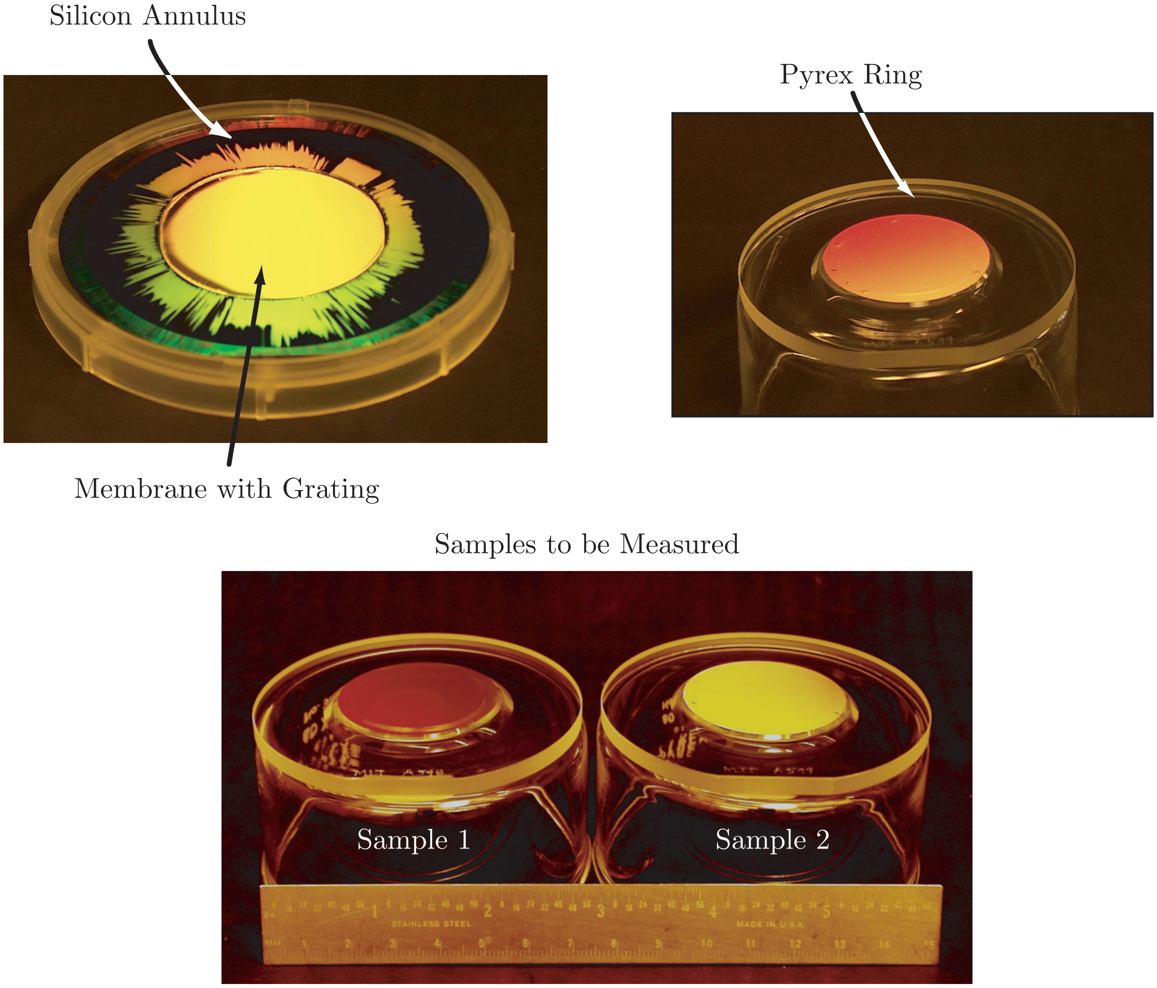

Figure 2-17: Photographs of the flip-bonding process, illustrated in figure 2-15, demonstrates the repeatability of the process.

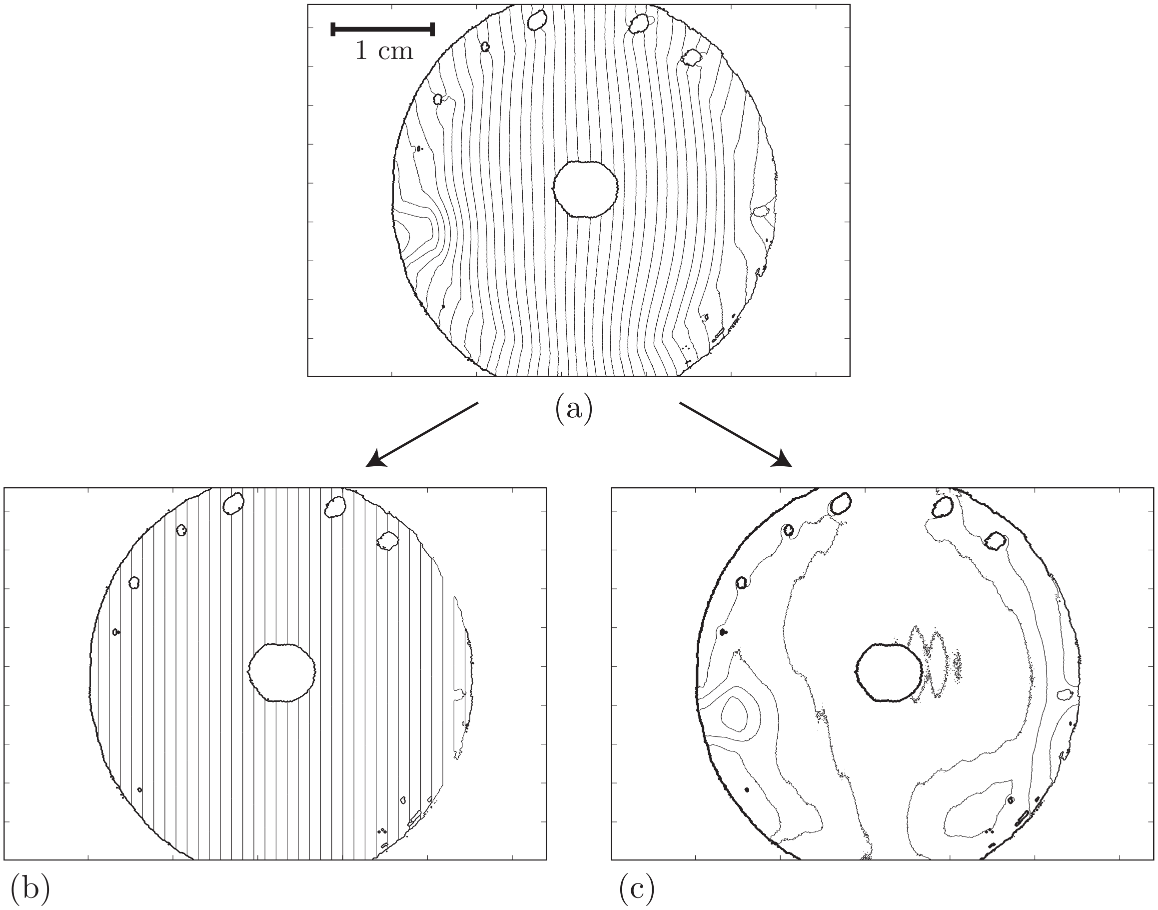

(a)

(b)

(c)

Figure 2-18: Contour plots of the phase distortion data from sample MITa598, measured in the HPSI system. The full data set, (a), can be separated into linear and nonlinear components, shown in (b) and (c) respectively. The linear components represent a magnification, which occurs due to a change in the overall period of the grating. The nonlinear components are due to local distortions. Each contour is separated by $\frac{\pi}{2}$ radians., with every π radian equivalent to an in-plane distortion of 200 nm. The diameter of the measured region is 38.1 mm.

Sample	$\Delta\varphi$ $\left[\frac{\text{rad}}{\text{mm}}\right]$	Δp_c [nm]	Δb [μm]	Δp_m [nm]
MITa598	1.413	-0.036	131	-0.0387
MITa599	1.210	-0.031	110	-0.0325

Table 2.1: Summary of Comparison Between Measured and Calculated Period Changes

is given by:

$$\Delta p_m = \frac{\lambda}{2} \frac{1}{b \sin\theta(1 + \tan^2\theta)} \Delta b \tag{2.12}$$

where θ is the half-angle of recombination of the two beam arms and b is the perpendicular distance from the substrate to the pinholes. One can measure the change in grating period by moving the substrate forward or backward from the reference position until the number of fringes is minimized. For sample MITa598 this required a change in b of $\Delta b = -131$ μm. Given $b = 1.093$ m, and $\theta = 26.02°$, this corresponds to a $\Delta p_m = -0.0387$ nm, which agrees closely with the value obtained directly from the HPSI analysis. For MITa599 we obtained $\Delta p_m = -0.0325$ nm. These results are summarized in Table 2.1.

The linear distortion map of MITa598 (figure 2-18b) shows that there is a magnification error of about -0.0016%, *i.e.* the regions around the outer rim of the mask have moved 3.06 μm towards the center. This makes the diameter of the membrane appear to have shrunk 6.12 μm relative to the pyrex.

This result can be explained by the differing thermal expansion coefficients of the two materials. We expect the diameter of the SiN$_x$ and the pyrex to alter through the relation:

$$\Delta d = \alpha d_0 \Delta T \quad , \tag{2.13}$$

where Δd is the change in diameter, d_0 is the original diameter, α is the thermal expansion coefficient, and ΔT is the change in temperature. For the anodic bonding conditions, the ΔT ranges is about 330°C. The thermal expansion coefficients of Si_3N_4 and pyrex are $\alpha \approx 2.7 \times 10^{-6}$/K and $\alpha \approx 3.2 \times 10^{-6}$/K, respectively. We can use equation 2.13 to calculate that the pyrex and SiN$_x$ expand by 40 μm and 34 μm, respectively. If we assume that the SiN$_x$ and the pyrex move freely against one another until the anodic bonding occurs, we would expect the differential expansion of the materials, and subsequent contraction, to make the SiN$_x$ membrane to appear have contracted by about 6 μm. This result is in good agreement with the measurement made by the HPSI.

The nonlinear distortion map, figure 2-18c, shows a maximum displacement of 0.38 μm. This is probably caused by the irregular deformation of the pyrex ring after it goes through the heating and cooling cycle. This was observed to occur during anodic bonding by placing fiducial marks on the raised pyrex rim. The marks shifted anywhere from 1 μm to 3 μm after going through a heating/cooling cycle.

Ideally, when the reference grating is repositioned in the HPSI there should be no fringes on the readout screen. This means that the reference grating is placed in exactly the same position as when the grating was originally exposed by IL, and that the samples to be measured will be similarly placed. Ferrera has analyzed in detail the phase errors resulting from differences in position and rotation between IL exposure and reinsertion for HPSI analysis [12]. The presence of fringes on the readout screen, when the reference grating is reinserted, enables one to calculate an upper limit on the absolute accuracy of the HPSI measurements. In the cases described in this paper, the reference grating produced ∼1/4 fringe on the readout screen, which corresponds to a phase excursion of $\pi/2$ radians. This in turn implies that our in-plane distortion measurements have an accuracy of ∼100 nm across the entire field. This limit can be greatly improved by improving the mounting system.

It is clear that flip-bonding the membrane introduces a significant amount of distortion. The magnification distortion can be easily corrected using any number of techniques, however the nonlinear distortion is a much more significant problem. Addressing this leads us once again into the realm of IPD measurement, but this time we need to correct the IPD as well. This leads us to out final episode in improving the x-ray mask.

2.4 The Adaptive X-ray Mask

The adaptive x-ray mask (AXM) is an approach that combines the HPSI to measure in-plane distortion, with a distortion correction method. There are a number of techniques that have been proposed in the past, ranging from using piezo-electric transducers to distort the x-ray mask periphery to depositing a correcting film to generate counter IPD. Because the ideal AXM system would operate in real-time, we chose to follow a suggestion by Feldman and correct distortion via local heating[16]. The AXM approach would consist of:

1. measuring the in-plane distortion with HPSI,
2. analytically calculating the stress distribution responsible for the distortion,
3. analytically calculating the heat-input distribution needed to cancel the stress distribution,
4. applying the calculated heat distribution, and remeasuring the in-plane distortion

This section will describe our HPSI measurements of a membrane that is distorted via local heating, and compare the measured distortion with analytically calculated values.

2.4.1 From measured distortion to stress

Kenichi Murooka, a visiting scientist from Toshiba, developed an analytical technique that predicts both in-plane distortion (IPD) and out-of-plane distortion (OPD) arising from arbitrary stress distributions in 2D[4]. Moreover, the formulation can solve the

---

[4] Finite element techniques can also perform this task, but cannot perform the inverse calculation.

inverse problem; *i.e.*, it can predict the stress distribution which, when applied to any existing distortion, eliminates it [34]. This is a technique, based on the variational method, require one to formulate the total energy that results from the membrane distortion, which is a straightforward task even for complicated stress distributions. One then iteratively searches for the distortion map that minimizes this total energy, which, according to the minimum-energy principle, should be the true membrane distortion for a given stress distribution. The inverse problem is solved analytically by performing a functional minimization on the total membrane energy, and solving for the stress distribution. The algorithm devised through this approach is both rapid and accurate [5]. An example is illustrated in figure 2-19, where a 10 mm-square membrane, made of 1 μm-thick SiN_x, is distorted by a 10 MPa absorber as shown in figure 2-19a and 2-19b. Figure 2-19c and 2-19d show the calculation of the IPD and OPD, respectively. Figure 2-19e shows the calculated stress distribution that would cause the IPD shown in figure 2-19c. There is a small residual error that results from the fact that only the IPD is considered, *i.e.* the OPD is considered small enough to be ignored. Another feature to note is the offset error, which can easily be corrected. Therefore, we can eliminate the distortion by simply changing the sign of the stress shown in figure 2-19e. We can add an arbitrary constant to the calculated stress distribution since a uniform stress does not influence the distortion.

Applying a film of material that has a controlled 2D stress distribution is both difficult and time consuming. We therefore turn to local heating.

2.4.2 Local Heating and Thermal diffusion

In order to use the calculation technique described above, we must draw an analogy between heat and stress. The relationship between stress and strain is given by:

$$\sigma = \frac{E}{1-\nu}\frac{\delta}{l} \tag{2.14}$$

where σ is the stress of the film, ν is the Poisson's ratio, E is the Young's modulus, and $\frac{\delta}{l}$ is the strain, *i.e.* the displacement of the membrane. We can directly relate the displacement caused by applying heat to that caused by a small strain through the linear thermal expansion coefficient, α. We can therefore rewrite equation (2.14) to include temperature, T:

$$\sigma = -\frac{E}{1-\nu}\alpha T \quad . \tag{2.15}$$

The minus sign is introduced because both compressive stress, which is defined as negative stress, and heating, *i.e.* applying positive temperature, cause an expansion of the membrane. By means of equation (2.15), we can use the previously described calculational techniques to analyze temperature distributions.

Through equations (2.14) and (2.15) we can relate a particular stress value to a particular temperature. However, unlike a stressed film, applied heat will diffuse away from the point of application. The simplest way to account for thermal diffusion

---

[5] The algorithm for the in-plane distortion is explained in greater detail in appendix A.

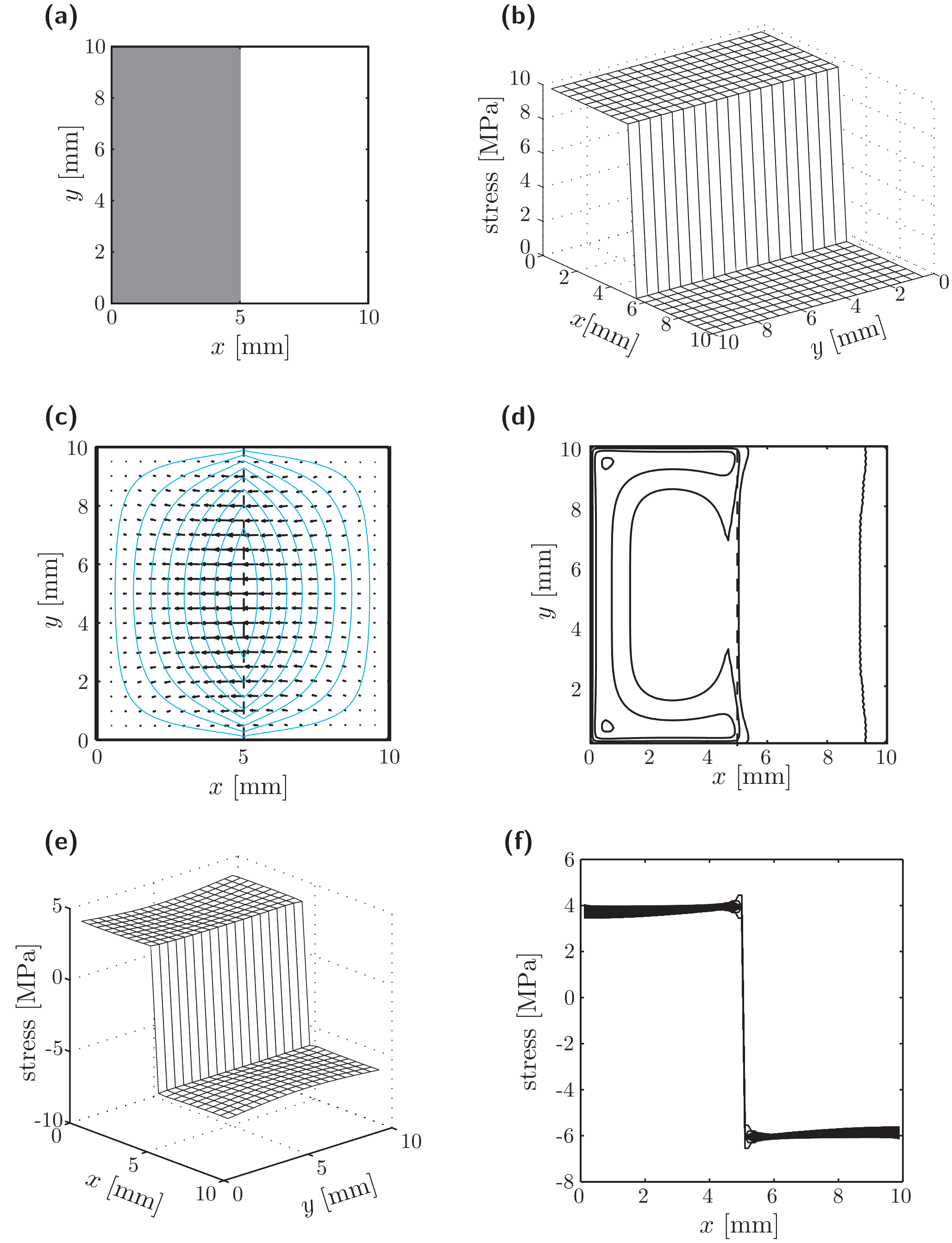

Figure 2-19: AXM calculation example of a 1 μm thick, 10 mm square SiN$_x$ membrane. (a) and (b) show a topview and perspective view of the 10 MPa tensile stress to be modeled. (c) shows the resulting in-plane distortion and (d) shows the resulting out-of-plane distortion. (e) shows the result of calculating the stress distribution given the IPD shown in (c). (f) shows various cross-sections through the calculated stress. There is an offset error that can be easily corrected. However there is some small error that results because we do not take the energy of the OPD into account

is by giving the edges of the absorber a sloped stress profile. This is a simplification of the blurring effects of thermal diffusion, which in actuality would be described via solution to the thermal diffusion equation.

Since we plan on performing the distortion correction through local heating, we must take into account thermal diffusion through the membrane, and heat loss. Thermal diffusion causes a blurring of the input heat distribution. Murooka solved this problem through the use of the heat equation, and showed that the calculation time required to incorporate thermal diffusion is less than one second [35]. For example, if one is given the IPD shown in figure 2-20(a), the variational calculational technique, described previously, predicts that the stress distribution in figure 2-20(b) would correct the IPD (if the sign were changed). In order to apply the correction to the membrane, the temperature distribution in figure 2-20(c) must be applied to the membrane. In order to obtain the equilibrium temperature distribution shown in figure 2-20(c), we must input the distribution shown in figure 2-20(d). In this example we assume a 1 μm-thick SiN_x membrane with thermal conductivity 16 W/mK and a heat loss coefficient of 26 $\mathrm{W/m^2K}$. Clearly, extra heat input at the center is necessary to obtain the desired temperature distribution. The analysis also shows that the time constant of the thermal diffusion is less than one second for a 1 μm-thick SiN_x membrane. Because the equilibrium state is expected to be reached quickly after the heat is applied, we can be confident that this technique would be useful for the AXM.

2.4.3 Heat-Input Distortion Measurements

To demonstrate the validity of our approach, we carried out the following experiments. We mounted a circular 54 mm-diameter SiN_x membrane mask, 1μm thick, in the HPSI, and impinged a 325 nm-wavelength He-Cd laser spot on it at various locations. The total He-Cd laser power was 32 mW, and the surface reflection and transmission are 19% and $\leq$ 1%, respectively. Therefore, the power absorbed in the membrane was ~26 mW. Figures 2-21a and 2-21b show contour maps of the x-component and y-component of in-plane displacement, respectively, when the laser beam is impinged at a point 10 mm to the right of center. The maximum displacement is -75 nm; successive contours differ by 10 nm. Figures 2-21c and 2-21d show contour maps of the when the laser is impinged at 20 mm to the right of center; here the maximum contour corresponds to -85 nm. To investigate the self consistency of our methods, we have taken the displacement data displayed in figure 2-21a and 2-21b, and, using the $\mathrm{Si_3N_4}$ thermal-expansion coefficient, calculated the corresponding temperature distribution, shown in figure 2-22a. From this, and assuming a heat loss coefficient of 26 $\mathrm{W/m^2K}$, and a thermal conductivity of 16 W/mK for the $\mathrm{Si_3N_4}$ membrane, we obtain the heat-input map shown in figure 2-22b. The peak temperature is calculated to be 34°C, which corresponds to about 44 MPa compressive stress on the membrane. The heat-input map of figure 2-22b appears to be a reasonable description of the impinging HeCd laser beam profile, which has a nominal diameter of 3 mm.

From the inferred temperature distribution of figure 2-22a we can calculate a resulting inferred displacement distribution, which is given in figures 2-22c and 2-22d as contour maps. These agree fairly well with the measured distortion maps of fig-

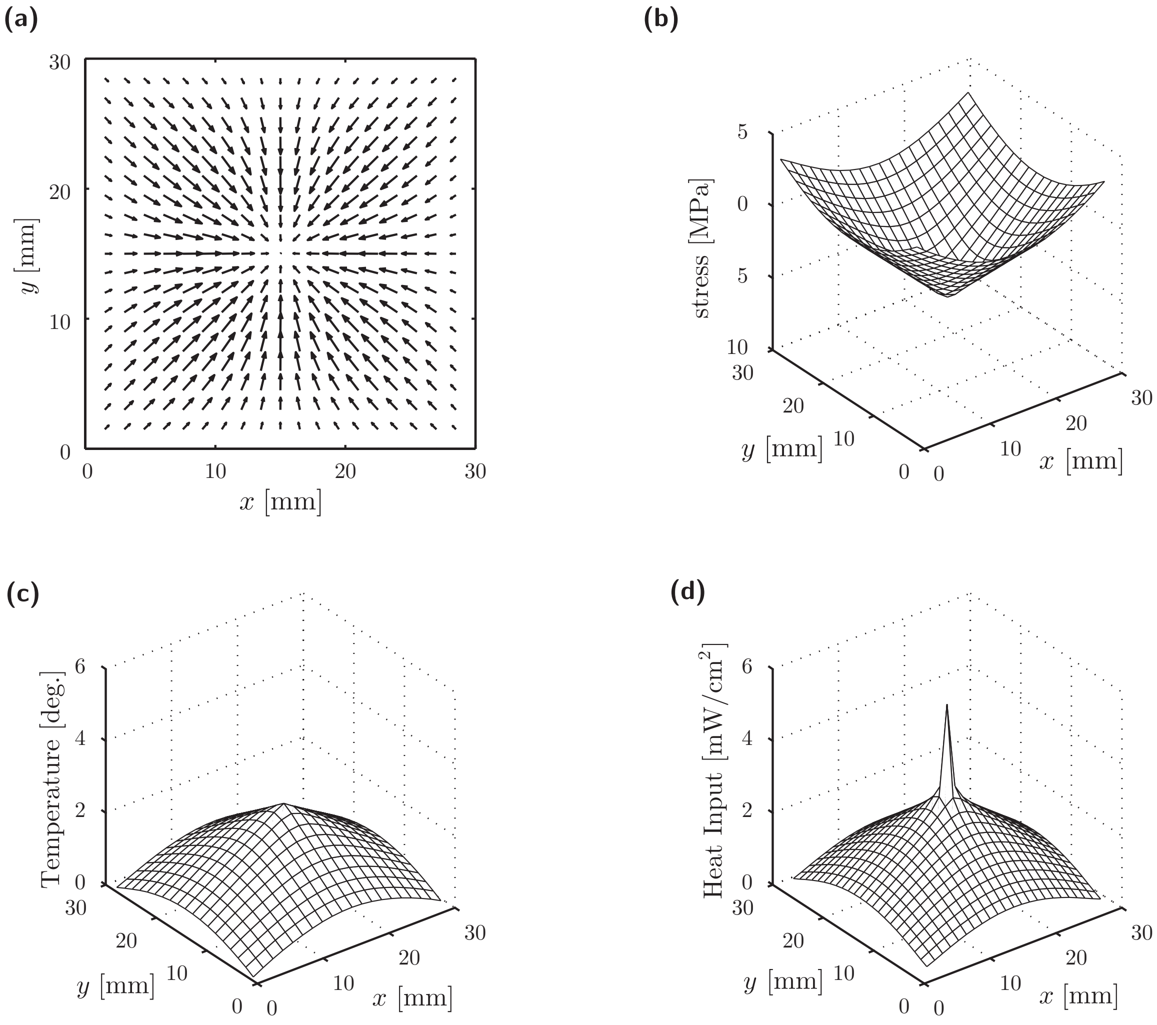

Figure 2-20: Example of distortion correction by heating. The membrane is SiN$_x$, 30 mm square, with 1 μm thickness. (a) Assumed distortion map, with a maximum displacement of 3.3 nm. (b) Calculation of the stress distribution that causes the distortion distribution of (a). (c) Calculated temperature distribution to correct the distortion distribution shown in (a), as a function of x, for a range of values of y from 15 mm to zero. (d) Calculated heat input needed to obtain the the temperature distribution shown in (c), after compensating for thermal diffusion, assuming a thermal conductivity of 16 mW/mK and a heat loss of coefficient of 26 W/m^{2}K.

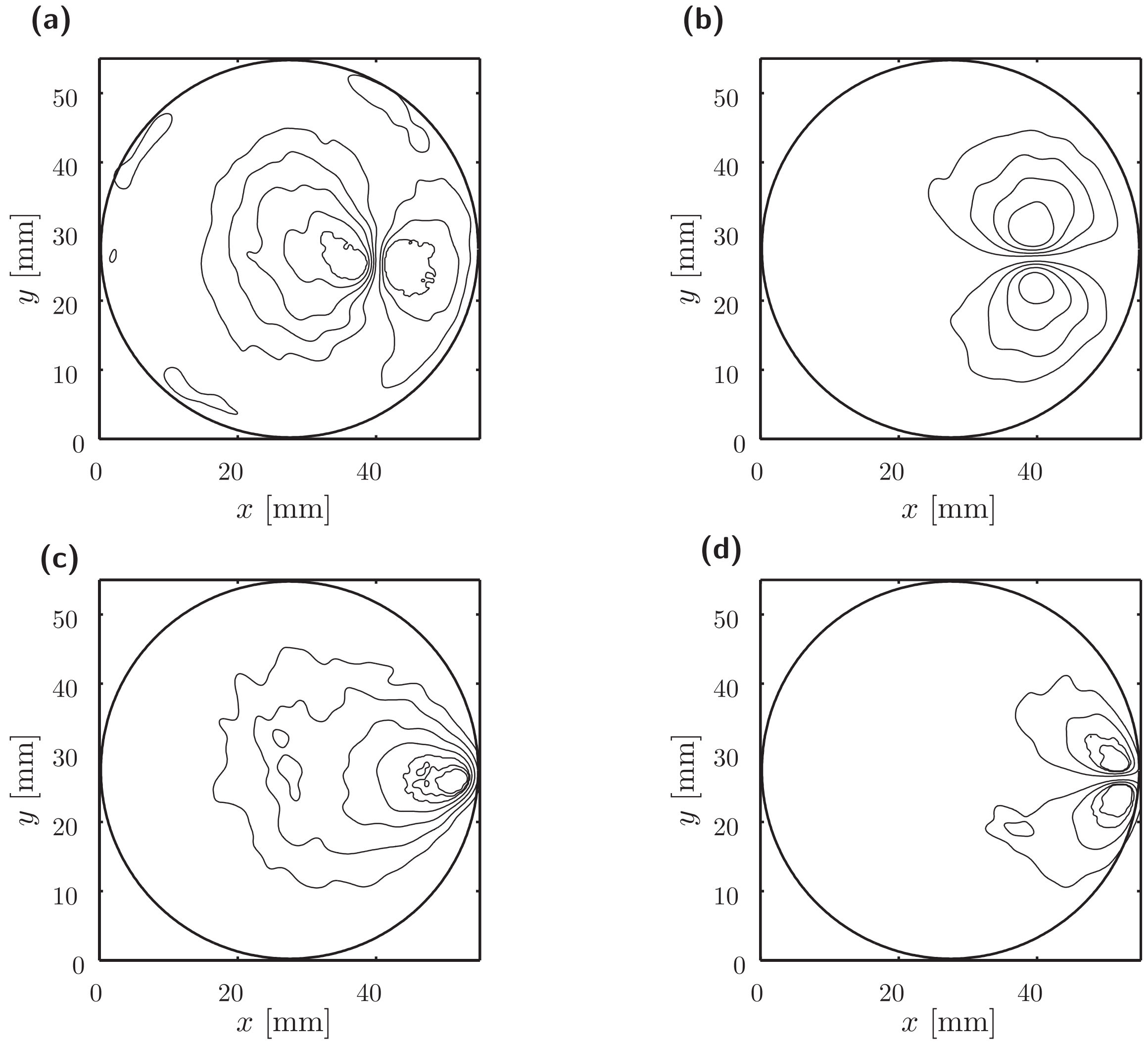

Figure 2-21: Contour map of HPSI measurements. The membrane is 54 mm in diameter and 1 μm thick SiN$_x$. (a) x-component and (b) y-component of the distortion caused by the He-Cd laser beam impinging 10 mm to the right of center. (c) x-component and (d) y-component of the distortion caused by the He-Cd laser beam impinging 20 mm to the right of center. Contours are separated by 10 nm; the maximum contour corresponds to -85 nm.

ures 2-21a and 2-21b, establishing the approximate self-consistency of our measurements and analytical techniques.

In a typical x-ray lithography exposure the mask is held in close proximity to the substrate, while maintaining a He environment. Heat is transferred through the He-filled mask-substrate gap. Assuming a gap of 20 μm and 1 atmosphere of He, the heat loss coefficient comes to ∼7,500 W/m^2 °K. This requires one to increase the correction heat input by a factor of ∼250 to achieve an equivalent level of distortion. If we take the example from figure 2-22d, and consider the heat transfer, the peak heat input required comes to ∼2,000 W/m^2 and the total input power becomes ∼0.9 W. Sources that can input this level of heat are readily available, *e.g.* an Nd-YAG laser. Additionally, the rapid heat transfer from the mask to the substrate decreases the lateral heat diffusion across the x-ray mask membrane, and therefore serve to decrease the effect of the blur.

The primary reason for the helium atmosphere is to heatsink the mask to the wafer in order to decrease temperature-induced distortion during the exposure. Because the AXM system can potentially correct these distortions, the helium atmosphere becomes unnecessary.

2.5 Summary

In this chapter the author has tried to describe the work that has gone into improving the x-ray lithography mask. This began with depositing low-stress absorber, and then improving the x-ray mask configuration, and finally developing the beginnings of a systemic solution to the x-ray mask problem. Throughout this effort a number of metrological tools were developed for the purpose of measuring the IPD and OPD of the membrane.

In the next chapter the author will discuss the application of both x-ray lithography and nanofabrication techniques to building Bragg-grating-based optical devices.

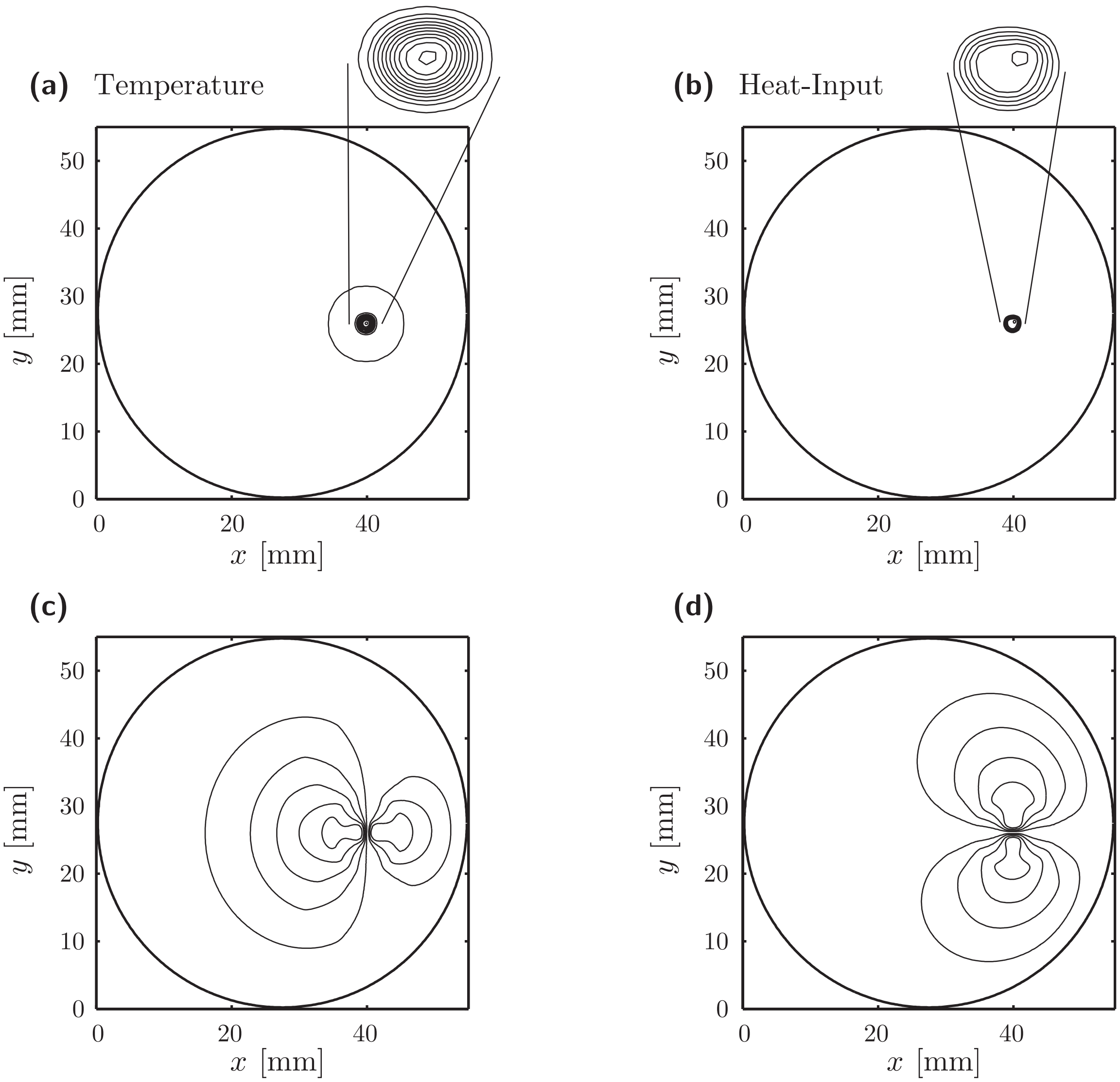

Figure 2-22: Calculation, based on our analytical model, of: (a) the temperature distribution that could cause the distortion of figure 2-21(a) and 2-21 (b). The temperature plot is magnified by the factor 6 relative to the axes; each contour is separated by 3°C. (b) Contour plot (magnified by the factor 6) of the heat input distribution corresponding to the temperature distribution shown in (a), assuming a thermal conductivity of 16 mW/m °K, and a heat loss coefficient of 26 $\mathrm{mW/m^2\,°K}$. (c) x-component and (d) y-component of the calculated distortion caused by the temperature distribution shown in (a). The range of the distortion is about -70∼65 nm.

Chapter 3

Fabrication

The term integrated microphotonics conjures up a vast array of materials, designs, and devices. The technologies being pursued range from the slightly prosaic, UV-induced Bragg-gratings in silica fiber [7], to the exotic, 3D-photonic bandgap materials formed by self-assembled colloids [36]. In selecting the device to drive the fabrication technology, the author attempted to thread a middle path between banality and fantasy. We chose to use InP-based materials because it can be formed into both 1.55 μm-wavelength lasers and low-loss passive devices. We chose to pursue Bragg-grating-based designs because, despite the flexibility afforded by their nature, their application in integrated-optical devices has been limited to relatively simple components; due, in part, to the technical challenges in fabricating such structures. This chapter calls attention to these unique challenges and presents a process sequence which solves some of the critical problems[1].

The device that we chose for driving the development of the fabrication technology was the channel-dropping filter (CDF), depicted in figure 3-1 [38]. The function of the CDF is to drop (or add) one wavelength-channel from a multi-channel bus. The filtering takes place in the quarter-wave-shifted Bragg gratings located above and below the bus waveguide. Because of the wavelength-selective nature of the Bragg gratings, they act as narrow-band resonators which are only excited by one wavelength. The details of the CDF design and operation can be found elsewhere. This chapter concerns itself primarily with the minutia of building an integrated-optical device with precisely placed gratings.

3.1 Fabrication Challenge and Process

Nanolithography

The first challenge presented by the channel-dropping filter depicted in figure 3-1 is the ~244 nm grating period, which is beyond the capability of conventional lithog-

---

[1] Even though it seems *de rigueur* for authors to include a chapter on coupled-mode theory, which explains the theoretical underpinnings of the Bragg grating, this author feels that inclusion of such a chapter would be redundant in light of all the reviews already published. An excellent review of coupled-mode theory can be found in chapter 2 of reference [37].

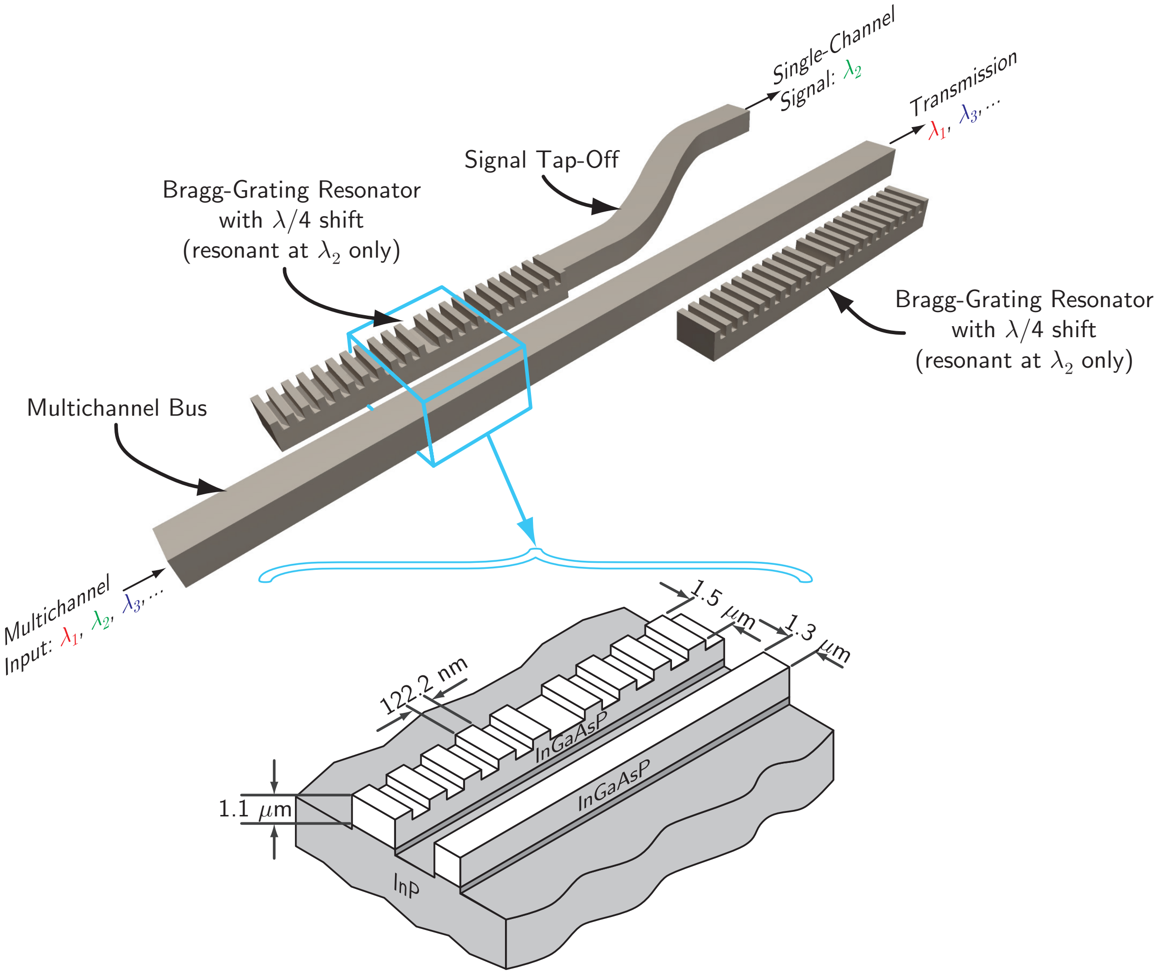

Figure 3-1: Diagram of the quarter-wave-shifted distributed-feedback channel-dropping filter (CDF) which is designed to take a multichannel input and spatially separate a single channel while passing the remaining channels unaltered. In order to fabricate such a structure, 244.4 nm-pitch gratings, with quarter-wave shifts, must be precisely placed on top of large waveguides. Because of the dramatic scale difference between the waveguide widths (~1 μm) and the gratings (~0.1 μm), controllable fabrication of the CDF structure required development of a dual-layer-hardmask process.

raphy techniques; according to the SIA roadmap (table 1.1) such gratings will not be printable until ~2005. The presence of an abrupt quarter-wave shift in the grating rules out the use of interference lithography[2], which otherwise could be used to produce such gratings directly onto the substrate. In order to fabricate grating filters that include one or more quarter-wave shifts, a more flexible lithography tool, such as electron-beam lithography, must be employed to write the lithography mask. It will not be a surprise to the reader to learn that the author feels that x-ray lithography is ideal for printing these quarter-wave shifted gratings.

Long Range Coherence

A second requirement of the Bragg grating, which is not apparent from figure 3-1, is that the grating must be spatially coherent over its entire length; the Bragg grating is several hundred microns to millimeters in extent. Once again, were it not for the quarter-wave shifts, interferometric lithography would be ideal to produce high-quality long-coherence length gratings. Unfortunately, since the mask must be written by e-beam lithography, numerous e-beam write fields must be stitched together. Any appreciable field-stitching errors at the boundaries between these adjacent e-beam fields results in a phase error in the Bragg grating. Stochastic modeling has shown that one must hold the field-stitching error to ≤ 5 nm in order to avoid phase-errors that can cause several deleterious effects in filter function [39]. Spatially phase-locked e-beam lithography (SPLEBL) was developed by Ferrera and is ideal for this task [40].

Grating Period Control

For the channel-dropping filter, and more generally for all Bragg-grating-based filters, the operating frequency is determined by the grating period. Therefore, in order to build a narrowband filter for a WDM system, we must maintain precise control of the Bragg grating period. To illustrate this requirement, consider two consecutive wavelength channels in a dense WDM system, separated in optical frequency by 100 GHz. If a filter is to operate on one of these channels without affecting the other, the period of the Bragg grating must be controlled to within 0.1 nm. The details on accomplishing this task is described in reference [12].

Alignment

Two levels of lithography are required for fabricating the channel-dropping filter shown in figure 3-1: one that defines the waveguide features and a second that defines

---

[2] There are two techniques that one could use to make an abrupt quarter-wave shift using IL alone. The first involves using positive resist on one-half of the substrate and negative photoresist on the other half. With careful control, a single IL exposure could potentially print an abrupt $\lambda/4$-shift. The second involves a standard IL exposure, transfer of the grating into a thick layer of SiO_2, protection of certain regions with photoresist, and then liftoff of the oxide (depositing a metal such as chrome and dissolving the oxide in an acid such as buffered hydrofluoric acid) in the unprotected regions. While both techniques are certainly realizable, they are imprecise and not amendable to defining higher-order filters that contain more than one abrupt $\lambda/4$-shift.

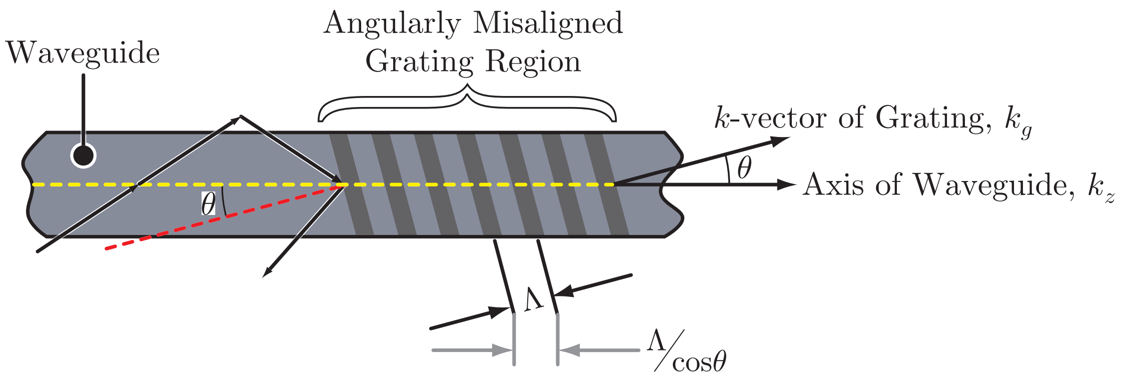

Figure 3-2: In addition to the traditional lateral alignment problem that is commonly encountered in fabrication, the k-vector of the grating must be precisely aligned to the waveguide axis. Misalignment will have two effects: (1) any angular misalignment between the grating and the waveguide axes will cause an effective lengthening of the grating period; (2) large angular misalignments will increase the scattering of the mode out the waveguide.

the fine-pitch gratings on top of the waveguide. Naturally, these two levels of lithography must be aligned relative to one another. In addition to the normal requirements of pattern overlay, the Bragg grating must be oriented such that its k-vector is precisely aligned to the waveguide axis. As depicted in figure 3-2, any angular misalignment between the grating and the waveguide axes will cause an effective lengthening of the grating period. Thus, in order to precisely control the operating frequency of the filter, not only must we precisely control the Bragg period as described above, but we must also maintain angular alignment between the grating and the underlying waveguide patterns. Moreover, if the angular misalignment is large the mode will scatter out of the waveguide and show high loss.

Nanolithography over Topology

Another challenge presented by the channel-dropping filter is that the fine-period grating structures must be patterned on top of relatively tall waveguide structures. Figure 3-3a illustrates how attempting to spin a coating of high-resolution photoresist onto a substrate with 1.1 μm-tall features invariably results in uneven resist coverage, which leads in turn to unreliable patterning. In order to avoid this topography problem, we have developed a technique, that we call the Dual-Level-Hardmask Process (DLHP), depicted in figure 3-3b. The DLHP places both the coarse and fine etch-mask features onto the substrate prior to etching, thereby avoiding the problem of patterning over large features. We detail the full integration of the process in section 3.3.

Finally, once the structure is fabricated, a layer of InP cladding must be deposited, while maintaining the underlying structure of the device. We next discuss InP etching.

(a) Problem: uneven resist coverage

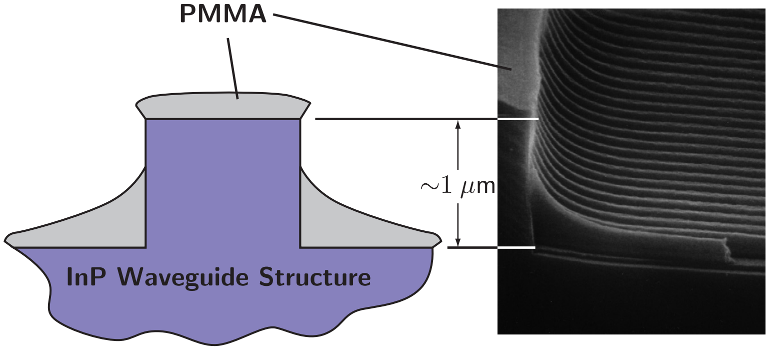

(b) Solution: Dual-Layer Hardmask Process

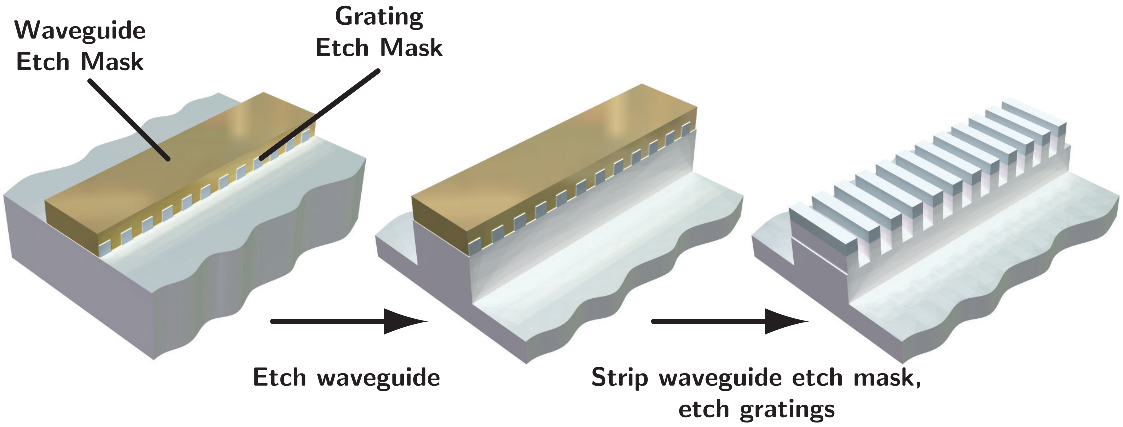

Figure 3-3: The most obvious way to pattern gratings on top of a waveguide would be to form the waveguide and then spin on the resist to pattern the grating. (a) The problem with this approach is that the ~ 1 μm tall waveguides would cause extremely uneven photoresist coverage leading to very poor grating reproduction. (b) The solution to this problem is the patterning of two hardmasks, one of the waveguide and the other for the grating, directly onto the substrate; then, through a series of etch steps, the grating on waveguide structure can be formed. This approach as the distinct advantage that all the processing can be performed on an essentially planar substrate.

3.2 InP Etching

Etching is the removal of substrate material through chemical or kinetic means. Wet etching is a common chemical technique in which an acidic or basic solution reacts with the substrate and forms byproducts that dissolve in solution. Chemically-based etching techniques usually result in isotropic etch profiles[3] which limits the application of this techniques to larger features.

Reactive-ion etching (RIE) uses both chemical and kinetic reactions to achieve higher fidelity and directional etch results. There are four primary RIE configurations:

RF-diode: this is the most common configuration and consists of a two-plate cavity, with the RF-power input through a blocking capacitor. This excites the plasma and causes the cathode to self-bias to a level that depends on the amount of power delivered and the ratio of area between the powered and grounded electrodes.

electron-cyclotron resonance (ECR) uses a microwave generator and cavity to create the plasma. The substrate is biased by RF-power delivered through a blocking electrode. In an ECR system, the acceleration voltage and the plasma density can be set independently.

inductively-coupled plasma (ICP) is similar to an ECR system, except that it uses an inductive coil, generally exterior to the chamber, to excite the plasma;

chemically-assisted ion beam (CAIBE) uses an inductive coil to generate the plasma, but the plasma is typically Ar (which is non-reactive alone); a biased grid extracts Ar-ions and directs them towards the substrate where a reactive gas, such as chlorine, is fed. The Ar-ions both excite the substrate atoms and sputter the substrate.

In all the RIE configurations an electric field accelerates reactive ion species, in the form of a plasma, into the substrate. The substrate is etched through a combination of sputter etching, whereby kinetic energy from the accelerated ions physically displace substrate material, and chemical etching, whereby the substrate material reacts with the radicals to form a volatile species. RIE can successfully etch extremely fine features.

3.2.1 Reactive-Ion Etching InP

As noted in section 3.1, fabricating integrated-optical devices requires defining fine features. This implies that the InP/InGaAsP must be etched using an RIE process.

Reactive ion etching (RIE) of InP can be accomplished through two etch chemistries:

1. halogen-gas-based chemistries, *e.g.* Cl_2, HCl, HBr, HI, *etc.*;

---

[3] The unusual exception being that under specific conditions, and in silicon and III-V single crystal semiconductors, etching will take place much more slowly into the $\langle 111 \rangle$ crystallographic planes.

	F	BP(°C)	**Cl**	BP(°C)	**Br**	BP(°C)	**I**	BP(°C)
Al	AlF_3	*subl.* 1291	$AlCl_3$	262	$AlBr_3$	263.3	AlI_3	360
Ga			$GaCl_2$	535				
	GaF_3	*ca.* 1000	$GaCl_3$	201.3	$GaBr_3$	278.8	GaI_3	*subl.* 345
In			InCl	608	InBr	*subl.* 662	InI	711–715
			$InCl_2$	530–570	$InBr_2$	*subl.* 632	InI_2	*volat.* 720
	InF_3	> 1200	$InCl_3$	*volat.* 600	$InBr_3$	*subl.*	InI_3	*volat.* 505
P	PF_3	-102	PCl_3	76	PBr_3	173	PI_3	227
	PF_5	-85	PCl_5	160	PBr_5	106		
As	AsF_3	58–63	$AsCl_3$	130	$AsBr_3$	221	AsI_3	400–424
	AsF_5	-52.8						

	H	BP(°C)
P	PH_3	-88
	P_2H_4	-99
As	AsH_3	-62.5
	As_2H_4	100

Table 3.1: Boiling points (BP) of possible etch products of halogen-gas-based InGaAsP RIE etching. This data can only be used as a starting point in choosing etch chemistries. Volatility of etch products is strongly influenced by ion bombardment, which is ignored when determining boiling points. From reference [41].

2. hydrocarbon-based chemistries, *e.g.* CH_4/H_2.

Each chemistry has its own characteristics which make it suitable for different applications. In general, the halogen-gas-based chemistry etches more rapidly, while the hydrocarbon-based chemistry results in smoother surface morphologies. The author chose to etch InP/InGaAsP using a hydrocarbon-based chemistry for two reasons: (1) regrowth requires smooth surface morphologies, (2) halogen-based etches are extremely aggressive, and therefore limiting in terms of etch mask choices. The background discussion below will briefly present both chemistries since the author presumes that the reader is interested in processing InP/InGaAsP in general.

Halogen-Gas-Based Chemistries

A number of halogen gases have been investigated for the etching of InP. The suitability of a specific gas can be determined by examining the boiling points or vapor pressure of possible end products; table 3.1 summarizes boiling points and vapor pressures for various possible end products of a halogen-gas-based RIE. From table 3.1 one can draw some initial conclusions about InP/InGaAsP etching in halogen gases. One would expect the primary etch products to be $GaCl_3$, $InCl_3$, $AsCl_3$, and PCl_3 if using pure Cl_2.

Early etching took place using chlorine-containing gases such as Cl_2 and CCl_4 [42, 43, 44]. Other gas mixtures used for etching include BCl_3, $SiCl_4/Cl_2$, $CHCl_3$, $COCl_2$, CCl_2F_2. Freon 12, *i.e.* CCl_2F_2, is a particularly attractive gas due to its non-toxic and non-corrosive properties. Moreover when using freon 12, Hu *et al* selectively etched GaAs/InGaAs over AlGaAs with ratios of several hundred [45]; it is thought that fluorine combines with aluminum to form the involatile compound AlF_3. Unfortunately, freon 12 is an ozone depleting compound.

While GaAs compounds can be etched using these chlorine containing compounds with generally excellent results (high anisotropy and etch rate), it was found that $InCl_3$ would not desorb unless the substrate was heated to $\geq 130°C$; note that table 3.1 indicates that one should expect $GaCl_3$ to be much more volatile than $InCl_3$. Etching In-containing materials below this temperature results in both slow etch rates and rough surface morphologies.

To solve these short-comings, researchers made attempts to use iodine-based chemistries. Flanders *et al* were the first used iodine containing plasmas to etch InP-based semiconductor lasers [46]. They achieved high etch rates and reasonable surface morphologies in an RF-diode system using two gas combinations: Ar/HI and H_2/HI/CH_4. This can be attributed to the lower volatility temperature of InI_3 with respect to $InCl_3$. Pearton *et al* used an H_2/HI gas chemistry, in an ECR configuration, to etch In-containing surfaces with high etch rates, high anisotropy, and smooth surface morphologies; moreover, the etched surfaces were stoichiometric [47]. Because of the extremely corrosive nature of HI, Chakrabarti *et al* made efforts to use less corrosive iodine-based gases (CH_3I, C_2H_5I, and C_3H_7I) also in an ECR configuration. They too achieved good results.

Hydrocarbon-Gas-Based Chemistries

Etching with hydrocarbon gases first took place by Niggebrugge *et al.* [48]. The etching of InP and its alloys results from their reactions with the ionization products (reactants) of the H_2/CH_4 which arise from the RF excitation. The reactants are thought to be:

$$\begin{aligned} \mathrm{CH_4} &\rightarrow x\mathrm{CH}_3^* + y\mathrm{CH}_2^* + z\mathrm{CH}^* + \mathrm{ions} \\ \mathrm{H_2} &\rightarrow x'\mathrm{H}_2^+ + y'\mathrm{H}^* + \mathrm{protons} \quad . \end{aligned}$$

These reactants react with the InP, and its alloys, in essentially the reverse of the MOCVD process:

$$\begin{aligned} \mathrm{In} + 3\mathrm{CH}_3^* &\rightarrow \mathrm{In}\left(\mathrm{CH_3}\right)_3 \\ \mathrm{P} + 3\mathrm{H}^* &\rightarrow \mathrm{PH_3} \quad . \end{aligned}$$

The etch products of the III-V etching were confirmed by Melville *et al* [49, 50]. In their experiment an electron-cyclotron resonant (ECR) dry etching system was used to etch InP while a quadrupole mass-spectrometer was used to identify the constituents in the chamber; table 3.2 summarizes the volatile species detected. This summary indicates that the organic-species are important in the etching of the indium. It also indicates that sputtering is an important component in the removal of indium.

Indium Volatiles	Phosphorous Volatiles
$In(CH_3)_2^+$	PH_3^+
In^+	PH^+
$In(CH_3)^+$	PH_2^+
$HInCH_3^+$	$H_2P(CH_3)_2^+$, PCH_3^+

Table 3.2: Species found in chamber while etching InP ranked in order of species quantity. This summary of reference [49, 50] indicates that the organic-species are important in the etching of the In. It also indicates that sputtering is an important component in the removal of In. We focus our attentions on In because the phosphorous containing compounds are generally much more volatile (see table 3.1).

Etching Studies

The RIE system in the NSL has an RF-diode configuration. Figure 3-4 shows an etch series where the methane:hydrogen ratios were varied. The substrate is an InP wafer that has been patterned with a 4 μm-period grating in 30 nm thick titanium. The grating was patterned via optical proximity lithography and liftoff. It is very apparent that etching in a hydrogen-rich chemistry results in a rough surfaces and that, as one would expect, the indium requires the reactive methane species to desorb.

Even with an equal flow of hydrogen and methane, the surface still remains slightly rough. If the methane flow is increased beyond the hydrogen flow, an unacceptable amount of polymer forms which slows the etch rate. A small amount of chlorine gas was added to the system in the hopes of aiding in the desorption of the indium. The hope was that even though PCl_3 is expected to be much more volatile than $InCl_3$ that the indium rich surface of the substrate would favor $InCl_3$ formation. Figure 3-5 shows that the adjusted chemistry results in surfaces that are significantly smoother. Unfortunately, chlorine also aggressively attacks the titanium etch mask, resulting in sloped sidewalls.

Figure 3-6 shows deep waveguide-type etching using various hydrocarbon chemistries. Figure 3-6a shows an etch where the methane portion of the chemistry was scaled back while the chlorine portion was increased. This was an attempt to test whether the chlorine gas could aid in the indium removal from the surface in lieu of the methane; the slightly rough surface indicates that it cannot. Another point to note is the etch profile is slightly sloped. There are two potential causes for this effect:

1. the chlorine gas is eroding the titanium mask (chlorine is an excellent titanium etchant);

2. a polymer coating is building up on the titanium mask and ballooning out, effectively making the mask look larger over time (this effect is commonly seen in hydrocarbon-based etching of InP).

- CH_4:H_2 at 10:40 sccm
- 10 mT Chamber Pressure
- 3 min etch

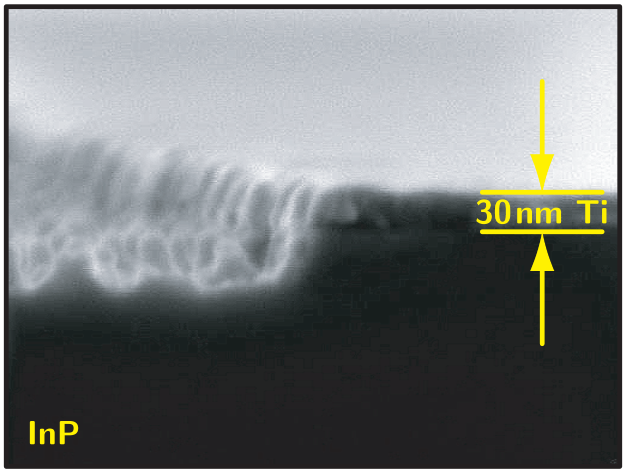

- CH_4:H_2 at 15:30 sccm
- 10 mT Chamber Pressure
- 3 min etch

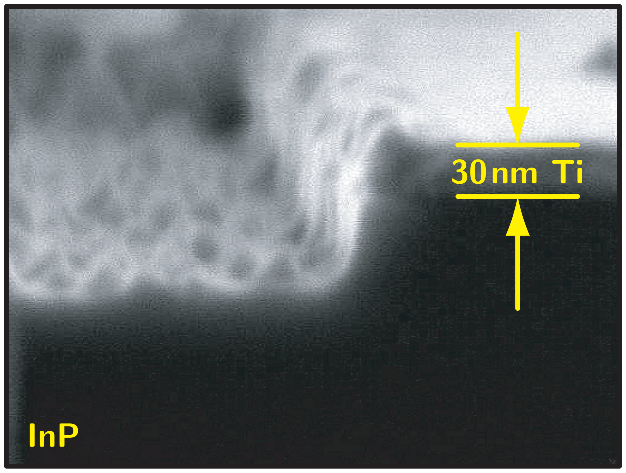

- CH_4:H_2 at 20:20 sccm
- 10 mT Chamber Pressure
- 3 min etch

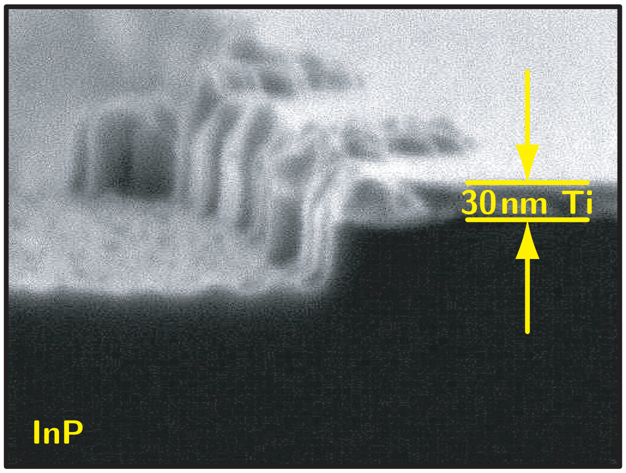

Figure 3-4: Hydrocarbon etching at various flow ratios. All the etches used a 30 nm thick film of Ti as the mask. As the flow rates between the CH_4 and the H_2 become more equal the resulting etched surface improves. This is expected since the dominant In removal process occurs via the reactive methane species.

- CH_4:H_2:Cl_2 20:20:4 sccm
- 10 mT Chamber Pressure
- 3 min etch

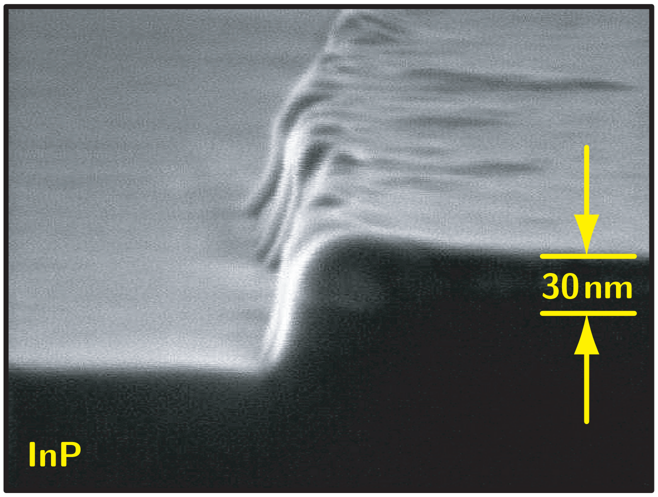

Figure 3-5: Hydrocarbon etching with inclusion of Cl_2. The adjusted chemistry results in surfaces that are significantly smoother. The chlorine also aggressively attacks the titanium etch mask resulting in sloped sidewalls.

In order to improve the profile, several mixtures were attempted. Figure 3-6(b) shows a particular example where two adjustment were made:

1. a small oxygen flow has been added in order to decrease polymer buildup;
2. the chlorine flow has been decreased, in order to slow the titanium etch rate, and the hydrogen flow has been increased in order to increase the indium removal.

These changes should decrease the etch profile's slope, but as one can clearly see in the figure the profile shows no noticeable improvement although the etched surface is exceptionally smooth. Figure 3-6c shows an example where the chlorine flow rate has been further reduced. It is clear that the chief cause of the sidewall slope, in this etch chemistry, is the titanium erosion caused by the chlorine gas. The surface in this case has become slightly rougher.

Figure 3-7 shows a mixture where the chlorine gas has been removed in order to make the profile as vertical as possible. The figure shows that the etch result is generally excellent with smooth etched surfaces and vertical etch profiles.

3.2.2 Regrowth over Etched Surfaces

Because we are trying to fabricate a buried core type device, we must be able to regrow high-quality optical material over the substrate without compromising the underlying structure. There are two dominant technologies for accomplishing this task: molecular-beam epitaxy (MBE) and metallo-organic chemical-vapor deposition (MOCVD). Here the author describes over growth using a gas-source MBE technique.

Rectangular-patterned gratings, similar in dimension to those required by the Bragg-resonant filters, are fabricated in InP substrates via x-ray lithography and RIE. After deposition of SiO_2 and polymethyl methacrylate (PMMA), the sample is placed

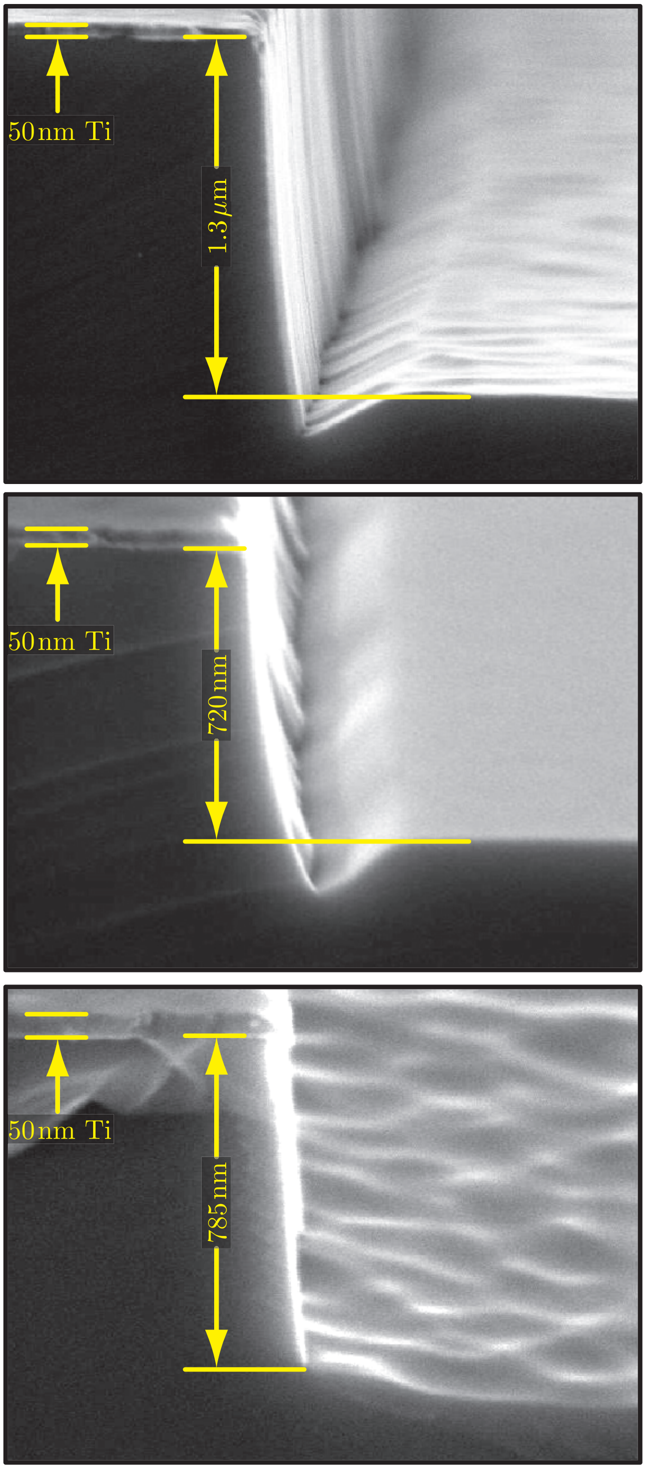

(a)

- CH_4:H_2:Cl_2 10:20:10 sccm
- 5 mT Chamber Pressure
- 30 min etch

(b)

- O_2:CH_4:H_2:Cl_2 2.5:20:20:4 sccm
- 5 mT Chamber Pressure
- 30 min etch

(c)

- O_2:CH_4:H_2:Cl_2 2.5:20:20:1.5 sccm
- 5 mT Chamber Pressure
- 30 min etch

Figure 3-6: Deep etching of InP using a hydrocarbon-halogen etch chemistry. (a) shows a sloped profile resulting from etch mask erosion and/or polymer buildup on the etch mask. (b) decreasing the Cl_2 flow and adding O_2 should improve the profiles, but clearly does not. (c) decreasing the Cl_2 portion improves the profile considerably, indicating the primary cause of the sloped profile is erosion of the etch mask.

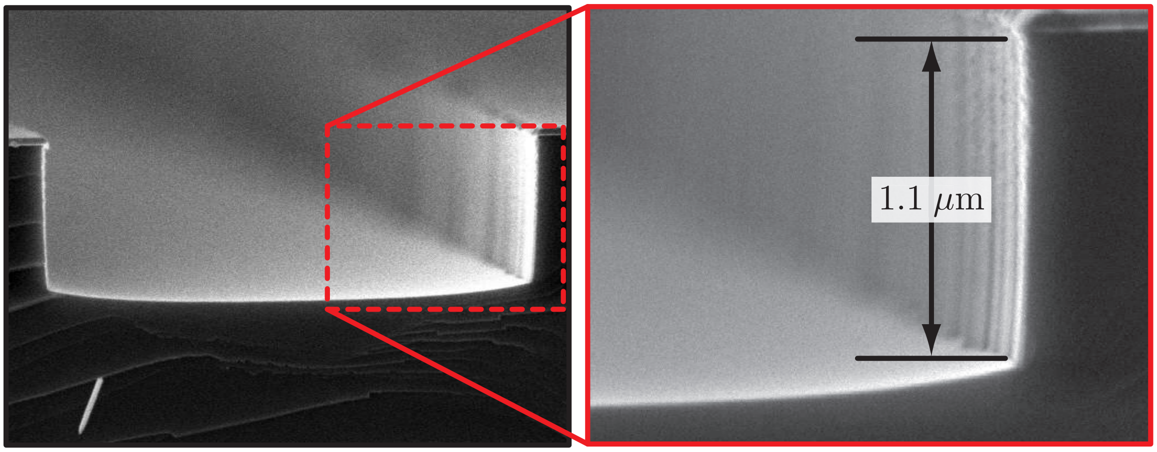

Figure 3-7: Etching InP in CH_4:H_2:O_2, with the rates 20:20:2.5 sccm, results in vertical profiles and smooth surfaces. The RIE was held at a 400 VDC self-bias, which required a power input in the range of 90–120 Watts. The chamber was held at a 5 mTorr pressure. This is a generally excellent etch which is used for all subsequent InP etching.

in electrostatic contact with the x-ray mask and exposed. Following development of the PMMA, RIE transfers the 230 nm period grating pattern (having equal lines and spaces) first into the SiO_2 mask and then into the InP, achieving vertical sidewalls to depths of 110 nm.

Initially the over growth was performed by Koontz *et al.* using a gas-source MBE. First results proved very promising [51], shown in figure 3-8, however these results could not be repeated. It was hypothesized that this failure to reproduce the initial results was due to the fact that the first etch was uniquely smooth and that every subsequent etch was intolerably rough [52].

Moreover, only regrowth of InGaAsP over InP was attempted; while interesting and potentially useful, this is not the correct material for completing the cladding layer of InP-based optical devices. Intuitively, growing InP over InGaAsP seems simpler, however this growth achieved only mediocre success. Figure 3-9 shows overgrowth of InP over InGaAsP material. In all cases the regrown layer was polycrystalline in nature and resulted in a significant amount of intrinsic waveguide loss [53]. While acceptable for active devices this type of intrinsic loss has highly deleterious effects for narrow-band filters.

Since reference [52] hypothesized that this polycrystalline growth was due to the fact that the first etch was uniquely smooth and that every subsequent etch was intolerably rough, we study the smoothness of the etched surfaces.

Smoothness of Etched Surfaces

The author used a Digital Instruments, model 9000, atomic force microscope to determine the smoothness of the etched samples. The instrument uses an algorithm that analyzes the power spectrum of the surface variation to determine the roughness of the

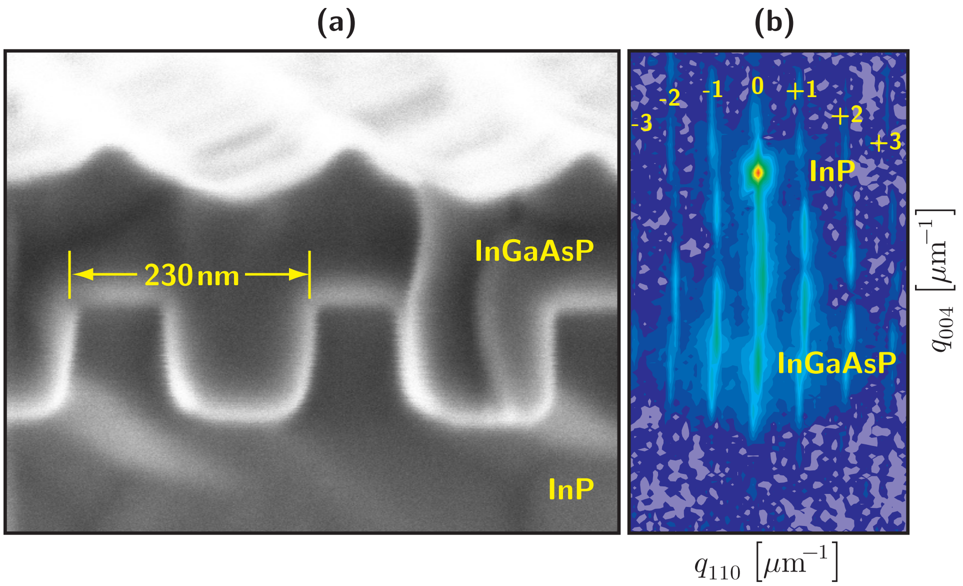

Figure 3-8: (a) shows the result of high-quality gas-source MBE regrowth over InP; the grating profile is well maintained. (b) is a 3D x-ray diffraction plot of the sample; the strong sidelobe peaks indicate high-quality gratings in both the InP and InGaAsP.

sample. This is a commonly used technique to analyze surface roughness [54, 55, 56]. Figure 3-10 shows a surface-morphology comparison of unprocessed InP and dry-etched InP. The unprocessed InP is extremely smooth, as one would expect, with a root mean square (RMS) roughness of 0.6 nm. Before etching InP, the RIE chamber was thoroughly cleaned and prepared by running the InP-etch recipe for 30 minutes. After etching InP for 30 minutes the RMS figure increased to 2.0 nm.

As mentioned above, there is some concern that the etched surface smoothness quality decreases over time as polymer builds up on the walls of the RIE chamber. To test whether or not this is the case, three additional InP samples were etched, each for 30 minutes, in succession. The RIE chamber was left alone in between the etches. Figure 3-11a shows the first sample that was etched for 30 minutes; the RMS roughness of the etched surface was 1.8 nm. Figure 3-11b shows the sample that was etched immediately afterwards; the surface shows an RMS roughness of 2.9 nm. Figure 3-11c shows the third etched sample with an RMS roughness of 2.0 nm. While certainly not conclusive proof, this series of etches shows that under the most common operating circumstances the etched surface of the InP remain smooth and fine.

To test whether the etch results would differ when etching quaternary materials, we etched and analyzed InGaAsP material, purchased from the EPI corporation, that could eventually be used as our optical substrate material. Figure 3-12a shows the surface morphology of an unprocessed MOCVD-grown wafer. The wafer shows a surface roughness of 3.0 nm. After the sample is dry-etched for 11 minutes, it shows an RMS surface roughness of 3.7 nm.

From the above experiments one can see that there is a definite increase in surface

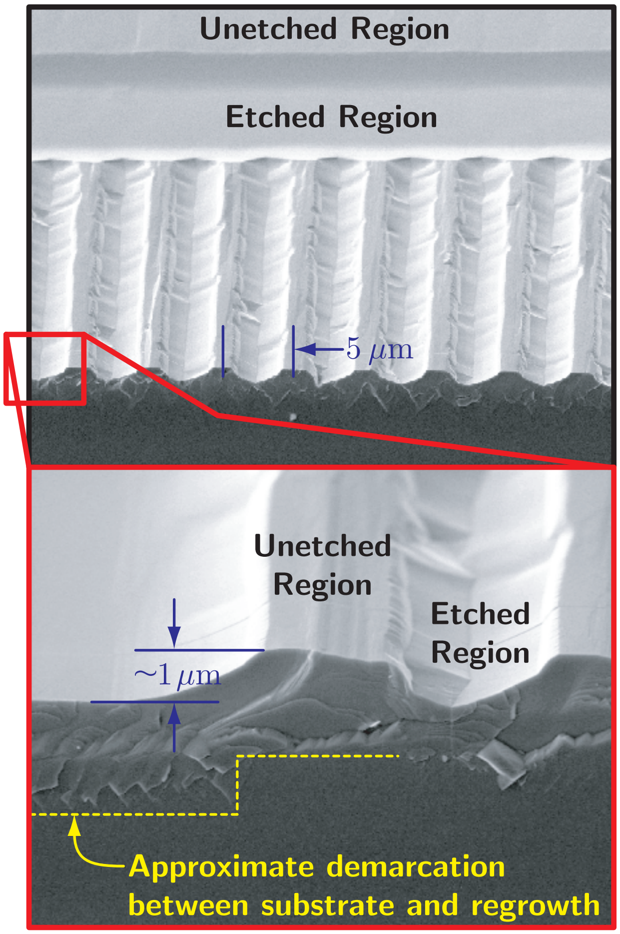

Figure 3-9: InP regrowth over waveguide type structures shows the polycrystalline nature of the regrowth. As a result the waveguides made from this sample resulted in high loss

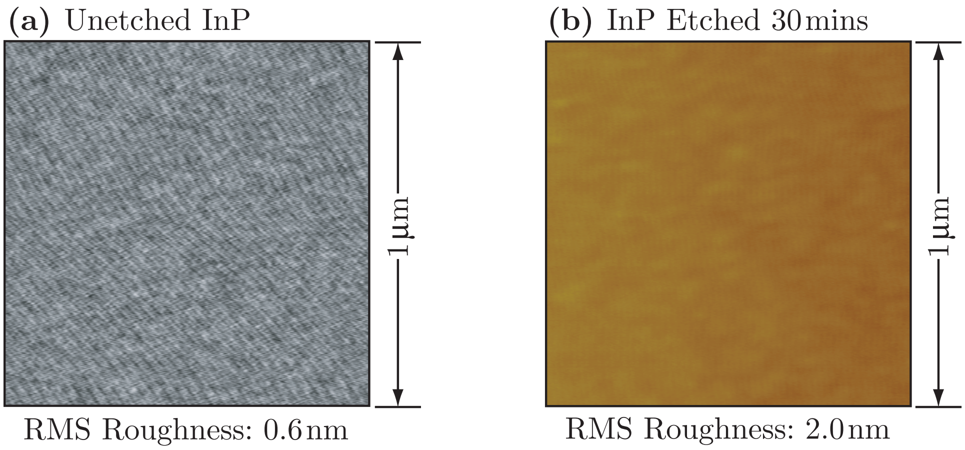
(a) Unetched InP

(b) InP Etched 30 mins

RMS Roughness: 0.6 nm

RMS Roughness: 2.0 nm

Figure 3-10: Smoothness comparison of virgin InP to etched InP. (a) shows an AFM scan of an InP wafer, that has seen no processing, with a surface roughness figure of 0.6 nm. (b) shows an AFM scan of an InP wafer that has been dry-etched for 30 mins; it shows a surface roughness figure of 2.0 nm.

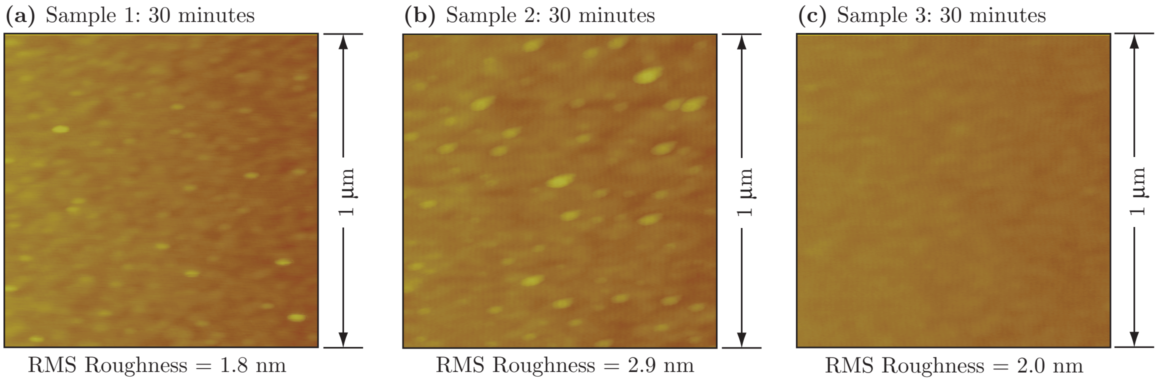

Figure 3-11: Successive dry-etching of InP does not increase the surface roughness of the etched surfaces. (a) shows a sample that has been etched for 30 minutes resulting in a surface roughness of 1.8 nm. (b) shows another sample that was etched immediately afterwards; the surface shows a roughness of 2.9 nm. (c) shows a third etched sample with surface roughness of 2.0 nm. It is clear from the series of etches that the surface roughness remains constant and smooth.

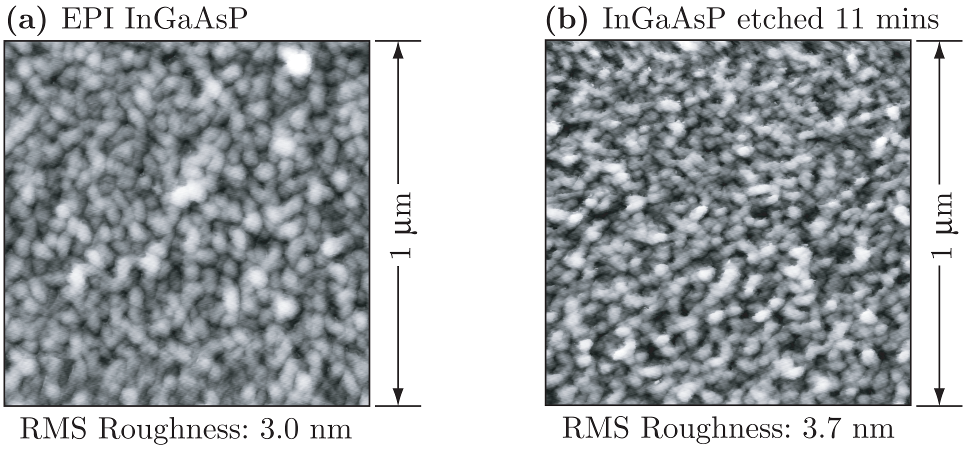

Figure 3-12: Smoothness comparison of MOCVD InGaAsP to etched InGaAsP. (a) shows an AFM scan of an MOCVD-grown InGaAsP wafer, that has seen no processing, with a surface roughness figure of 3.0 nm. (b) shows an AFM scan of the same wafer after it has been dry-etched for 11 mins; it shows a surface roughness figure of 3.7 nm.

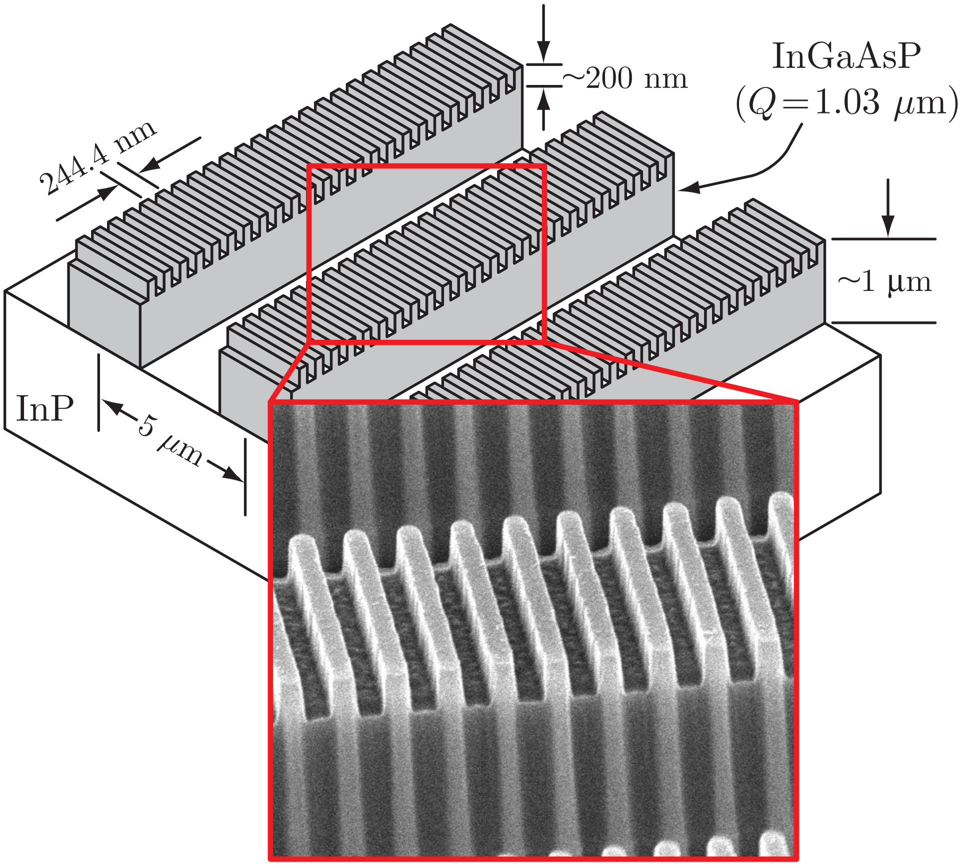

Figure 3-13: The MOCVD regrowth test sample consists of 244.4 nm pitch gratings on top of 1.1 μm waveguides. These structure mimic the structure of channel-dropping filter.

roughness over an unprocessed InP wafer, but the resulting etched surface is always as smooth as the best results attained in the literature [54, 55, 56]. Additionally it is clear to the author that if the regrowth techniques described in reference [52] could not regrow on the surfaces with 3 nm of roughness that another regrowth technique had to be sought.

MOCVD Regrowth over Square Gratings

To test the ability of MOCVD to regrow over square-profile gratings, while maintaining the profiles, a sample was sent to Charles Joyner, of Lucent Technologies. Figure 3-13 shows a schematic and SEM of the sample which consists of a 244.4 nm-period grating, etched to a depth of 220 nm, on top of large waveguide-type structures. Prior to sending the sample to Charles Joyner, it was dipped in hydrofluoric acid, cleaned in hot-NMP, acetone, methanol, isopropanol, and finally rinsed in DI-water.

Before regrowth, Charles Joyner dipped the sample in a weak acid. Because MOCVD is a high-temperature process, more care must be taken in order to maintain the grating profile. A slight AsH_3 flow is maintained during the heat-up of the sample in the MOCVD chamber. This slight flow is just enough to form a monolayer of InAs

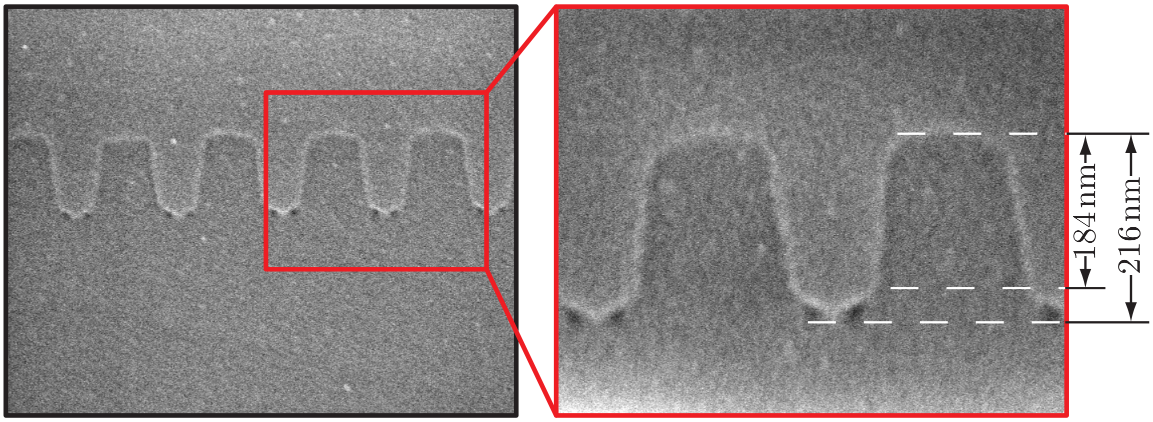

Figure 3-14: Cross-sectional SEM of the InP/InGaAsP interface after MOCVD regrowth performed at Lucent Technologies. The dark spots at the base of the grating trench are thought to be InAs inclusions resulting from the regrowth.

on the surface of the sample; this InAs layer prevents mass transport of the In that would normally erode the peaks and fill in the troughs of the grating. Because the surface temperature eventually rises above the As depletion temperature, the AsH_3 flow must be maintained in order to keep the InAs monolayer stable. When the growth temperature is finally reached, but just before growing InP, the slight AsH_3 flow is terminated, and the sample is flushed for one second with PH_3. At this point the InAs vaporizes but since the InP growth begins almost immediately, there is not enough time for the surface to mass transport before the InP buries the now preserved features[57].

After the regrown sample was received from Lucent Technologies, it was cleaved and subjected to a selective wet-etch in a mixture of DI-water:H_2O_2:H_3PO_4 with the ratio 40:5:5 for one minute. Figure 3-14 is a cross-sectional SEM of the InP/InGaAsP interface, and confirms that the profiles of the gratings are maintained during regrowth. The dark spots at the bottom corners of the trench are thought to be InAs inclusions. Typically no InAs remains unless a $\langle 111 \rangle$B face is exposed; this facet is a very fast growing plane and consequently hard to divest of As [57]. This is unlikely to be a problem, even though the refractive index of InAs is high, due to the extremely small size of the affected regions. These over growth results were repeated over two other samples, with devices gratings, with identical results.

3.3 Fabrication Process

The fabrication of the channel-dropping filter makes use of the etching techniques described above, as well as the nanolithography techniques described in chapter 1. The most important aspect of the fabrication was the development of the dual-layer hardmask process (DLHP), which incorporates the components necessary to address the fabrication issues described earlier in section 3.1. This section will describe in detail the steps of the DLHP.

3.3.1 Mask Fabrication

In constructing the channel-dropping filter, a combination of several lithographies is used. Optical-proximity lithography is used to print the relatively coarse (1.3–1.5 μm) features, and x-ray nanolithography is used to pattern the fine-period Bragg gratings. The optical photomasks which define the waveguide features were written by a commercial mask shop using a MEBES tool, and the x-ray masks used for the grating features were written with the NSL's VS2A electron-beam-lithography system.

In generating the x-ray masks required for the channel-dropping filter, we used a technique called spatial-phase-locked e-beam lithography (SPLEBL) [58, 9, 59], which marries the long-range spatial coherence of interference lithography to the flexibility of electron-beam lithography; the mode of SPLEBL employed is called the *segmented-fiducial-grid mode*. Forming the final device mask requires several precursor steps.

The IL-Grating Mask

Figure 3-15 outlines the steps used to form the IL-Grating Mask. Interference lithography is used to form a 244.4 nm pitch grating, in electroplated gold, on the x-ray mask. This grating will eventually serve as the 'fiducial' for the SPLEBL write. When printing gratings onto an x-ray mask using interference lithography, it is not possible to achieve sufficient angular alignment between the standing-wave pattern and a reference direction on the mask. This is problematic because we must know the orientation of the grating precisely. To solve this problem, after the interference lithography is done, and the gratings are plated up, we use e-beam lithography to add alignment marks to the x-ray mask which are referenced to the interferometric gratings.

After recording the interferometric grating on the x-ray mask, the grating is cleared in selected areas and replated with gold, shown in figure 3-15b. A daughter is made of this mask; this reproduction process inverses the image so that the boxes that were filled gold become open in the daughter mask, as illustrated in figure 3-15c. This mask is then placed in the e-beam lithography tool and the rotation of the grating with respect to the stage axes is measured by recording the (x, y) locations of several points along a single grating line, over a distance of approximately 1 cm. Once this calibration has been done, alignment marks—designed to overlay with those from the waveguide photomask—are written in the cleared areas. Figure 3-16 depicts how the two alignment marks, that are aligned to the grating, on the x-ray mask will serve as a lever arm when aligning to the complementary marks on the waveguide mask. By means of this technique, we guarantee that the alignment marks placed on the x-ray mask are aligned to the corresponding marks on the waveguide mask to within an angle of 10 μradians. When the x-ray mask is aligned to the waveguide level, the maximum overlay error (measured after exposure) is $\sim$500 nm, corresponding to a maximum total angular misalignment of under 50 μradians. Figure 3-15(d) depicts the completed IL-grating mask with the alignment marks.

(a)
- Interference lithography: $p = 244.4\,\mathrm{nm}$
- Develop photoresist
- Dry-etch grating (through SiO_2 interlayer and ARC)
- Electroplate gold
- Strip residual SiO_2 interlayer and ARC
- Strip and respin PMMA

(b)
- Expose large rectangular areas (by e-beam lithography)
- Develop PMMA, electroplate gold
- Strip PMMA

(c)
- Replicate onto blank x-ray mask (by x-ray lithography)
- Develop PMMA, electroplate gold
- Strip PMMA
- Spin on new PMMA

(d)
- Align e-beam coordinates to gratings lines
- Wriite alignment marks and blocking patterns
- Develop PMMA, electroplate gold
- Strip PMMA

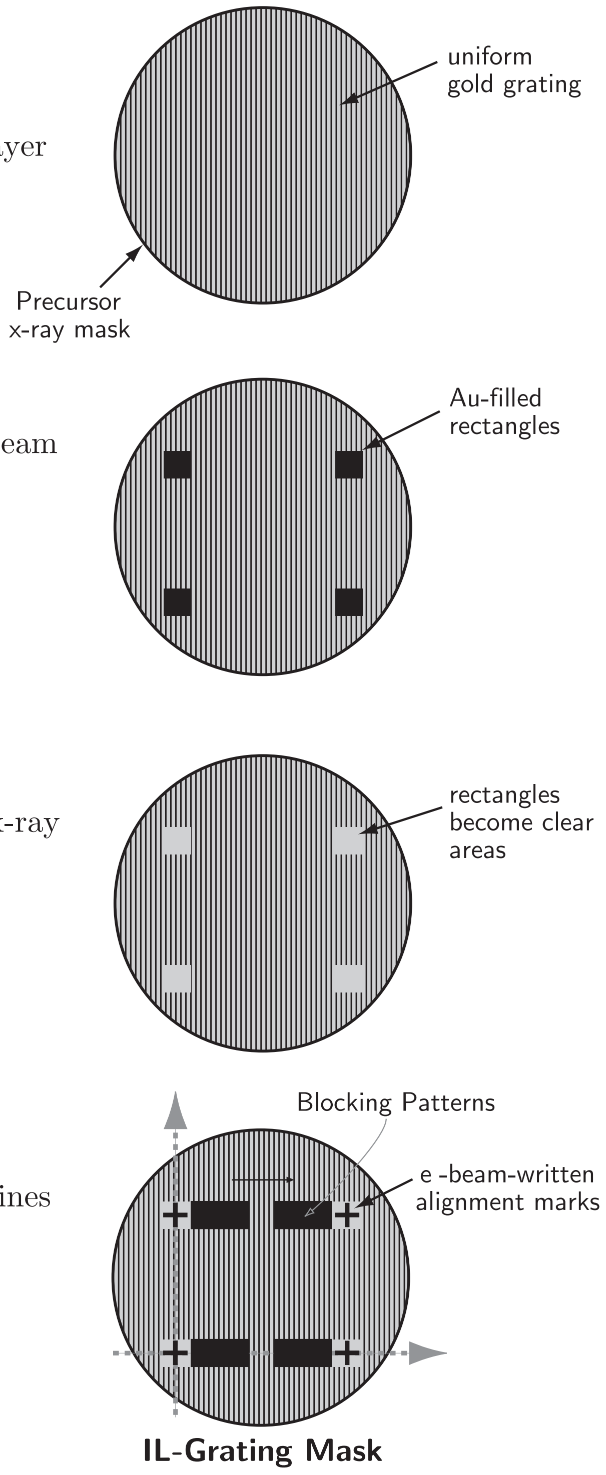

Figure 3-15: Making the interference-lithography (IL) fiducial reference mask. (a) a controlled interference lithography step forms 244.4 nm pitch gratings on the x-ray mask. (b) large areas are opened and plated in Au. (c) the mask is *daughtered* to reverse the image. (d) alignment marks, described in figure 3-16, are written in the cleared openings and blocking patterns are written.

- Write the alignment marks along grating axis. This done using the NSL's VS-2A e-beam tool.
- On the photomask, both the alignment marks and the waveguides are written with a MEBES e-beam tool.

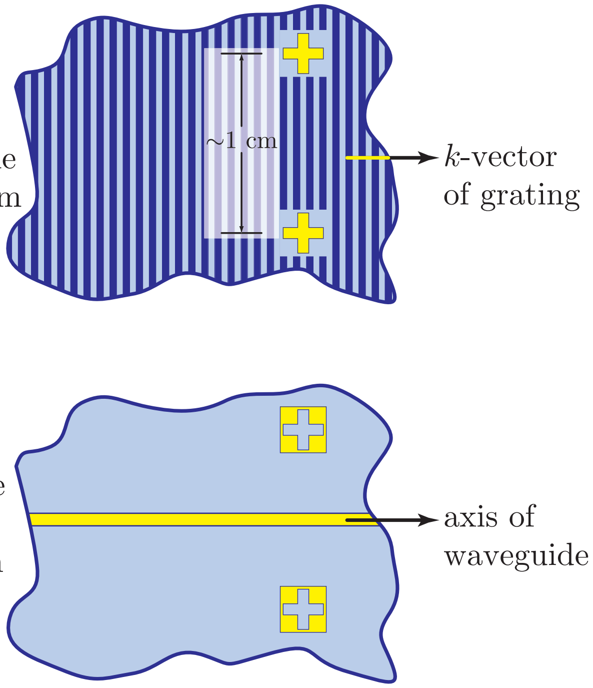

Figure 3-16: The alignment marks on the x-ray mask have a complement on the photomask that will be printed on the wafer. In addition to the typical purpose that alignment marks serve, *i.e.* lateral alignment, the marks are located far enough apart so that they can be use to angularly align the k-vector of the grating to the waveguide to better than 50 μradians.

Grating Period Control

Because of the phase locking method used to write the Bragg gratings, the period of the Bragg gratings is proportional to that of the interferometrically-generated fiducial gratings on the x-ray mask. Therefore, in order to control the period of the Bragg gratings, it is necessary to control the period of the fiducial gratings to the same relative tolerance, typically to better than one part per thousand. For simplicity of implementation, we have chosen the period of the e-beam grating to be the same as that of the fiducial, although this is not a fundamental requirement.

In interference lithography, the grating period depends upon the wavelength of exposure and the angle between the two beams that form the standing wave, according to

$$p = \frac{\lambda}{2\sin\theta} \quad ,$$

where λ is the wavelength and θ is the half-angle between the two beams. Although the wavelength is quite accurately controlled, the interference angle θ can only be adjusted to an accuracy of a few milliradians, which is a factor of 5–10 worse than needed. To overcome this difficulty, we measure the period of a test grating using the interferometer-controlled stage of our electron-beam lithography system, and we then fine tune the interference lithography setup to eliminate any period errors. After the test grating is recorded by interference lithography onto a silicon wafer, the sample is electroplated with gold to provide contrast for backscattered electron imaging in the e-beam system. The wafer is mounted on the e-beam stage and the direction of the grating lines with respect to the stage's axes of translation is measured, to eliminate cosine errors. We measure the distance across a large number of periods (250–500) by translating the stage. This distance divided by the number of periods gives the grating period. Figure 3-17 is a histogram illustrating the high precision achieved with this technique. Using this procedure the actual period of the gratings was found to be within 0.1 nm of the design specification (244.4 nm). This gold grating on the Si wafer serves as a reference standard which we use to set up the interference lithography, ensuring that the fiducial grating that we next expose on the x-ray mask has an accurately known period.

SPLEBL-Grating Mask

The segmented-grating mode of SPLEBL requires isolated fiducial gratings in order to write the actual device gratings. Figure 3-18 outlines the procedure to prepare the IL-grating mask for SPLEBL. First one places a prepattern of PMMA, that corresponds to the desired locations of the fiducials, on an x-ray mask; these large features are printed using deep-UV optical-proximity lithography. This PMMA prepattern also contains alignment marks, which are used when one makes an aligned daughter exposure with the IL-Grating Mask. After developing and plating this mask, now referred to as the Fiducial-Master Mask, one makes a daughter in order to reverse the polarity. After this mask is electroplated with gold, new PMMA is spun on. This *Fiducial-Grating Mask* contains gold IL gratings in isolated regions, and large open areas of PMMA

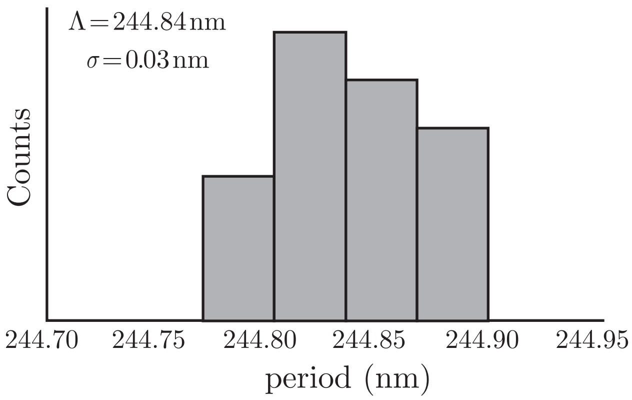

Figure 3-17: Histogram demonstrating the precision with which we can measure the period of an interferometrically-generated grating. The histogram was obtained by repeatedly measuring the period of the same grating. The accuracy of the measurement is limited by the wavelength of the laser, which is known to 1 part in 10^8, and the cosine error due to misalignment of the stage's interferometer optics and its axes of motion, which we estimate to be less than 1 part in 10^6.

for the SPLEBL write. Finally e-beam lithography is used to write the quarter-wave-shifted patterns required by the device. During the e-beam writing, the existing interferometric pattern on the mask is sampled in order to determine the absolute beam position. This sampling is the basic SPLEBL step, and allows one to generate quarter-wave-shifted gratings that span several e-beam writing fields, yet are free of the inter-field stitching errors that would otherwise be present [9]. A more detailed description of the fabrication of the IL and SPLEBL-grating masks can be found in reference [12].

Final Device Mask

The SPLEBL-grating mask has fiducial gratings that we do not want transferred onto our final substrate. To remove these extraneous patterns we first daughter the SPLEBL-grating mask and then respin it with PMMA. Figure 3-19a shows an SEM of the daughtered SPLEBL-grating mask. The continuous fiducial gratings located above and below the quarter-wave shifted device gratings must be removed in order to use this mask.

Onto this mask we align and daughter the *fiducial-clearing mask*. After this exposure, PMMA will cover all the SPLEBL-written patterns, as well as alignment marks, and leave the fiducial gratings exposed. Therefore, electroplating gold will bury the fiducials. A daughter of this mask contains only the alignment marks and the device gratings. This final mask is the *device-grating mask*. This process is depicted in figure 3-20.

(a)
- Prepattern PMMA on blank mask with deep-UV optical-proximity lithography
- Develop PMMA

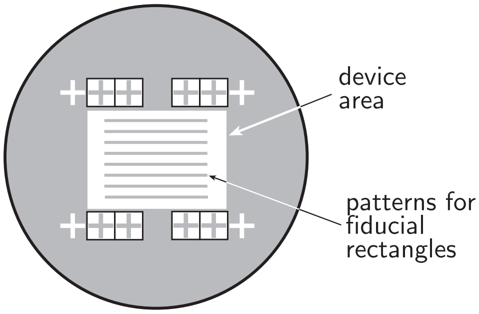

(b)
- Align IL-Grating Mask to prepattern
- Expose grating by x-ray lithography
- Develop PMMA, electroplate gold
- Strip PMMA

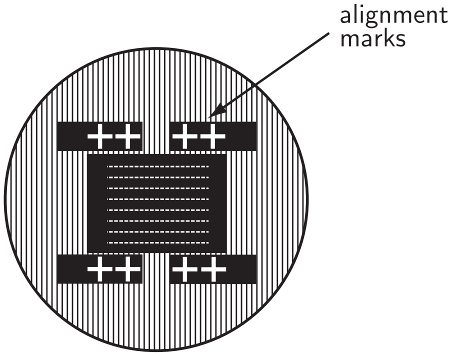

Fiducial-Master Mask

(c)
- Daughter onto blank x-ray mask to reverse polarity
- Develop PMMA, electroplate gold
- Strip PMMA
- Spin on new PMMA

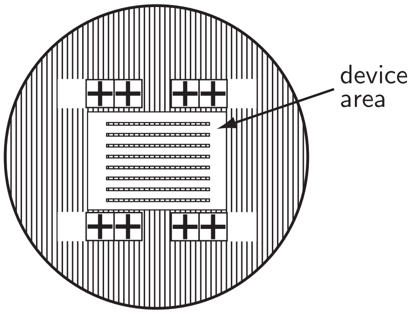

Fiducial-Grating Mask

(d)
- Write device gratings using SPLEBL
- Develop PMMA, electroplate gold
- Strip PMMA

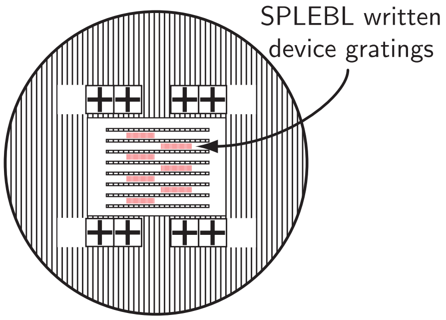

SPLEBL Grating Mask

Figure 3-18: Making the SPLEBL-grating mask. (a) PMMA is prepatterned with alignment marks and blocks; the blocks correspond to the desired locations of the fiducial gratings. (b) the IL-Grating Mask is aligned and daughtered onto the mask, and then electroplated in Au. (c) The Fiducial-Master Mask is daughtered to reverse the polarity. (d) The quarter-wave shifted gratings are written.

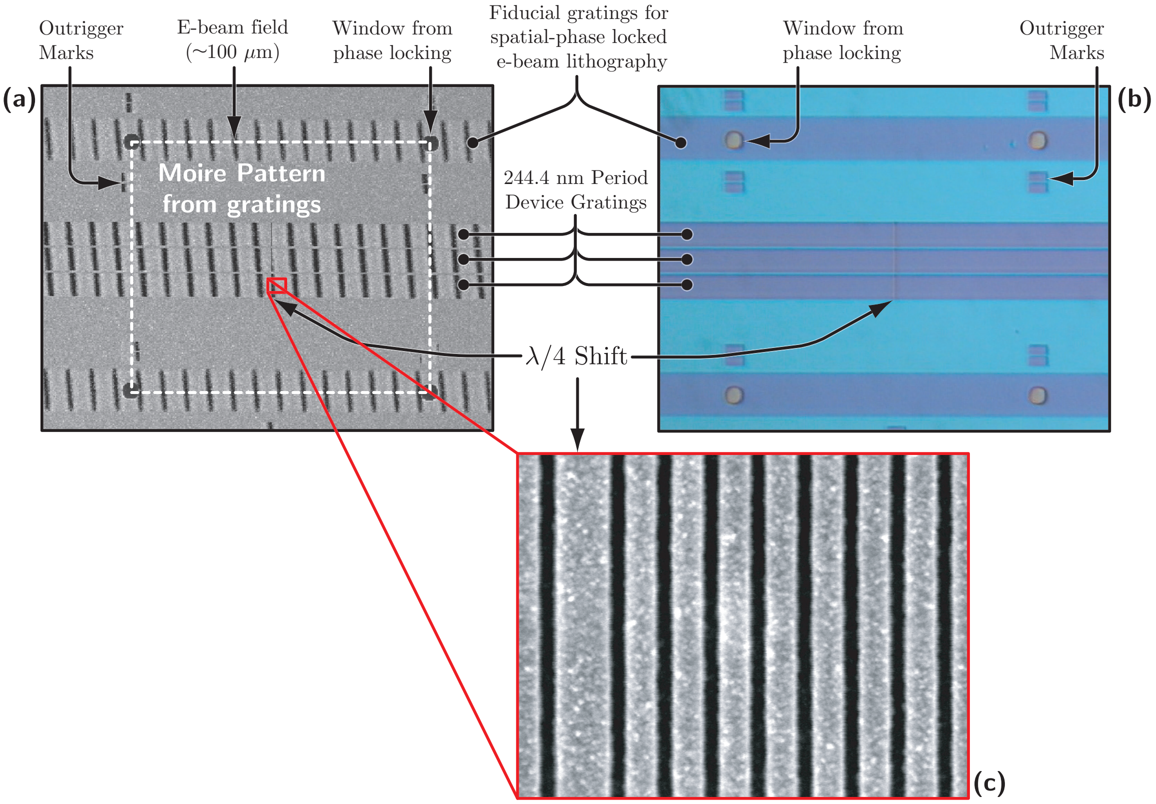

Figure 3-19: Daughter of the SPLEBL-grating mask and a test print in PMMA. (a) This scanning electron micrograph illustrates that the x-ray mask contains many extraneous features, required for the SPLEBL write, that must be removed. (b) This optical micrograph illustrates a print into PMMA demonstrates the fidelity of x-ray lithography, and the necessity of removing the extraneous features. (c) A high-magnification SEM of the x-ray mask clearly indicates the quarter-wave shift in the device gratings.

(a)

- Splebl gratings mask has fiducial gratings that must be removed
- Daughter splebl grating mask by x-ray lithography
- Develop pmma, electroplate gold
- Strip and respin pmma

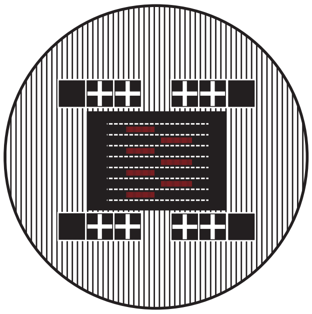

Daughter of SPLEBL Grating Mask

(b)

- Align fiducial clearing mask to daughter of splebl grating mask and expose
- Develop pmma
- Exposure results in pmma covering the device gratings and alignment marks
- Electroplate gold
- Strip pmma

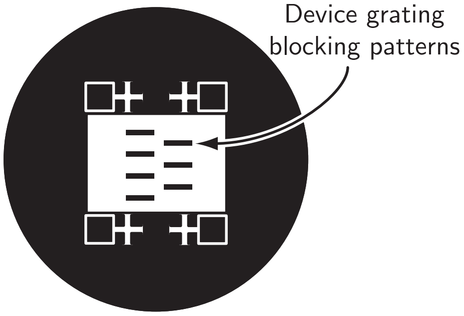

Fiducial Clearing Mask

(c)

- Daughter onto blank x-ray mask
- Develop pmma, electroplate gold
- Strip pmma

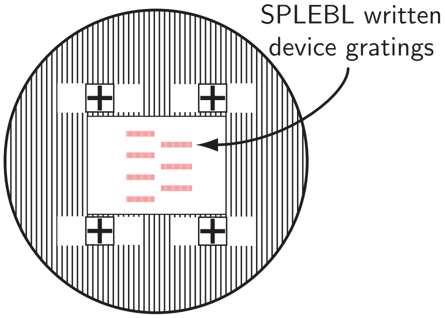

Final Device Mask

Figure 3-20: Making the final device-grating mask requires clearing the fiducials patterns. (a) The splebl-grating mask is daughtered to reverse the polarity and respun with pmma. (b) A fiducial-clearing mask is aligned and exposed onto the mask from (a); after development, pmma covers the device gratings and certain alignment marks. (c) The mask is electroplated and daughtered to produce the final device-grating mask.

3.3.2 Dual-Layer Hardmask Process

After the masks are generated, there remains the problem of forming sub-micron grating patterns over relatively tall surface topography. To address this problem, we have developed a technique that we call the Dual-Layer-Hardmask Process (DLHP), which is outlined in figure 3-21. In this process, the Bragg grating patterns are defined first in a thin hard-mask layer on the substrate (figure 3-21a). Before the gratings are etched, however, the waveguide features are patterned in a second hard-mask on top of the grating hard-mask (figure 3-21b). By patterning both hard-masks before the waveguide or grating features are etched into the optical substrate, we ensure that all lithography steps are performed over essentially planar surfaces.

The process begins with an optical substrate of InP with a 1.1 μm-thick layer of InGaAsP quaternary core; this material was grown by MOCVD at Lucent Technologies. Onto the substrate, we spin on a 300 nm-thick layer of PMMA and expose it in our x-ray lithography system using the device-grating mask described earlier. We develop the PMMA in a mixture of MIBK:IPA:MEK 21:63:16. After development, we lift off 50 nm of titanium using hot-NMP to dissolve the PMMA. The hot-NMP is followed by acetone, methanol, DI-water rinse. Having patterned the grating hard-mask, the PMMA is removed.

Next, we spin and bake on a thin layer of PMMA, $\leq$ 50 nm. Then we spin on a layer of OHKA TMHRi negative-tone photoresist, and expose the waveguide patterns using optical contact photolithography. In this step, we reference to the alignment marks left by the grating mask to ensure angular alignment between the waveguide and Bragg-grating axes. After a 100°C post-exposure bake and development, in OPD-262, we lift off the waveguide pattern in 200 nm of nickel. The thin PMMA layer is required because the OHKA photoresist is difficult to remove. Figure 3-22a is a scanning-electron micrograph depicting the patterned nickel hard-mask layer, with the underlying grating in titanium. We then use the nickel waveguide layer as an etch mask to clear away any residual grating mask, using a CHF_3 RIE process, as shown in figure 3-22b. This grating-removal step insures that the grating will be perfectly aligned to the waveguide. Figures 3-23a and 3-23b show examples of where the waveguide and grating are not perfectly aligned. Figure 3-23c shows how after the excess grating is removed, both result in perfect alignment.

The waveguide features are then etched into the InGaAsP core material, using the nickel layer as hard-mask. The InGaAsP is reactive-ion-etched in a hydrocarbon plasma of $O_2/H_2/CH_4$ at flow rates of 2.5/19/19 sccm. We maintain a DC bias of 300 V and chamber pressure of 5 mT. This etch results in straight sidewalls and smooth etch surfaces, as described in section 3.2.2 and shown in figure 3-24a. Next, the nickel is removed with a selective wet chemical etch, revealing the underlying titanium grating pattern. Figure 3-25 shows one of the complication in removing nickel: there is some residue that remains. This residue can be easily removed in a 200 VDC O_2 RIE step. Once the surface is cleaned of the residue, the Bragg gratings are etched into the top surface of the waveguide using the titanium as the hard-mask. Finally, the titanium layer is stripped using a solution of buffered HF, completing the process. Figure 3-26 depicts the completed structure after this etch sequence.

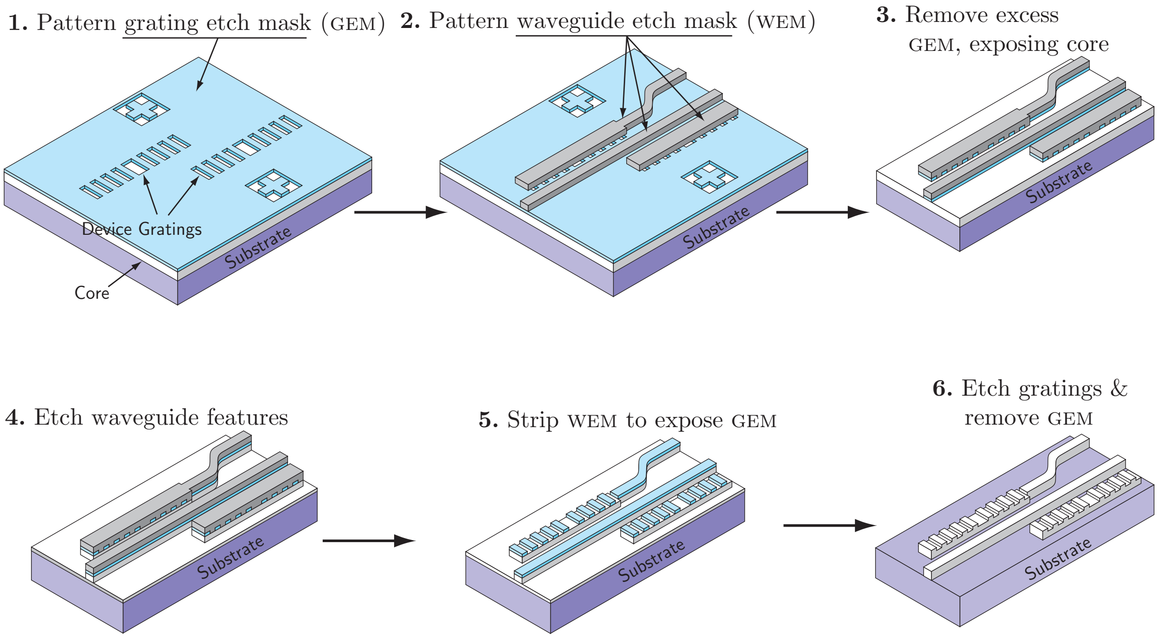

Figure 3-21: The dual-layer hardmask process (DLHP) integrates MITs unique lithography capabilities with an innovative process sequence that enables one to perform all required lithography steps prior to etching. (1) The device grating etch mask (GHM) is defined through x-ray nanolithography. The x-ray mask, made using a combination of MIT's interferometric and spatially phase-locked e-beam lithography technologies, contains two alignment marks that act as a long lever arm to ensure angular alignment of the grating to the waveguide. (2) The waveguide etch mask (WHM) is defined through optical-contact lithography. Note that the device grating is wider than the width of the waveguide which ensures that the lateral alignment of the grating to the waveguide is perfect. (3) The excess GHM is removed through reactive-ion etching. (4) The waveguide is etched into the optical substrate. (5) The WHM is stripped revealing the GHM perfectly aligned atop the waveguide. (6) The grating is etched and the GHM removed. The structure is now ready for overgrowth.

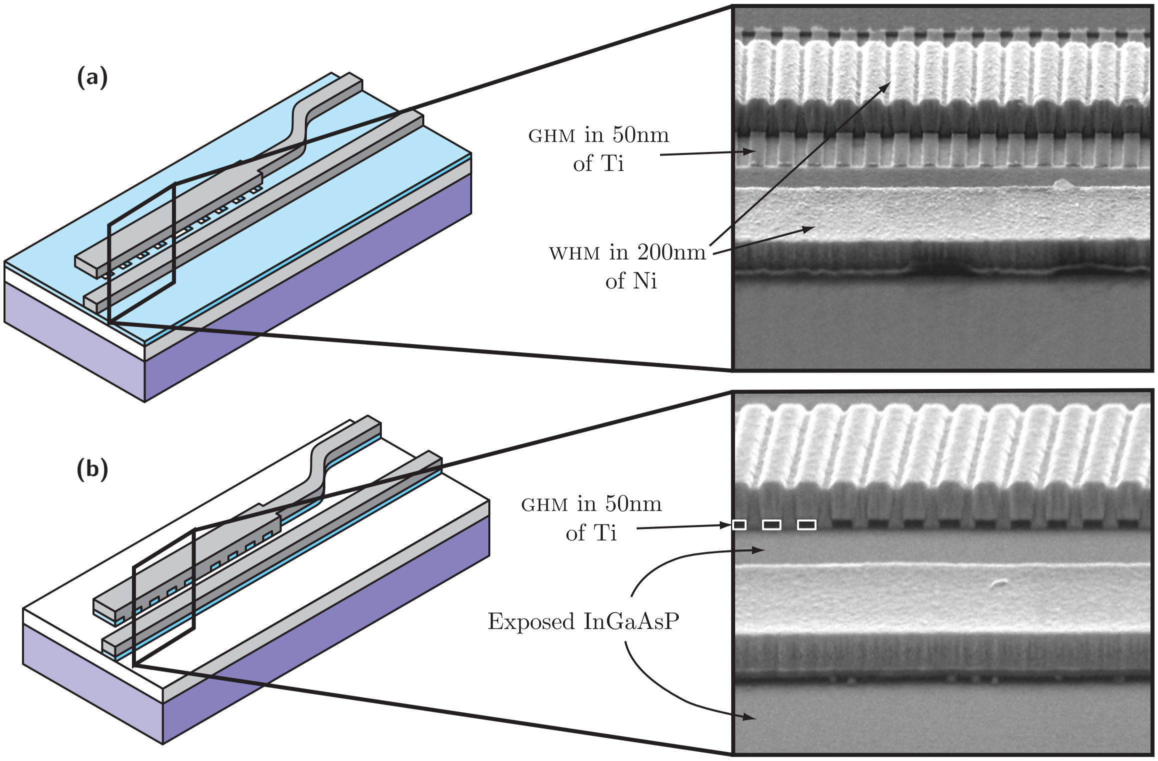

Figure 3-22: (a) Scanning electron micrograph showing both the *grating hard-mask*(GHM) and the *waveguide hard-mask*(WHM) used in the process. The waveguide features are patterned with optical photolithography and Ni liftoff, and the underlying gratings are patterned in Ti via x-ray nanolithography and reactive-ion etching. (b) After patterning both hard-masks, the excess grating patterns are removed using the waveguide pattern as a mask.

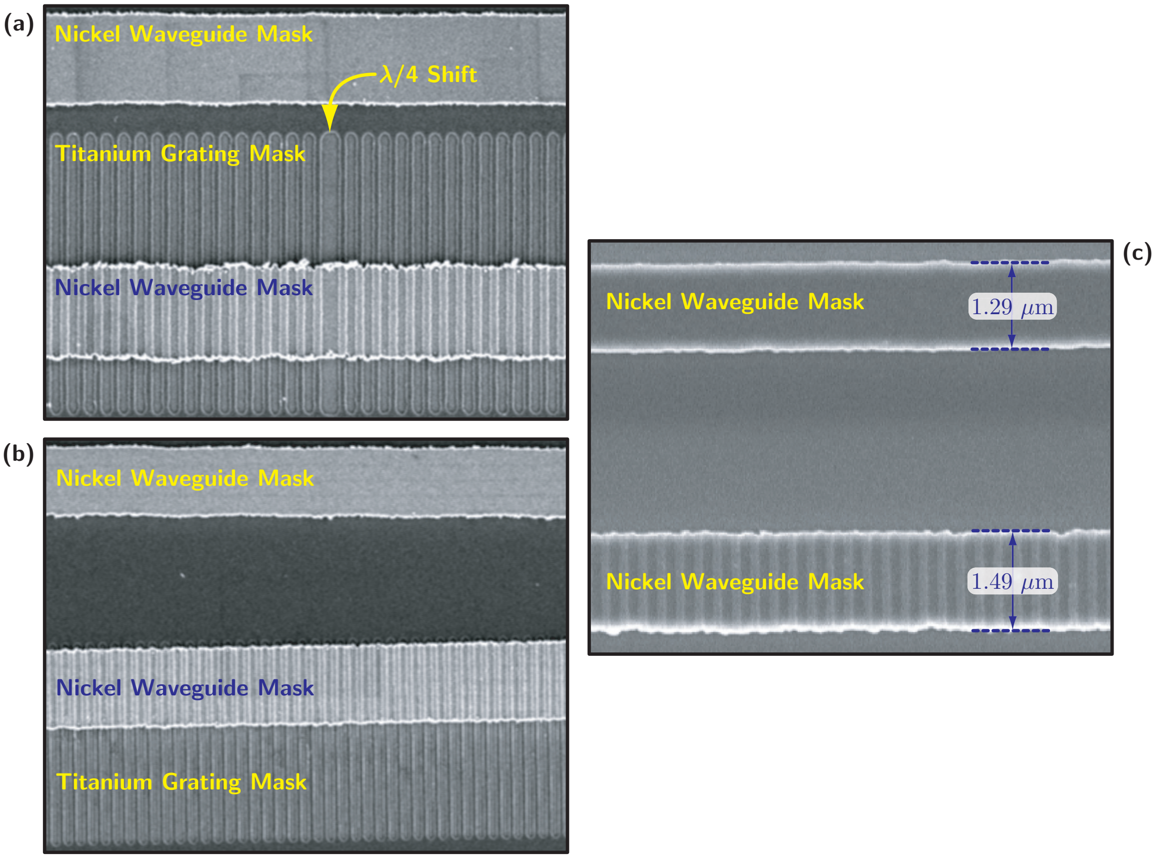

Figure 3-23: A top-view of the etch masks demonstrates the self-aligned nature of the DLHP process and the large tolerance in lateral alignment. (a) and (b) differ in lateral alignment by approximately 1 μm. Both (a) and (b) look like (c) after the excess grating is removed. That is, the grating is perfectly aligned to the waveguide. The resulting etch mask has a width of 1.29 μm for the bus-waveguide and 1.49 μm for the grating.

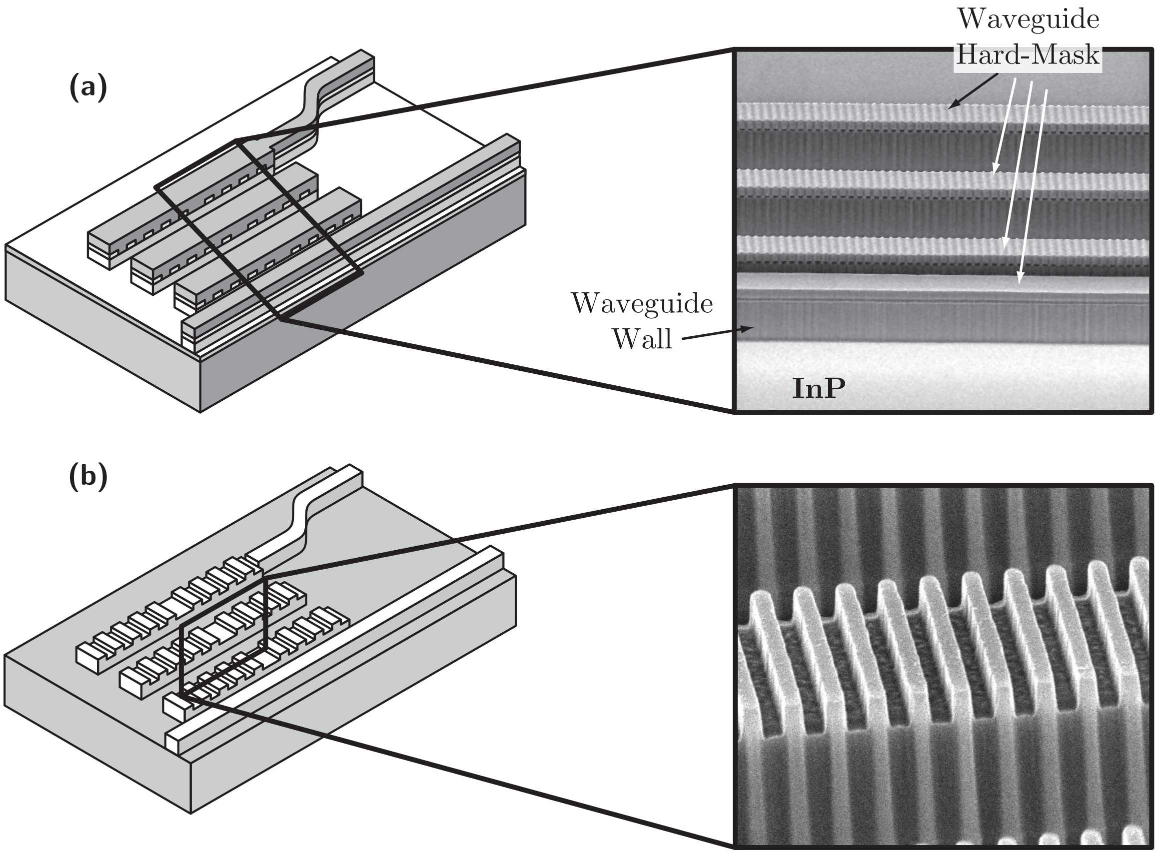

Figure 3-24: Scanning electron micrographs showing (a) the etched waveguides; (b) final structure after etching of the gratings and removal of hard-masks. (The three parallel gratings shown here are portions of a higher-order filter.)

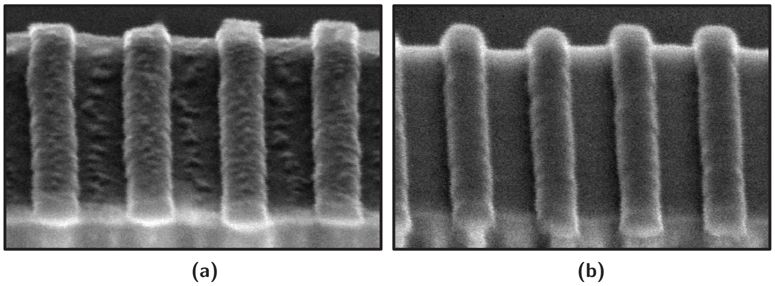

Figure 3-25: The nickel wet etchant leaves behind some residue. (a) shows the Ti grating lines sitting on top of the etched waveguide immediately after the Ni wet-etch. (b) shows that the scum-like residual material can be removed through an O_2 RIE step. Sputtering is an important component of the removal; an unbiased O_2 plasma will not remove the substance

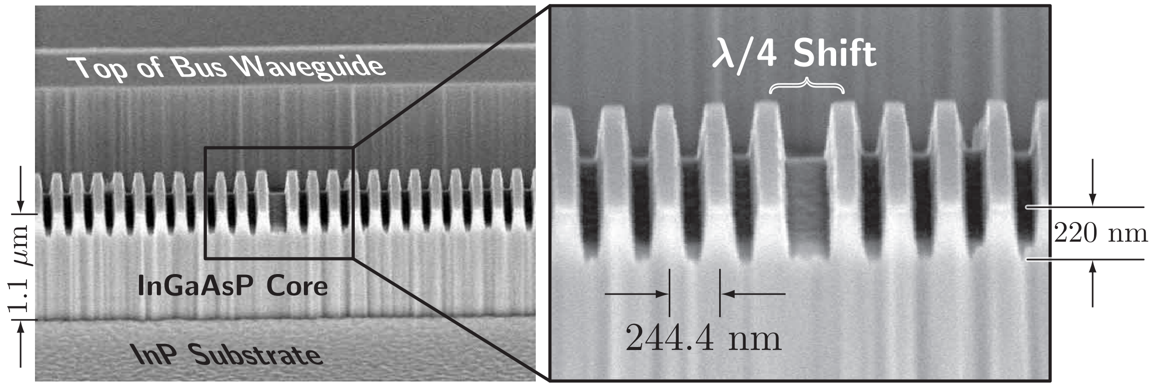

Figure 3-26: The completed structure shows a quarter-wave shifted Bragg grating. To complete the device, this structure is overgrown with InP in an MOCVD system. The resulting grating has a duty-cycle of approximately 52%.

The final step in the process is to overgrow a top layer of InP cladding material, thereby forming a buried-channel waveguide structure. This regrowth was performed by Charles Joyner of Lucent Technologies and described in section 3.2.2.

3.4 Summary

This chapter has discussed the challenges and solutions to some of the major problems in economically manufacturing integrated-optical devices. Specifically the nanolithography technologies of the NSL were integrated into the DLHP process to produce quarter-wave shifted Bragg grating on top of waveguides. The process is robust and can easily be applied to other material systems and other grating geometries.

As a test of the quality of the gratings Jalal Khan measured the optical response of several in-line resonators. The measurements indicated that the gratings were of extremely high quality and very low-loss [60].

Chapter 4

Conclusions and Future Work

This final chapter attempts to serve two purposes. First, it will attempt to draw together the two previous chapters by using some simple analysis to show the effects of x-ray mask distortion on the spectral response of Bragg-grating based microphotonics. Second, it will highlight some work that has not quite reached maturity. Additionally, it will try to point out some new directions that this research might take.

4.1 XRM Distortion & Spectral Response

Semiconductor devices are constructed in layers; each layer requires lithography that must be accurately and precisely aligned to all the other layers. X-ray mask distortion detrimentally affects the ability of one to accurately overlay these different layers of lithography. It is not the distortion itself that is the culprit—optical projection systems have systematic distortion in the field—but rather the pattern dependent nature of the distortion. When gate lengths are on the order of 100 nm, the overlay budget is approximately 10 nm. As long as the distortion is either small enough or systematic enough, *i.e.* all layers are identically distorted, then all the features will overlay and the failure of any semiconductor devices can be attributed to other causes. It is important to note that distortion only has an indirect effect of the performance of semiconductor devices.

In contrast, distortion has a direct effect on the performance of Bragg-grating-based integrated-optical devices. Bragg-grating devices rely on the fidelity of their gratings to perform their functions. Any distortion in the grating, *e.g.* chirp, can seriously affect the spectral response of the grating. Murphy describes how the chirp in the interferometric lithography system affected the spectral response of simple Bragg reflectors [37]. Any mask distortion is directly translated to grating distortion.

Integrated-optical devices have overlay requirements as well, but they are considerably easier to meet than those of semiconductor devices. Current waveguides range from 1–5 μm in width, depending on the material system used. As shown in figure 3-23, the dual-layer hardmask process enables one to tolerate $\sim 1\mu$m-scale lateral misalignments.

This section describes the effects of distortion on the spectral response of Bragg-

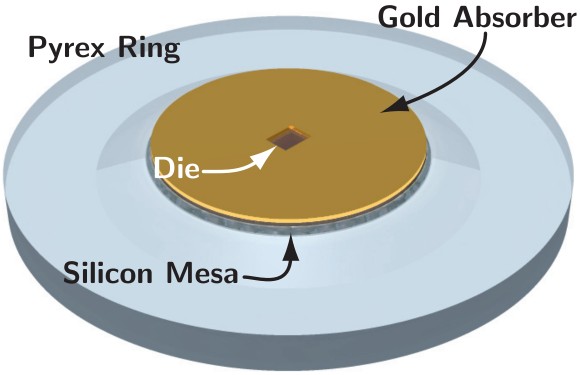

Figure 4-1: The typical x-ray mask contains an open central region, called a *die*, with a large periphery of absorber. In our case the absorber is a thin foil of gold. The pyrex ring is for support and ease of handling. As noted previously, the silicon mesa is for ease of exposure and exposure-gap control.

grating-based integrated-optical devices.

4.1.1 X-ray Mask Distortion

Figure 4-1 depicts a typical mask pattern with a central region, called a *die*, containing the patterns of interest and a large periphery that is either blank or completely covered with absorber. In-plane distortion is highest when this periphery is completely covered with absorber. In the specific case of the CDF mask, the die is a 5 mm × 9.4 mm region that contains the device grating features in the center of the membrane. The grating patterns on the CDF mask are placed as densely as practically possible. Even in this case, the device gratings make up a very small fraction of the die area (much less than 2% of the die area). We can effectively view the die as a completely open region since the small amount of absorber will contribute trivially to the overall distortion.

Chapter 2 described the problem x-ray mask distortion caused by the absorber. We model the distortion caused by the absorber using the minimum energy technique described in Appendix A. Figure 4-2a illustrates the shape of the distortion caused by the tensile stress of the CDF mask pattern.

4.1.2 Modeling Distortion Effects

There are a number of techniques one might use to calculate the effects of x-ray mask distortion on the spectral properties of Bragg-grating-based filters. For example, Thomas Murphy used a coupled-mode technique to model the effects of period chirp, introduced by interferometric lithography, in the grating [37]. Because the magnitude and direction of x-ray mask distortion is arbitrary, the author decided to use a transfer-matrix technique because of the relative ease and flexibility of the calculations[1]. Figure 4-3 illustrates how a grating structure can be modeled as a di-

---

[1] The mechanics of the transfer matrix approach is well explained in reference [61].

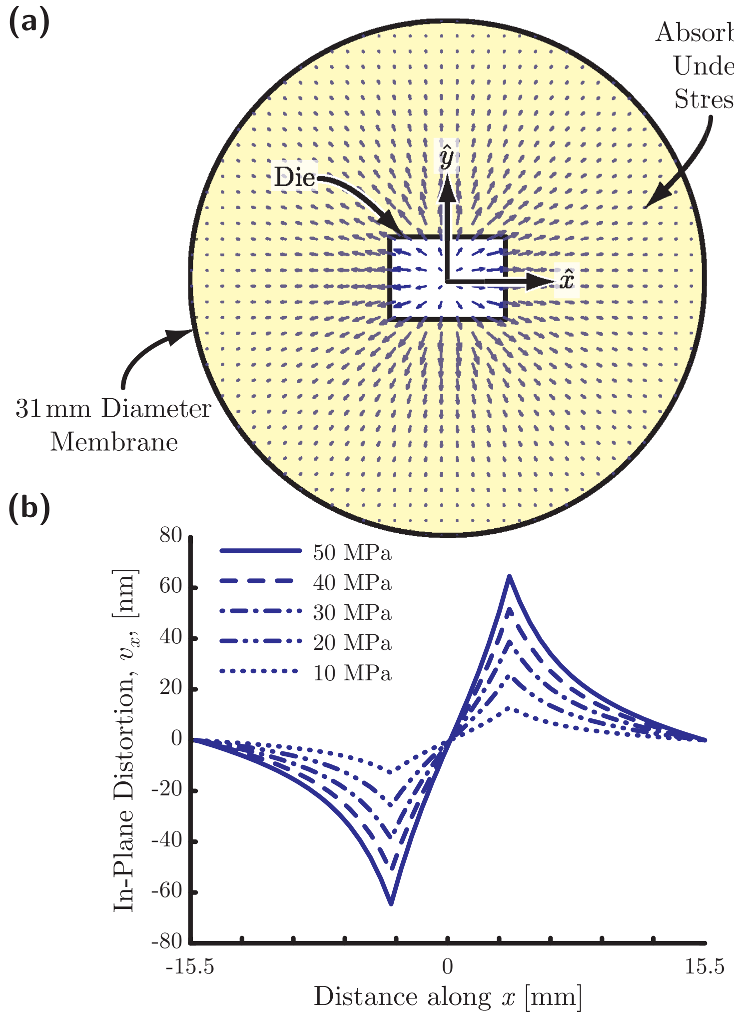

Figure 4-2: Distortion resulting from CDF die pattern. (a) shows the overall pattern of the in-plane distortion. The tensile absorber tends to pull everything tighter, which can be seen most easily in the edges of the die region moving out. (b) shows the in-plane distortion, v_x, along the mid-line of the membrane for different for differing values of absorber stress. As one would expect the IPD increases along with the stress level.

electric stack. The two constituents of the grating, *i.e.* the tooth and trench, are first analyzed independently, using a mode solver to calculate the propagation constant and effective index of each cross-section. The grating is then modelled a dielectric stack with the alternating indices n_{tooth} and n_{trench}.

Reference [62] describes how this approach can be related to the coupled-wave approach. The coupling constant, κ, can be related to the indices of the dielectric stack through the relation:

$$-\kappa\Lambda \simeq \frac{2\,\Delta n}{n} \tag{4.1}$$

where

$$\Delta n = \frac{n_{\text{tooth}} - n_{\text{trench}}}{2} \quad ,$$

$$n = \frac{n_{\text{tooth}} + n_{\text{trench}}}{2} \quad ,$$

and Λ is the Bragg grating period of the grating. Coupled-mode theory and the transfer matrix techniques should produce spectral results that are identical. In order to test the transfer matrix technique in a nontrivial case the author modeled the chirp of the SOI grating in reference [37]. Specifically, the chirp of the grating was

$$\Lambda(x) = \Lambda_0 + 56\left[\frac{\text{pm}}{\text{cm}}\right] x \quad , \tag{4.2}$$

where Λ_0 is the unperturbed period of the grating. We can relate this to the IPD through the relation:

$$v_x = -\frac{A}{2\,\Lambda_0} x^2 \quad , \tag{4.3}$$

where v_x is the IPD distortion along the x direction, and A is the chirp (which is 56[pm/cm] in the above case). Using equation 4.3 we can write that the grating is altered by the distortion:

$$v_x = 1.25 \times 10^{-8}\left[\frac{1}{\mu\text{m}}\right] x^2 \quad . \tag{4.4}$$

This distortion, v_x, is directly entered into the transfer matrix calculation to simulate the chirp of the interferometrically generated grating from reference [37]. Specifically the grating is 8 mm long, with a 223 nm-period grating formed in a silicon-on-insulator (SOI) material system. Figure 4-4 shows the result of the calculation; the transmitted power spectrum is identical to the spectrum calculated by the coupled-mode theory analysis in reference [37].

4.1.3 Spectral Effects of Distortion

As stated above, the major contributor to the distortion is the large area of absorber outside the die. Figure 4-2b shows how 50 MPa of tensile stress moves the edges of the

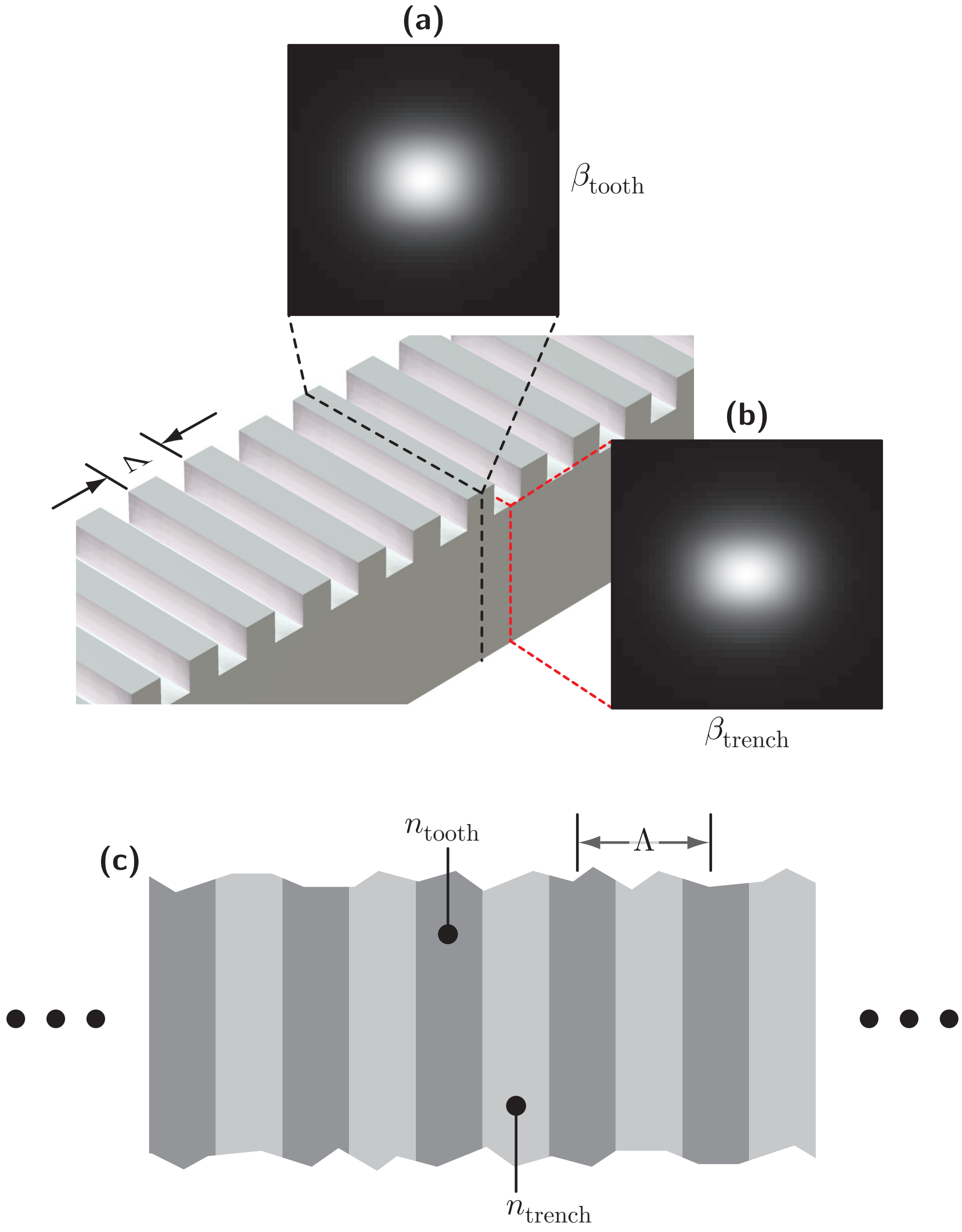

Figure 4-3: A grating structure can be analyzed as an alternating dielectric stack by viewing the grating tooth and trench as the two alternating layers. (a) shows an example of the tooth's mode profile, with propagation constant β_{tooth}. (b) shows the same for the trench region, with propagation constant β_{trench}. It takes a sharp eye to see that the trench mode profile is a little flatter than the tooth's profile. (c) shows how the dielectric stack would conceptualized. The index for the tooth, $n_{\text{tooth}} = (\lambda/2\pi)\beta_{\text{tooth}}$, and trench, $n_{\text{trench}} = (\lambda/2\pi)\beta_{\text{trench}}$, are used as the values for the layers in the dielectric stack.

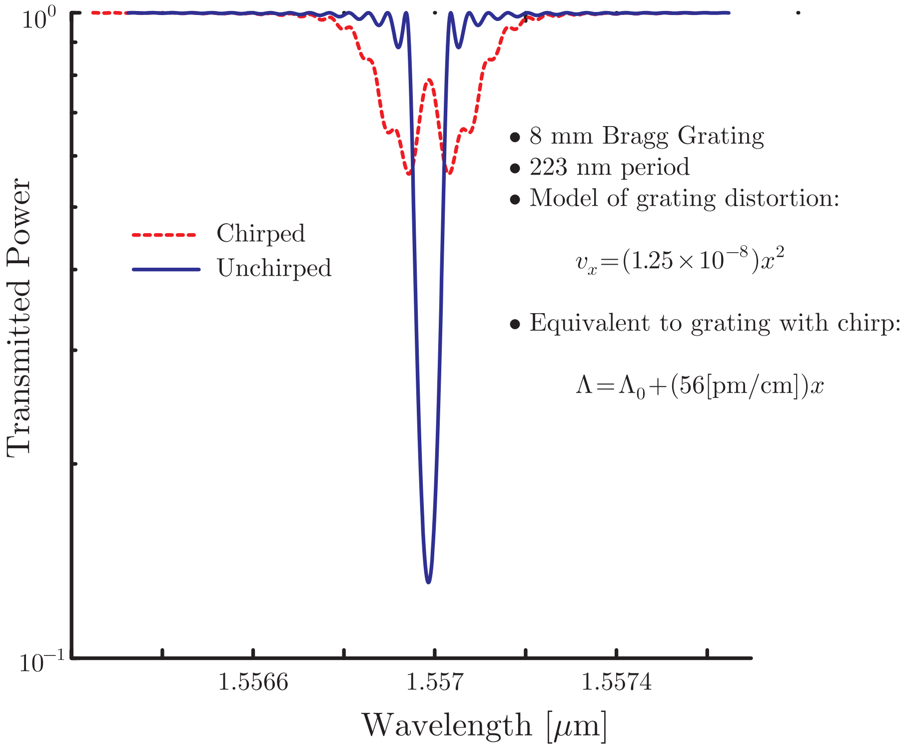

Figure 4-4: The transfer matrix technique is used to simulate the chirp of the interferometrically generated grating from reference [37]. Specifically the grating is 8 mm long, with a 223 nm-period grating formed in a silicon-on-insulator (SOI) material system. The transfer matrix technique modeled the IPD, v_x, of the grating which was equivalent to a chirp of 56 pm/cm. The transmitted power spectrum is identical to the spectrum calculated by the coupled-mode theory analysis in reference [37].

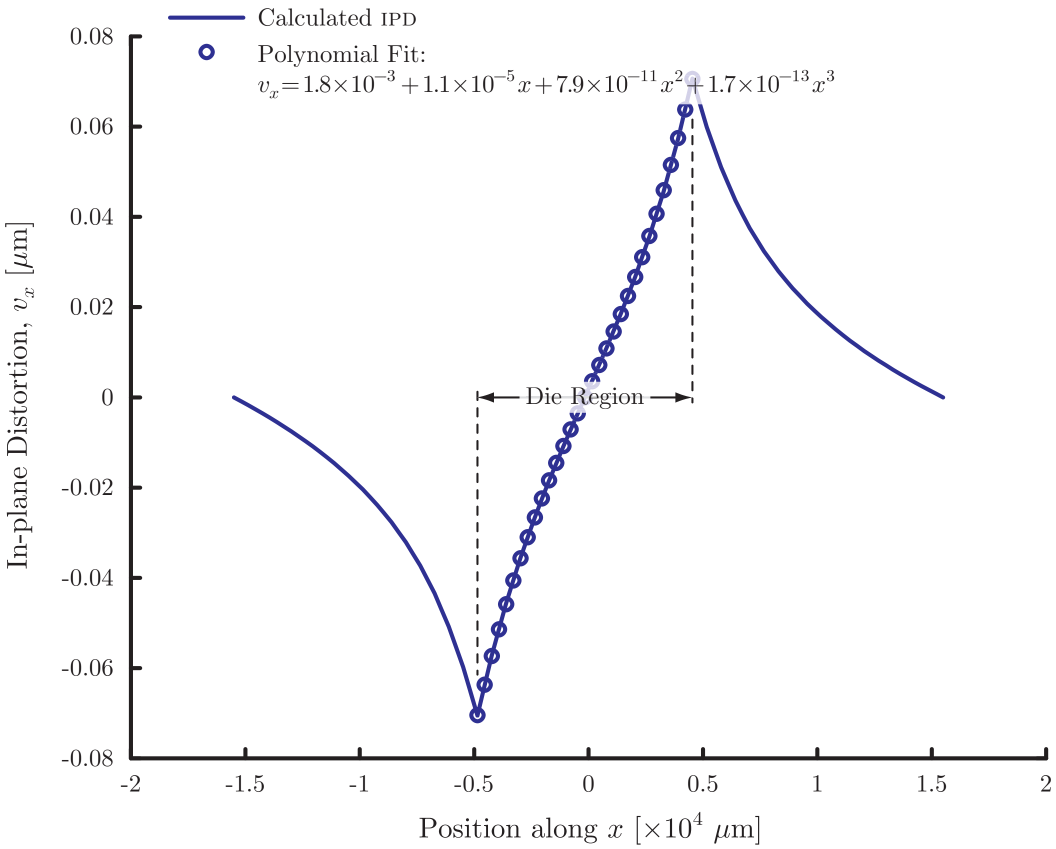

Figure 4-5: In order to model the spectral effects of the distortion caused by x-ray mask distortion, we first model the effects of the tensile absorber paying particular attention to the die region. The solid line shows the IPD along the mid-line of the membrane for the case of 50 MPa of absorber stress. The circles show the result of the 3rd-order polynomial fit that results in equation 4.5.

die away from the center by approximately 70 nm; the movement is commensurate with lower stress levels. We perform the analysis for the 50 MPa case, though this stress level is higher than what would be realistic; we can consider this a worst-case scenario.

Modeling In-Plane Distortion

Figure 4-5 shows the distortion along the mid-line of the x-ray mask; this is where the distortion is the most pronounced. In order to put this in a form that the transfer matrix technique can digest, a 3rd-order polynomial is fit to the calculation result in the die region of the mask. The result, is also plotted in figure 4-5,

$$\begin{aligned} v_x = 1.814\times10^{-3} &+ 1.136\times10^{-5}\,x \\ &+ 7.923\times10^{-11}\,x^2 \\ &+ 1.657\times10^{-13}\,x^3 \quad , \end{aligned} \tag{4.5}$$

is a good fit to the distortion. The dominant functional term is linear, indicating that one would expect the primary effect of the x-ray mask distortion to be an expansion in the grating period. An increased grating period would cause the spectrum to shift to longer wavelengths. The higher-order distortion terms, which are considerably smaller, contribute to the chirp and would have more dramatic effects on the spectral response of the grating.

Quarter-Wave Shifted Gratings

Figure 4-6 shows the result of using equation 4.5 in the transfer-matrix technique to model a quarter-wave-shifted grating with parameters very similar to those of the CDF devices described earlier. Specifically, the grating is located at the center of the die and is 600 μm long. A mode solver gives the effective indices of the tooth and trench to be 3.1881 and 3.1835 respectively. Equation 4.1 states that such an alternating dielectric stack has a κ of 58 cm^{-1}; this is very close to the κ value that was experimentally observed [60]. Clearly, this type of distortion alters the spectral response of strong gratings very little. Specifically, the spectrum has red-shifted by 0.002 nm and the peak reflectivity, in the resonance peak, has dropped by 0.18%. This behavior is consistent with the fact that the dominant term of the x-ray mask distortion is the expansion of the grating period.

Comparison to Measured Distributed Bragg Gratings

We can also use equation 4.5 to model how the distortion might affect the spectrum of the one of the distributed Bragg reflectors (DBR) that was fabricated. Figure 4-7 shows the measured spectral response of the DBR overlaid with the transfer-matrix calculation. Additionally, the dotted line shows the spectral effect of the IPD from the x-ray mask. The distortion of the x-ray mask

Spectral Response of Flip-Bonded X-ray Mask

We can return to one of the flip-bonded x-ray mask discussed in section 2.3.1, specifically MITa599. A significant amount of distortion due to the flip-bonding process was measured. This distortion made the idea of an uncorrected prepatterned flip-bonded x-ray mask unusable for high-performance semiconductor devices. If we were to place a hypothetical quarter-wave shifted grating onto the mask prior to flip-bonding we could use our techniques to calculate the spectral effects of the distortion. Figure 4-8a shows the polynomial fit to the IPD due to the flip-bonding process. Figure 4-8b shows a comparison of the spectra for an undistorted QWS grating and the distorted QWS grating (in the dotted line). The significant contraction of the grating period, which causes a noticeable blue-shift in the spectrum, is the dominant effect of the flip-bonding distortion.

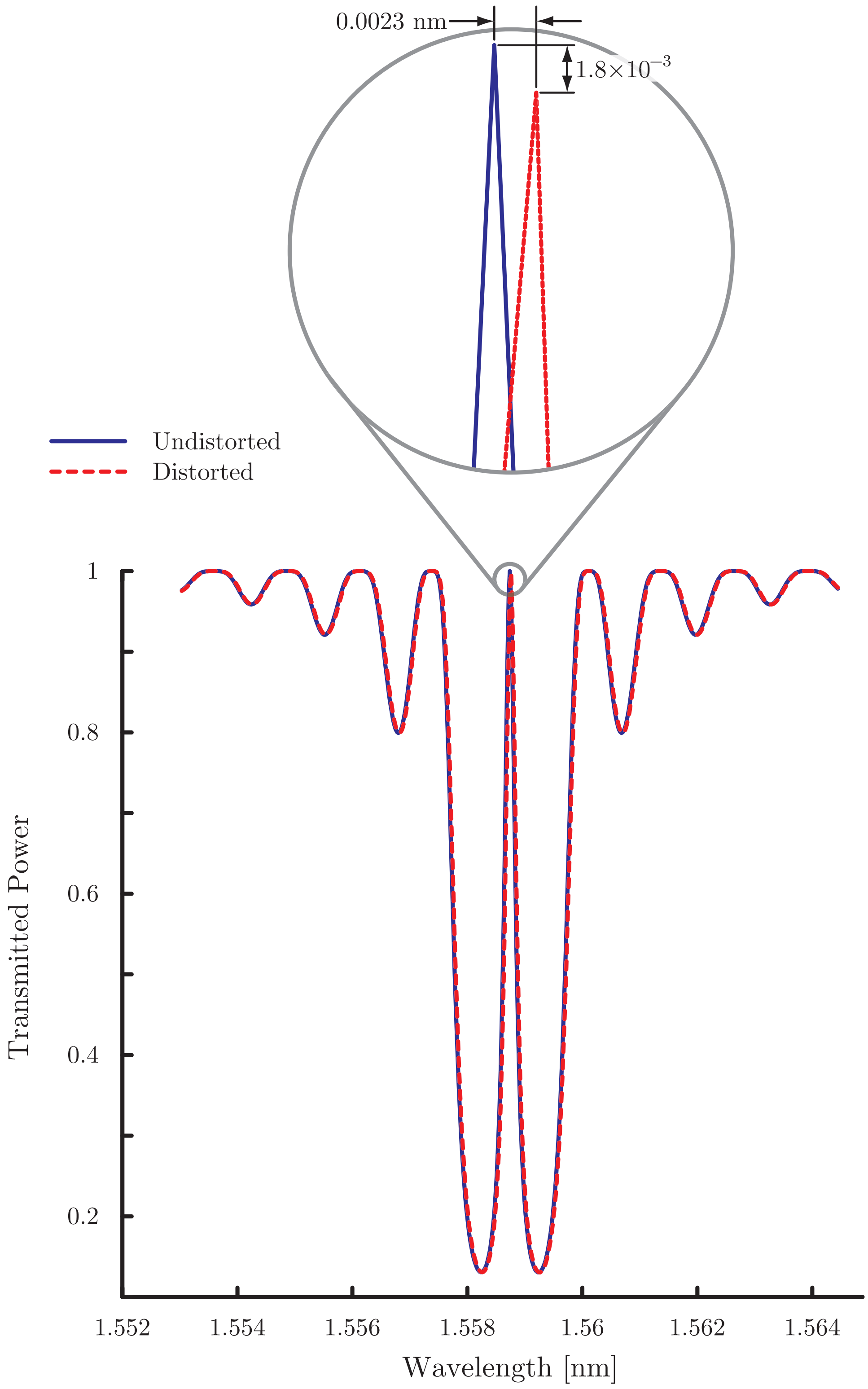

Figure 4-6: A comparison between an undistorted and distorted quarter-wave shifted Bragg grating. The quarter-wave shifted grating structure is very similar to the CDF gratings. Specifically the grating is located at the center of the die, is 600 μm long, and has a κ of 58 cm^{-1}. The distortion of the x-ray mask causes the peak to red-shift by 0.002 nm and the peak resonance to drop by 0.18%.

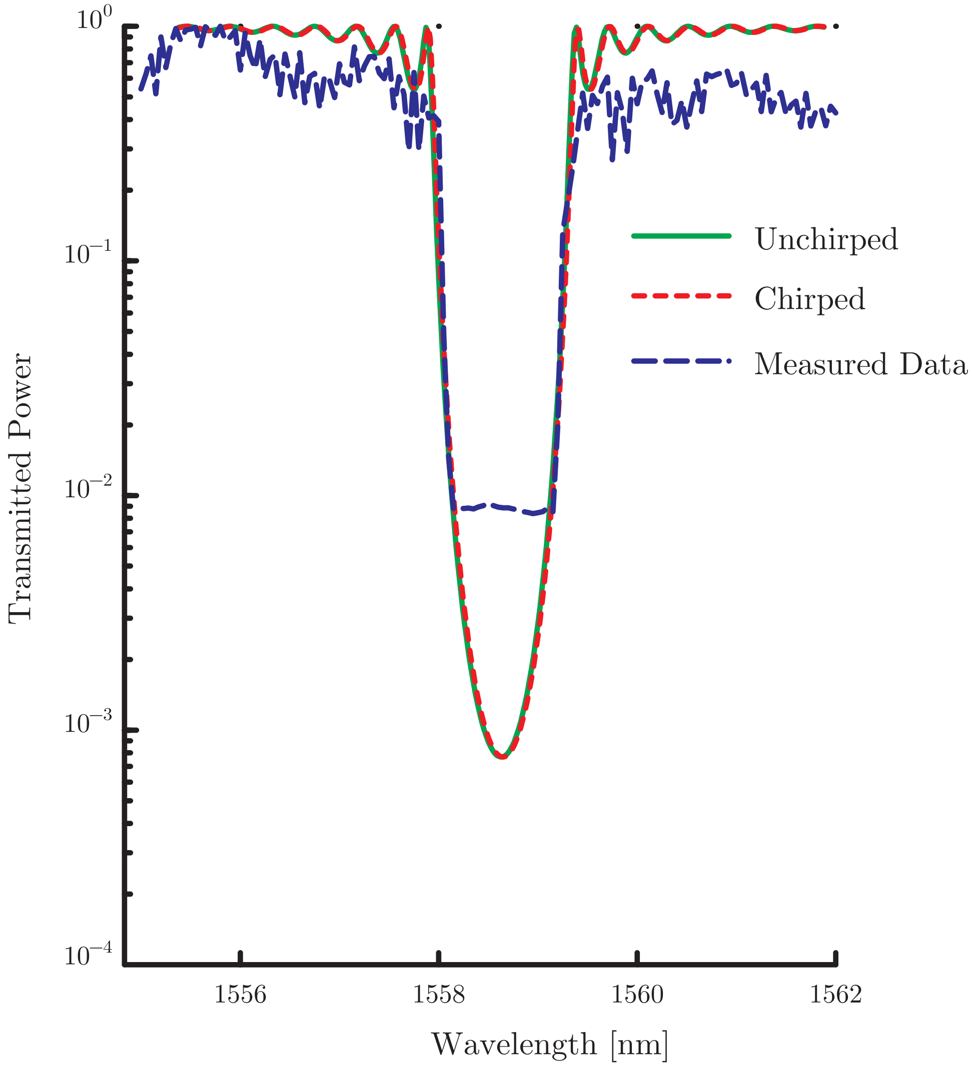

Figure 4-7: A transfer-matrix calculation of a DBR is overlaid on the measured results. The dotted line shows the spectrum after the grating is distorted using equation 4.5. The effect on the spectrum is similar to the quarter-wave shifted case, shown in figure 4-6, namely the spectrum shifted a little bit to longer wavelengths.

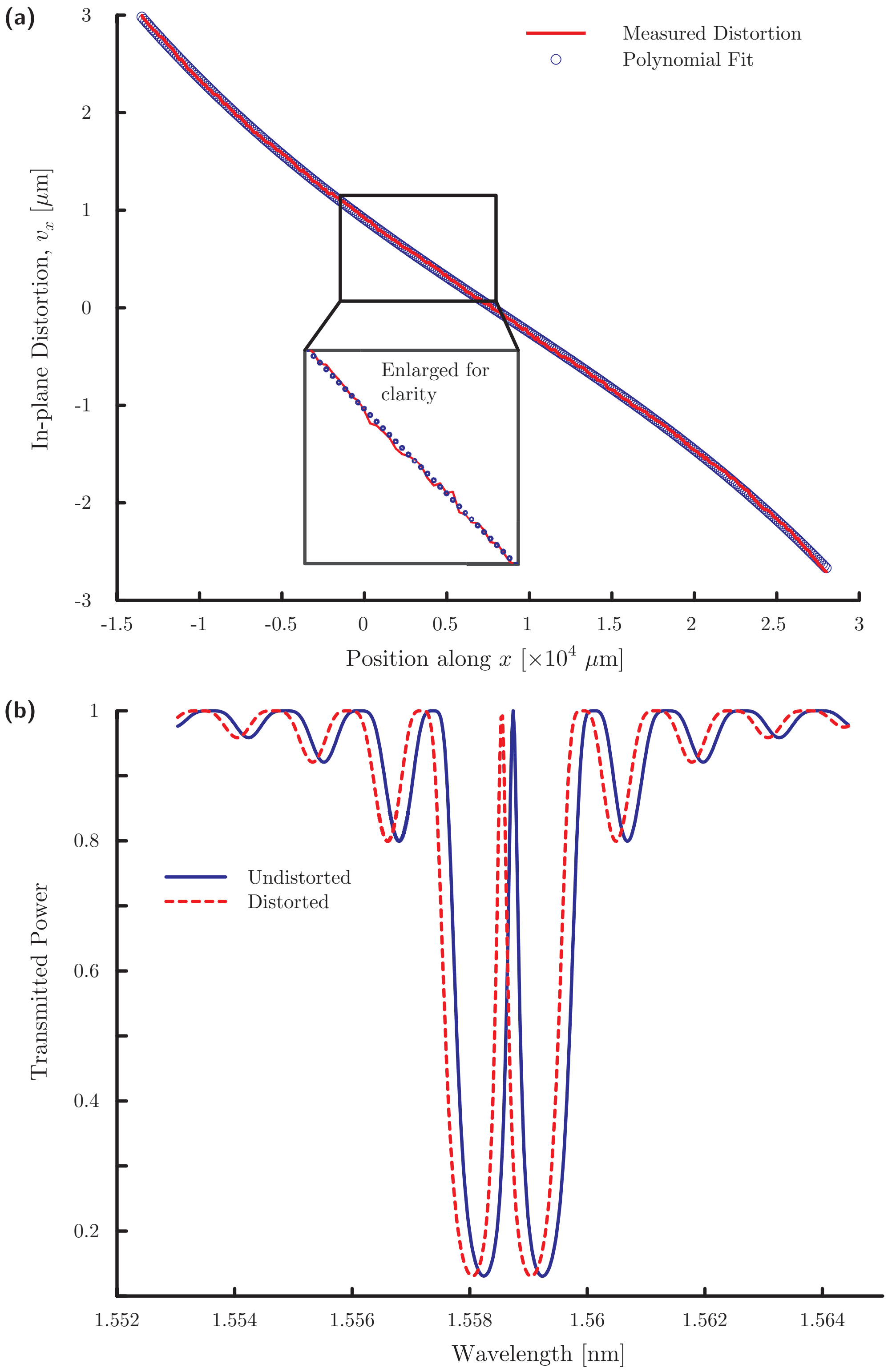

Figure 4-8: The effects of flip-bonding on the spectral response of the grating. (a) shows the polynomial fit to the IPD caused by the flip-bonding process. The distortion is significantly higher than that caused by the absorber stress. (b) shows the spectral response of a quarter-wave-shifted Bragg resonator. The dotted line shows the spectral alteration caused by the in-plane distortion. Even for this extreme distortion, the spectrum is surprisingly unaffected.

4.1.4 Spectral Effects of Other Fabrication Errors

There are other fabrication errors that can effect the spectral response of Bragg-grating-based devices. Fabrication errors impact the physical dimensions of the optical structure and not the periodicity as x-ray mask distortion does. The effects of these types of errors are generally well known—reference [63] is a good review. We briefly describe some of the more important effects below.

Duty-Cycle. The tooth-width to the trench-width is referred to as the duty-cycle, d, of the grating; *e.g.*, when $d = 0.5$ a grating has equal tooth and trench widths. A systematic change in the duty-cycle of the grating causes the spectrum to shift. This is due to the fact that the Bragg-grating period, $\Lambda = \lambda_0/2n_{\text{eff}}$, shifts because the effective index, n_{eff}, of the grating changes. Including d, the Bragg-grating period can be expressed as:

$$\Lambda = \frac{\lambda_0}{[d\, n_{\text{tooth}} + (1-d)n_{\text{trench}}]} \quad ,$$

where λ_0 is the free-space wavelength of interest.

Stitching Errors. Because the device gratings are longer than a single e-beam field, the pattern must be written by stitching together several fields. Damask [63] numerically modeled the effects of these random phase-shifts on the resonance-width and center-frequency of quarter-wave shifted (QWS) Bragg-grating devices. Based on certain assumption about the device parameters required, Damask found that the performance of a QWS Bragg-grating is not affected if the field-stitching error is kept below 5 nm.

Height/Width Errors. Systematic dimensional errors in the waveguide shift the center frequency of Bragg-grating devices by changing the effective index of the waveguide.

The list of fabrication errors above is by no means exhaustive, but does include the primary sources of error. Another potential source of error is material growth—epitaxial deposition of quaternary material with a well-controlled refractive index is difficult.

It is important that device design does not occur in a room sealed from the realities of lithography, fabrication, and growth. While the capabilities and techniques described in this thesis are powerful and flexible, they are not capable of producing devices of arbitrary precision. The remainder of this chapter discusses some work that was begun and promises to grow into some interesting future endeavors.

4.2 Distributed Feedback Lasers

In collaboration with Farhan Rana, of MIT's Semiconductor Laser Group, we began making InP-based distributed feedback (DFB) lasers. Figure 4-9 shows the result of a fabricated DFB laser and measured spectra; the beautiful polyimide planarization

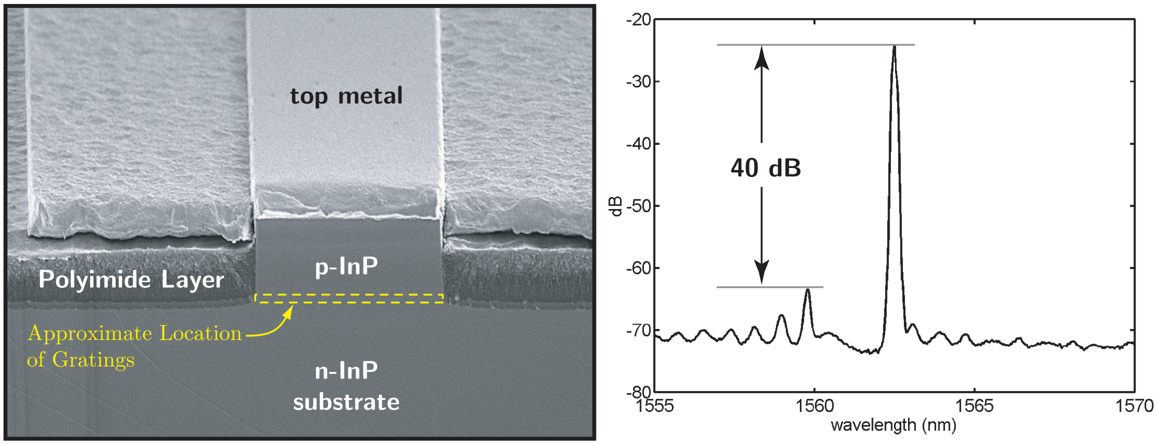

Figure 4-9: A DFB laser made with a combination of x-ray lithography and optical proximity lithography. The polyimide planarization process, developed by Farhan Rana, enabled the laser to operate at high frequency.

process was developed by Farhan Rana and enabled the laser to operate at very high speeds. In our efforts we were hampered by the polycrystalline nature of the MBE overgrowth. Once this material issue is worked out, a wide variety of DFB lasers and other active devices can be easily made. Currently, fiducial masks exist for grating periods of 244.4 nm, 245.2 nm, and 245.8 nm.

4.3 Sidewall Grating

The DLHP grating process can be altered slightly in order to produce sidewall gratings. Figure 4-10 illustrates the prototype altered process to produce sidewall and triwall gratings. In the first step, a thin mask layer of oxide is deposited onto the InP-based substrate. On top of this the device grating pattern is lifted off in a material such as chrome. The waveguide is patterned in photoresist. The excess chrome grating mask is etch away using a chlorine based etch chemistry. The photoresist pattern is eroded away using an unbiased oxygen plasm which reveals some of the chrome grating tooth. The photoresist and chrome grating tips are used as etch masks to etch into the oxide layer. The entire structure is then etched. If one wants gratings in the top of the waveguide, the photoresist is stripped and then one uses the chrome to etch through the underlying oxide and then into the substrate.

Figure 4-11a shows an example of a sidewall grating etched into InP. Figure 4-11b shows an example of the process producing gratings on all three sides of the waveguide. Figure 4-11c and 4-11d shows an example of a deeper triwall grating. Clearly surface roughness and etch profiles are not under control which indicates that this process is in the prototype stages and requires additional process development before use in actual devices.

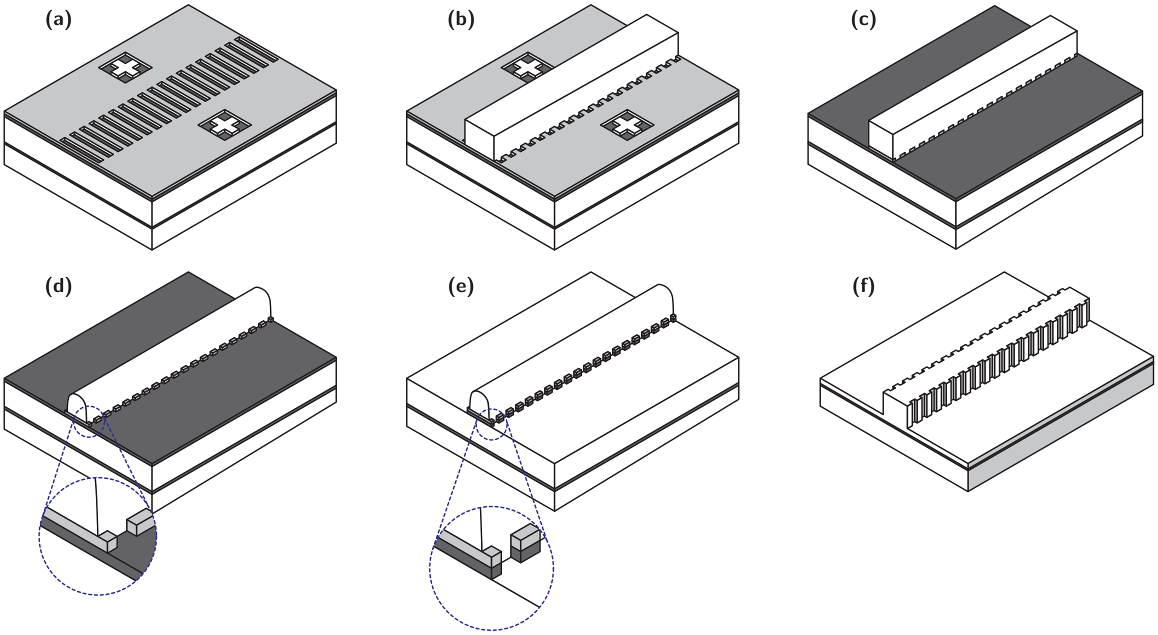

Figure 4-10: (a) The process begins with the device grating mask, possibly 50 nm of Cr, patterned on top of a thin film, possibly 50 nm of SiO_2. (b) The waveguide pattern, in photoresist, is placed appropriately. (c) The waveguide pattern is used to etch the excess Cr, possibly using a BCl_3/O_2 chemistry. (d) The waveguide pattern is eroded back, possibly using an O_2 RIE step. (e) The underlying film is patterned, using the photoresist in conjunction with the Cr grating mask, possibly using a CHF_3 RIE process. (f) The substrate is etched. To put gratings in the top as well, the photoresist should be stripped, which exposes the Cr grating, and the underlying film etched; the gratings can then be etched into the top of the waveguide. Figure 4-11 shows various examples of this prototype process.

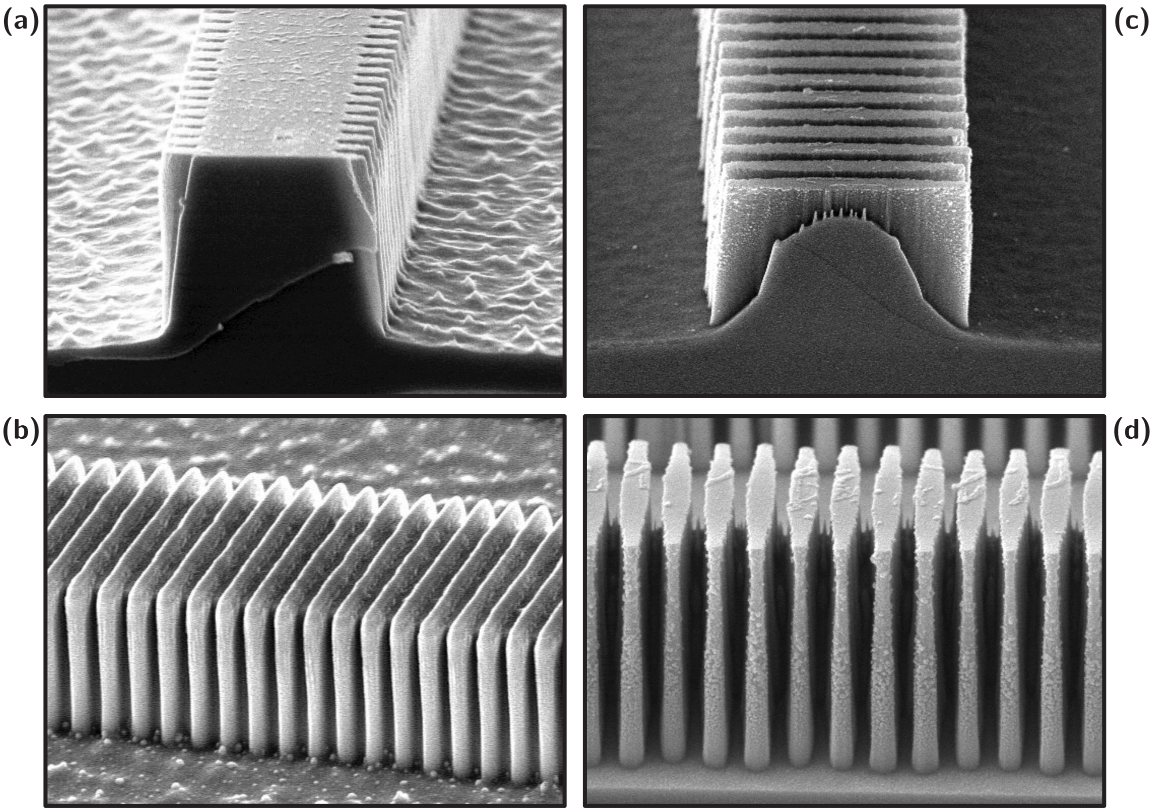

Figure 4-11: (a) shows an example of a sidewall grating etched into InP. (b) shows an example of the process producing gratings on all three sides of the waveguide. (c) and (d) shows an example of a deeper triwall grating. Clearly surface roughness and etch profiles are not under control.

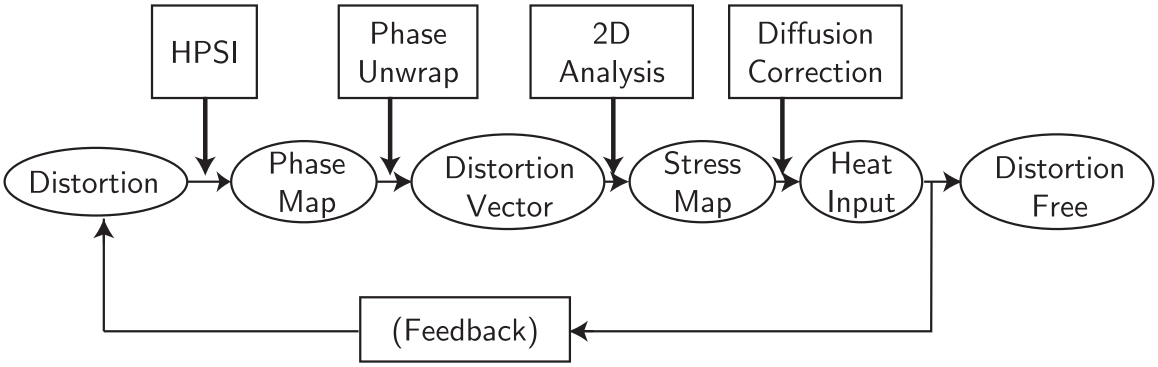

Figure 4-12: Flow chart outlining our iterative approach to eliminating distortion. First the HPSI acquires a phase map of the membrane. Next the data is translated into a distortion map. This map is then analyzed to calculate the causal stress map. Next, the heat distribution that will correct the stress map is calculated. Finally a 2D heating pattern is applied to the mask that should eliminate the distortion. The distortion is measured continuously by HPSI and, if not removed by the heat input, the sequence is iterated. Additionally, feedback can be used to control any time-dependent distortion.

4.4 Adaptive X-ray Mask

Figure 4-12 depicts a flow chart of the complete AXM approach. Each step requires less than a few seconds to complete. Therefore, this approach can work in real time, *i.e.* it can be made into an *in-situ* scheme. The AXM technique may provide other benefits as well. For example, since we no longer need a stiff, radiation-hard, membrane, or uniform low stress in the absorber, we can make use of thinner membrane materials and simpler, more economical processes for absorber deposition and patterning. These may provide increased throughput and reduce the cost of ownership.

A dedicated IL/HPSI system has been set up in the NSL, and is illustrated schematically in figure 4-13,. This system uses a simpler, and more robust, fringe locking system than the SNL system. Using this dedicated HPSI a 2D heat projection system should be developed in order to complete the AXM approach.

4.5 X-ray Lithography and Microphotonics

X-ray lithography is ideally suited for microphotonics. The major technical impediment to the successful use of the x-ray lithography in the semiconductor industry is the distortion in the x-ray mask. This issue is of much less concern for optical devices. The unique demands of the optical devices loosens the overlay requirements, and instead demands that high-fidelity gratings must be reproduced over long distances. Control over duty-cycle, *i.e.* improved process latitude, is much more important than ultimate feature size and overlay accuracy. The resolution and process control required to maintain proper duty-cycles and grating periods can easily be accomplished with the state-of-the-art x-ray lithography described in this dissertation.

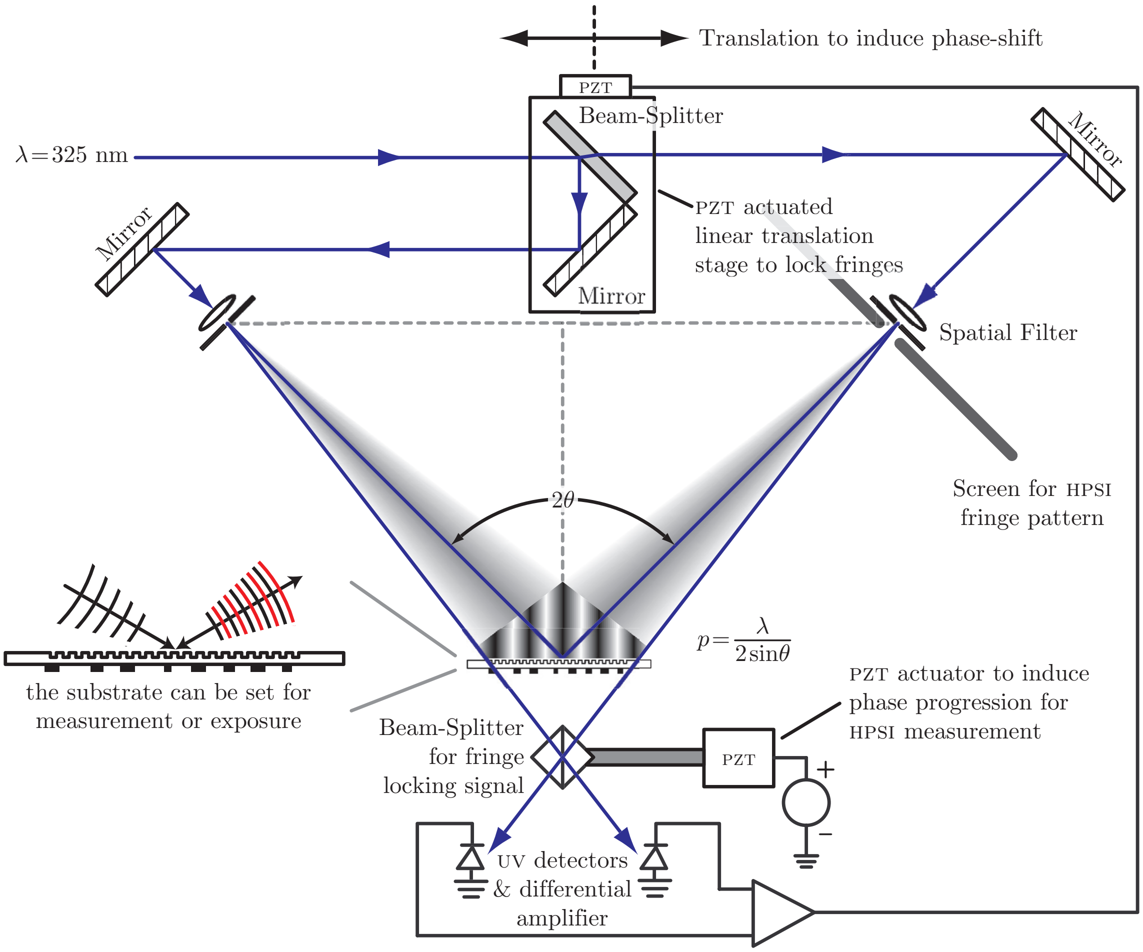

Figure 4-13: The final version of the IL/HPSI. The system uses a 325 nm He-Cd laser and a simpler fringe-locking system. Rather than a Pockels' cell, as in the SNL, the beam-splitter is moved back and forth. The additional mirror is required in the beam-splitter to insure that as the stage is translated back and forth, the beams do not translate.

Moreover, the primary concerns of x-ray lithography, *i.e.* the x-ray mask distortion, is not as significant a concern for optical devices. The DLHP for making microphotonics has much wider overlay tolerances than semiconductor processes for electronics. The studies have shown that the flip-bonded x-ray mask, with pellicle protection could be used to print microphotonics; ideally of course this mask configuration would be used in conjunction with the AXM system.

In conclusion, the state of microphotonics fabrication is at an exciting state. The fabrication tools and processes to build complicated devices have been developed and could conceivably go into a manufacturing environment.

Appendix A

Distortion Calculations

As mentioned previously, understanding x-ray membrane mask distortion is critical to the success of x-ray lithography. Specifically, we must understand the relationship between stress and distortion, *i.e.* to know the stress distribution that causes a measured distortion. Yanof *et al.* studied both IPD and out-of-plain distortion (OPD) caused by absorber stress [64]. However, their calculation was limited to a 1-dimensional (1D) model, and their OPD calculation used an unrealistic boundary condition to ease the analysis. One could also use finite element analysis to calculate the distortion that arises from a particular stress distribution. Unfortunately, the extreme aspect ratio of an x-ray mask membrane (*i.e.* 1 μm in thickness *vs* 31 mm in extent) gives most commercial solid modeling programs difficulty. Moreover, the reverse problem, calculating a causal stress pattern from a given distortion, is not possible in the finite element analysis.

Kenichi Murooka, a visiting scientist from Toshiba, developed an analytical technique that predicts both in-plane and out-of-plane distortion arising from an arbitrary stress distribution on a membrane surface. This technique can also solve the inverse problem; *i.e.*, it can predict the stress distribution which, when applied to any existing distortion, eliminates it. These techniques, based on the variational method, require one to formulate the total energy that results from the membrane distortion, which is a straightforward task even for complicated stress distributions. One then iteratively searches for the distortion map that minimizes this total energy, which, according to minimum energy principle, should be the true membrane distortion for a given stress distribution. The inverse problem is solved analytically by performing a functional minimization on the total energy and solving for the stress distribution. This calculational technique should enable us to correct for arbitrary distortions by, for example, applying another film or differentially heating.

This technique has been used throughout this dissertation and is therefore included in this appendix for convenience. In this section, we describe this analytical method to calculate the full 2-dimensional (2D) in-plane distortion from a given stress distribution. Then, the method is inverted to calculate the 2D stress distribution that would cause a given distortion distribution.

A.1 In-Plane Distortion from Stress

The most common way to model the distortions that arise due to stress is by employing a finite-element-based solid modeling system. Using such a system to model an x-ray mask membrane is fraught with difficulty due to its extreme aspect ratio; the membrane has a 30 mm diameter and 1 μm thickness. Rather than using an FEM system a variational method was adopted to calculate the IPD.

The basic concept of the variational method is that the real distortion is obtained when the total elastic energy as a function of distortion is minimized. The general formula for the energy ε of a unit volume of an isotropic solid is given as follows, using Young's modulus E and the Poisson ratio ν as two the elastic constants [65]:

$$\varepsilon = \frac{E}{2\,(1+\nu)}\left({u_{ik}}^2 + \frac{\nu}{1-2\nu}{u_{ll}}^2\right) \qquad , \tag{A.1}$$

where the generalized strain, u_{ik}, is:

$$u_{ik} = \frac{1}{2}\left(\frac{\partial u_i}{\partial x_k} + \frac{\partial u_k}{\partial x_i}\right). \tag{A.2}$$

The indices i, k, l each correspond to x, y, z and should be summed up in equation (A.1) and (A.2) according to the Einstein convention [1] . So writing equation A.1 out fully:

$$\begin{aligned}\varepsilon = \frac{E}{2(1+\nu)}\Bigg\{ & u_{xx}u_{xx} + u_{xy}u_{xy} + u_{xz}u_{xz} + \\ & u_{yx}u_{yx} + u_{yy}u_{yy} + u_{yz}u_{yz} + \\ & u_{zx}u_{zx} + u_{zy}u_{zy} + u_{zz}u_{zz} + \\ & \frac{\nu}{1-2\nu}\left(u_{xx}+u_{yy}+u_{zz}\right)^2 \qquad \Bigg\} \qquad .\end{aligned}$$

In the above relations, u_i is the component of a displacement vector in the i direction. The generalized strain tensor, u_{ik}, can be related to the generalized stress tensor, τ_{ik}, through Hooke's law:

$$\tau_{ij} = \lambda\delta_{ij}u_{kk} + 2\mu u_{ij}. \tag{A.3}$$

Where δ_{ij} is the Kronecker delta function and the Lamé constants are:

$$\begin{aligned}\lambda &= \frac{\nu E}{(1+\nu)(1-2\nu)} \\ \mu &= \frac{E}{2(1+\nu)} \qquad .\end{aligned}$$

---

[1] In the Einstein convention, repeated indices are summed. Therefore in equation (A.1), ${u_{ik}}^2$ represents the sum of nine terms (*i.e.* $u_{xx}u_{xx} + u_{xy}u_{xy} + u_{xz}u_{xz} + u_{yx}u_{yx} + u_{yy}u_{yy} + u_{yz}u_{yz} + u_{zx}u_{zx} + u_{zy}u_{zy} + u_{zz}u_{zz}$) and ${u_{ll}}^2$ represents $(u_{xx} + u_{yy} + u_{zz})^2$.

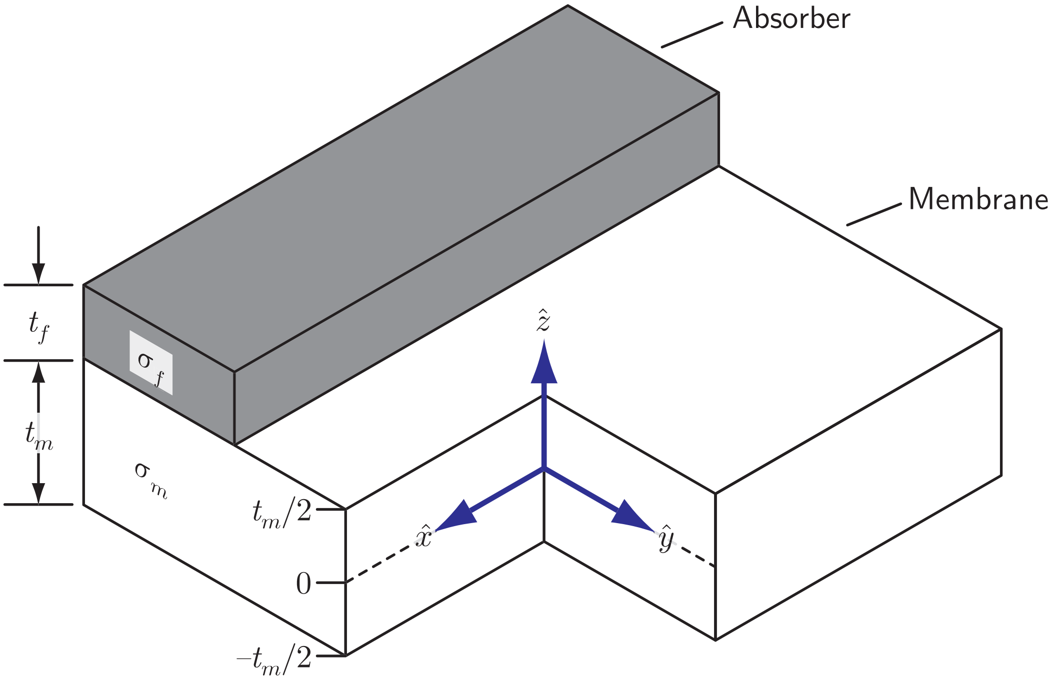

Figure A-1: In our analysis, the $x - y$ plane is taken to be the membrane's mid-plane. The z-axis is perpendicular to the membrane surface. The absorber has a thickness of t_f and a stress of σ_f. The membrane has a thickness of t_m and a stress of σ_m.

To determine the stress-to-distortion relationships x-ray mask membranes we separate the distortions into two types: those that occur within the $x-y$ plane (in-plane distortion) and those that occur along the z-axis (out-of-plane distortion). The above relationships are the launching point from which we will first derive the IPD energy and then the OPD energy. Figure A-1 illustrates the coordinate system used in the following analysis: the x-y plane is taken to be at the membrane's mid-plane while the z-axis is taken to be perpendicular to the membrane's surface.

In both cases we make the assumption that the stress of the absorber gives rise to forces that are in the $x - y$ plane, *i.e.* there are no forces perpendicular to the membrane surface. This means that:

$$\tau_{xz} = \tau_{zx} = \tau_{yz} = \tau_{zy} = \tau_{zz} = 0 \qquad , \tag{A.4}$$

which we can then use Hooke's law to write:

$$u_{yz} = u_{zy} = u_{zx} = u_{xz} = 0 \tag{A.5}$$

$$u_{zz} = -\frac{\nu}{1-\nu}\left(u_{xx} + u_{yy}\right) \qquad . \tag{A.6}$$

Substituting equation A.5 and A.6 into (A.1) we can write the IPD energy as:

$$\begin{aligned}\varepsilon_{IPD} = \frac{E}{2(1+\nu)}\Bigg\{ & \left[1+\frac{\nu^2}{(1-\nu)^2}\right]\left(u_{xx}^2+u_{yy}^2\right) \\ & + \frac{\nu^2}{(1-\nu)^2}2u_{xx}u_{yy}+u_{xy}^2+u_{yx}^2 \\ & + \frac{\nu}{1-2\nu}\left[\left(1-\frac{\nu}{1-\nu}\right)(u_{xx}+u_{yy})\right]^2\Bigg\} \qquad .\end{aligned}$$

After some algebra one can reduce the above expression down to:

$$\varepsilon_{IPD} = \frac{E}{2(1-\nu^2)}\left(u_{xx}^2+u_{yy}^2\right)+\frac{E\nu}{2(1-\nu^2)}2u_{xx}u_{yy}+\frac{E}{1+\nu}u_{xy}^2 \tag{A.7}$$

Of this distortion we want to account for the portion that is caused by the stress of the absorber. Since the absorber is amorphous, it has an isotropic stress-strain relationship, expressed as $\sigma = \frac{E}{1-\nu}$(strain). So we can write the relation between the macro and microscopic distortion as:

$$v_{ij} = \delta_{ij}u_{ij} - \sigma\frac{1-\nu}{E}$$

From the stress-strain relationship, we can substitute the following

$$\begin{aligned} u_{xx}^2 &= v_{xx}^2 + 2\sigma\frac{1-\nu}{E}v_{xx} + \left[\sigma\frac{1-\nu}{E}\right]^2 \\ u_{yy}^2 &= v_{yy}^2 + 2\sigma\frac{1-\nu}{E}v_{yy} + \left[\sigma\frac{1-\nu}{E}\right]^2 \\ u_{xx}u_{yy} &= v_{xx}v_{yy} + \sigma\frac{1-\nu}{E}v_{xx} + \sigma\frac{1-\nu}{E}v_{yy} + \left[\sigma\frac{1-\nu}{E}\right]^2 \qquad ,\end{aligned}$$

into equation A.7. Which we can then write as:

$$\varepsilon_{IPD} = \frac{E}{2(1-\nu^2)}\left[v_{xx}^2+v_{yy}^2+2\nu v_{xx}v_{yy}\right]+\sigma(v_{xx}+v_{yy})+\frac{E}{1+\nu}v_{xy}^2 \tag{A.9}$$

After substituting in equation A.2, the final formula is returned for the energy per unit volume for IPD:

$$\begin{aligned}\varepsilon_{IPD} = & \frac{E}{2\left(1-\nu^2\right)}\left\{\left(\frac{\partial v_x}{\partial x}\right)^2+\left(\frac{\partial v_y}{\partial y}\right)^2+2\nu\left(\frac{\partial v_x}{\partial x}\right)\left(\frac{\partial v_y}{\partial y}\right)\right\} \\ & +\sigma\left\{\left(\frac{\partial v_x}{\partial x}\right)+\left(\frac{\partial v_y}{\partial y}\right)\right\}+\frac{E}{4\left(1+\nu\right)}\left(\frac{\partial v_x}{\partial y}+\frac{\partial v_y}{\partial x}\right)^2 \qquad ,\end{aligned} \tag{A.10}$$

where v_x and v_y are the components of the distortion vector representing the IPD. We have rewritten u_x and u_y as v_x and v_y to distinguish macroscopic distortion from microscopic displacement after taking into account the offset due to the stress. The first and second terms inside the first pair of braces correspond to the stretching energy. The second term of equation (A.10) corresponds to the offset offset of stretching energy due to the stress. The third term corresponds to the shear energy in the $x-y$ plane.

Integrating equation (A.10) over the entire membrane area to sum up the total energy, *i.e.* $\iint \varepsilon_{IPD} dxdy$, and minimizing the total energy with respect to v_x and v_y gives the IPD. Note that this approach enables one to treat the general case where both E and σ are functions of x and y, which would be necessary to treat the case for an arbitrarily patterned absorber supported on a membrane.

Kenichi Murooka implemented this technique in MATLAB, using a steepest gradient search as the minimization technique. Figure A-2 shows an example of an IPD calculation. The membrane is a 10 mm-square shape of 1 μm-thick SiN$_x$ whose stress is 200 MPa tensile. The left half of the membrane is covered by a 0.3 μm-thick film whose stress is 10 MPa tensile. The calculating grid is 100×100, and the calculation took about 30 min. to calculate on a 300 MHz CPU machine. Figure A-2a shows a vector plot of the IPD. It appears that the boundary condition is properly taken into account. Figure A-2b shows the contour map of x-direction displacement v_x, and figureA-2c and A-2d show the cross-sections of this contour map. Clearly, a 1D model does not adequately represent the distortion, even in the central region.

A.2 Stress from In-Plane Distortion

In general, the inverse problem, *i.e.*, finding the stress that causes a given distortion, is much harder to solve. We can simplify the problem if we assume that any IPD induced by the OPD is relatively small, and can be neglected. With this assumption, we can apply a functional minimization to equation (A.10), the IPD energy, and arrive at the following set of differential equations:

$$\frac{\partial^2 v_x}{\partial x^2} + \frac{1-\nu}{2}\frac{\partial^2 v_x}{\partial y^2} + \frac{1+\nu}{2}\frac{\partial^2 v_y}{\partial x \partial y} = -\frac{1-\nu^2}{E}\frac{\partial \sigma}{\partial x} \tag{A.11}$$

$$\frac{\partial^2 v_y}{\partial y^2} + \frac{1-\nu}{2}\frac{\partial^2 v_y}{\partial x^2} + \frac{1+\nu}{2}\frac{\partial^2 v_x}{\partial x \partial y} = -\frac{1-\nu^2}{E}\frac{\partial \sigma}{\partial y} \tag{A.12}$$

We can calculate $\sigma(x,y)$ directly from equations (A.11) and (A.12) by integrating with respect to x and y, respectively, given v_x and v_y. However, to optimize the calculation time and accuracy, the equations are rewritten with $div \equiv \frac{\partial v_x}{\partial x} + \frac{\partial v_y}{\partial y}$ and $rot \equiv \frac{\partial v_y}{\partial x} - \frac{\partial v_x}{\partial y}$ as follows.

$$\frac{\partial div}{\partial x} - \frac{1-\nu}{2}\frac{\partial rot}{\partial y} = -\frac{1-\nu^2}{E}\frac{\partial \sigma}{\partial x} \tag{A.13}$$

$$\frac{\partial div}{\partial y} + \frac{1-\nu}{2}\frac{\partial rot}{\partial x} = -\frac{1-\nu^2}{E}\frac{\partial \sigma}{\partial y} \tag{A.14}$$

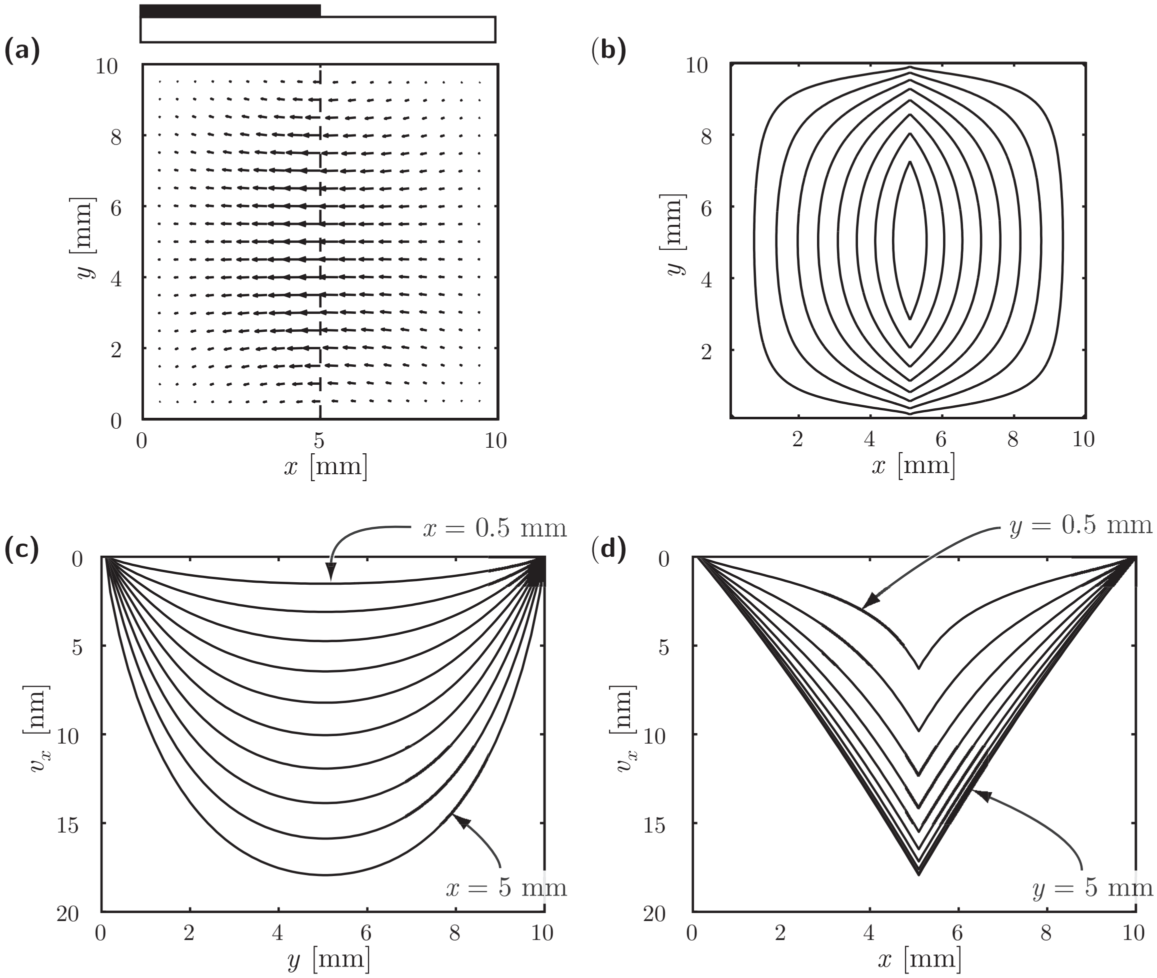

Figure A-2: In-plane distortion (IPD) calculation in a rectangular-membrane case. The SiN_x membrane has a 10 mm-square form and 1 μm thickness, with 200 MPa tensile stress. The absorber is 0.3 μm thick with 10 MPa tensile stress, and covers the left half of the membrane. (a)distortion vector map (b)contour map of v_x (c)cross-section of v_x contour map for various values of y (d)cross-section of v_x contour map for various values of x.

In solving equation (A.11), (A.12), (A.13) or (A.14) for σ, the integration of the second term is the hardest to handle due to the accumulations of errors. Since the second term of equation (A.13) or (A.14) is much smaller than that of equation (A.11) or (A.12), demonstrated in reference [34], using equations (A.13) and (A.14) requires less calculation time and provides sufficient accuracy.

A.3 Summary

A variational method was described for calculating the distortion of a membrane from a given stress distribution. In addition, we described a variational method for calculating the stress distribution that causes a given distortion distribution. We presented evidence that the inverse calculation is highly accurate. By solving this inverse problem we open the possibility of correcting stress-induced distortion of membranes, including the important problem of correcting distortion in membrane masks for nanolithography. Because the computation of the inverse problem can be carried out very rapidly, we open the possibility of real-time correction of membrane distortion. Because the method presented is analytical rather than numerical, arbitrarily complex membrane configurations and distortion distributions can be readily handled.

Appendix B

Anodic Bonding

Anodic bonding is a process that permanently fuses a metal (or semiconductor) surface to ion-doped glass [66, 67]. It produces extremely strong metal-glass seals that are irreversible [68]; silicon-glass seals are similarly strong and irreversible [33]. This phenomenon is commonly used in many practical disciplines, and has been explained in peer-reviewed journals [69, 70].

Configuration and Reactions

The term *anodic bonding* describes the fact that the process results in the anode, which is typically some metal or semiconductor, becoming bonded to the glass. In the most common anodic bonding configuration, shown in Figure B-1, the glass is negatively biased while the metal is set to ground. The anode is placed in contact to the glass. Heating the setup to $\geq 300\,^{\circ}\mathrm{C}$ begins the anodic bonding reaction.

The cations in the glass, typically Na^+, are fairly mobile at the elevated temperature and move towards the negative contact to combine with the electrons:

$$\mathrm{Na}^+ + \mathrm{e}^- \rightarrow \mathrm{Na} \quad . \tag{B.1}$$

This motion forms a depletion region close to the anode-glass interface. The extremely high electric fields in this depletion region drives the negatively charged oxygen ions to the anode surface. The reaction that takes place at the anode depends on anode type. A metal anode, considered non-blocking due to its high conductivity, forms a metal-oxide within the glass; this type of seal is very similar to the metal-glass seal that forms by high-temperature. It can be described by the reaction:

$$\mathrm{Me} \rightarrow \mathrm{Me}^{n+} + n\mathrm{e}^- \tag{B.2}$$

If the anode is silicon, considered blocking because of its relatively low conductivity, an SiO_2 bonding surface forms at the anode-glass junction. This reaction can be described by:

$$\mathrm{Si} + 2\mathrm{O}^{2-} \rightarrow \mathrm{SiO}_2 + 4\mathrm{e}^- \tag{B.3}$$

Figure B-2 summarizes the transfer of the ions and electrons during the reaction.

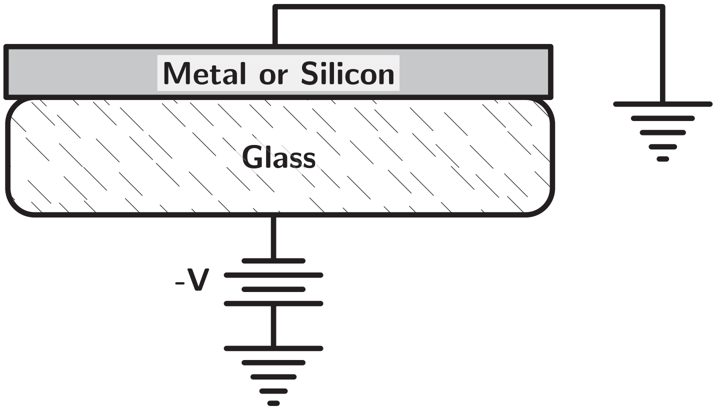

Figure B-1: The most common anodic bonding configuration involves placing a metal or silicon anode into intimate contact with glass and heating everything to $\geq 300\,^{\circ}$C. A large negative bias is placed across the metal-glass junction which induces a depletion region to form, shown in figure B-2, and begin the anodic bonding reaction.

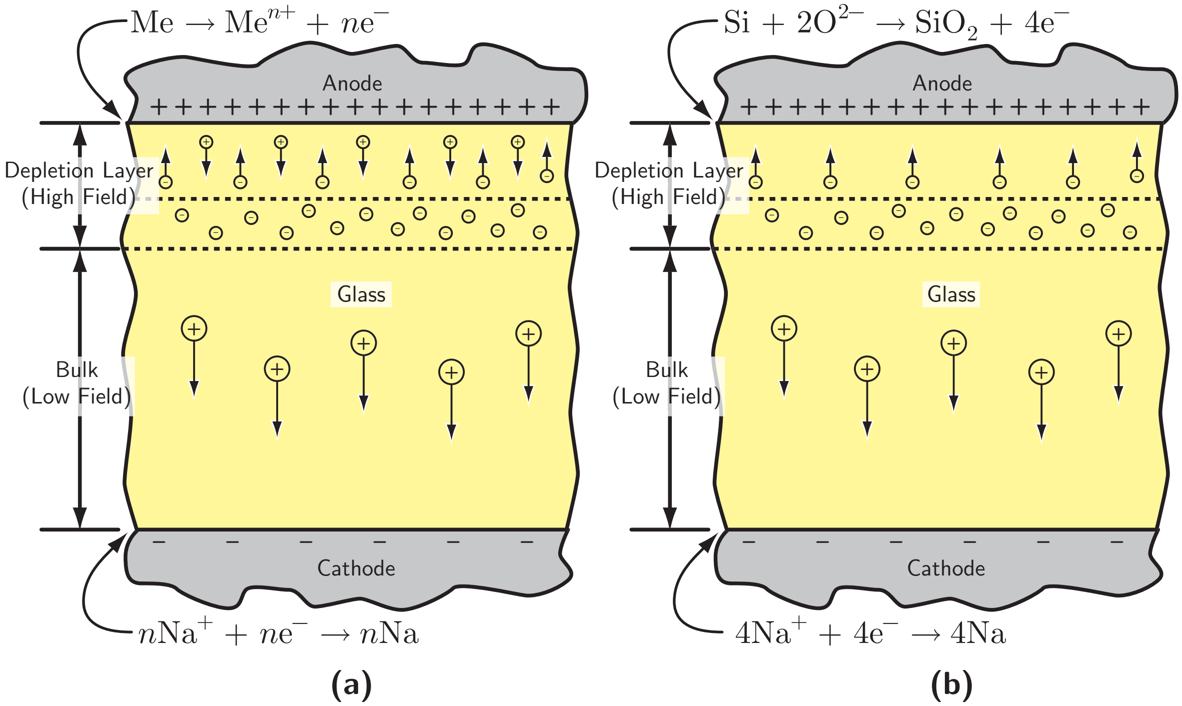

Figure B-2: This illustration of anodic bonding depicts the movement of charge in the system. (a) depicts the case of the non-blocking anode where metal-ions diffuse into the glass to form an oxide; the positive ions of the glass diffuse to plate on the surface of the cathode. (b) shows the case of the blocking anode where the oxygen anions diffuse to the surface of the anode to form the bonding silicon dioxide layer; similar to the non-blocking anode case, the cations from the glass diffuse to plate on the cathode. The possible electrochemical reactions for the cations and anions are shown.

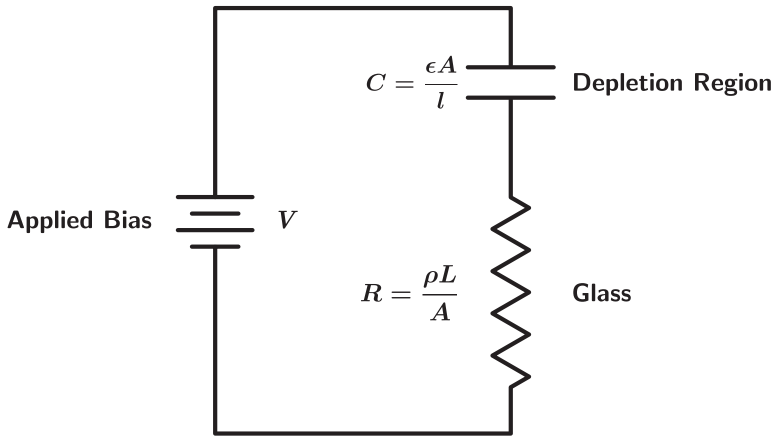

Figure B-3: The circuit model that is used to derive the rate relation for anodic bonding. The glass is represented as a resistance, R, that is dependent upon the anode area, A, and the length through the glass, L. The depletion region is represented as a capacitance, C, that is dependent upon A and the depth of the depletion region, l.

Rate Processes [70]

Figure B-3 shows the circuit model of the typical non-blocking anodic bonding configuration. The glass is a large resistor, with resistance R, and the depletion region is as a capacitor, with capacitance $C = \frac{\epsilon A}{l}$. R is determined by the glass' resistivity, ρ, [1] and the geometry of the system (*i.e.* the anode area, A, and the distance through the glass, L). C is determined by the dielectric constant, ϵ, the area, A, of the bonding region and the depth, l, of the depletion region. We can calculate the depth of the depletion region by realizing that the total charge being transferred, Q, is equal to the product of A, l, q (the charge of an electron), and p (the charge density within the depletion region). The capacitance related to the depletion region is

$$C = \frac{\epsilon A^2 pq}{Q} \quad . \tag{B.4}$$

From this relation, we can write the Kirchhoff relation as:

$$V - R\left(\frac{dQ}{dt}\right) - \frac{Q^2}{\epsilon A^2 p} = 0 \quad , \tag{B.5}$$

where V is the applied bias. After some manipulation, one can write describe the current using the relation:

$$I(t) = I_0 \mathrm{sech}^2(\zeta t) \tag{B.6}$$

where I_0 is the initial current, and normalized variable:

$$\zeta = \frac{V}{R\sqrt{\epsilon A^3 pV}} \quad , \tag{B.7}$$

---

[1] The log, base 10, of the resistivity, ρ, for Corning borosilicate glass type 7740 (commonly referred to as Pyrex) is approximately 6.9 Ωcm at 300°C.

	Area $[\mathbf{cm^2}]$	$\boldsymbol{L}$ $[\mathbf{cm}]$	**Resistance** $[\mathbf{k\Omega}]$	$\boldsymbol{I_0}$ $[\mathbf{mA}]$
Standard MIT Mask	12.08	0.2	132	11.4
Flip-Bonded Mask	3.85	0.2	413	3.6

Table B.1: A summary of the anodic bonding conditions for the standard MIT x-ray mask and the flip-bonded x-ray mask.

has been introduced. The initial current, I_0, is solely determined from the resistivity of the glass and the voltage since at $t = 0$ a capacitor acts like a short. Additionally, the length of the depletion region can be written:

$$l = \sqrt{\frac{\epsilon V}{p}\tanh(\zeta t)} \tag{B.8}$$

We are specifically interested in the bonding rates and characteristics for the standards MIT x-ray mask and the flip-bonded x-ray mask. The primary difference between the two cases is the bonding area, which is 12.08 cm^2 and 3.85 cm^2 for the standard MIT mask and the flip-bonded mask, respectively. Table B.1 summarizes the differences between the two x-ray mask configurations. The calculated I_0 for the standard MIT and flip-bonded x-ray mask is 11.4 mA and 3.5 mA, respectively, which is fairly close to the observed values during anodic bonding.

Figure B-4 shows the calculated time dependence of the current during anodic bonding. The graph shows that it takes approximately 5 seconds for the standard MIT x-ray mask to complete bonding, which compares well to observed bonding times. The calculation shows that the flip-bonded x-ray mask bonds in 3 seconds, which also compares favorably to observed bonding times.

Summary

The anodic bonding process is commonly used in making x-ray masks, as well as a host of other potentially useful objects and devices. It is also a well understood process, who's time dependence can be accurately modeled. This brief section discussed the chemical and rate processes of anodic bonding and related to the results that we see in the NSL. The model discussed above matches experimental results quite well and should take much of the uncertainty and guesswork out of anodically bonding new structures.

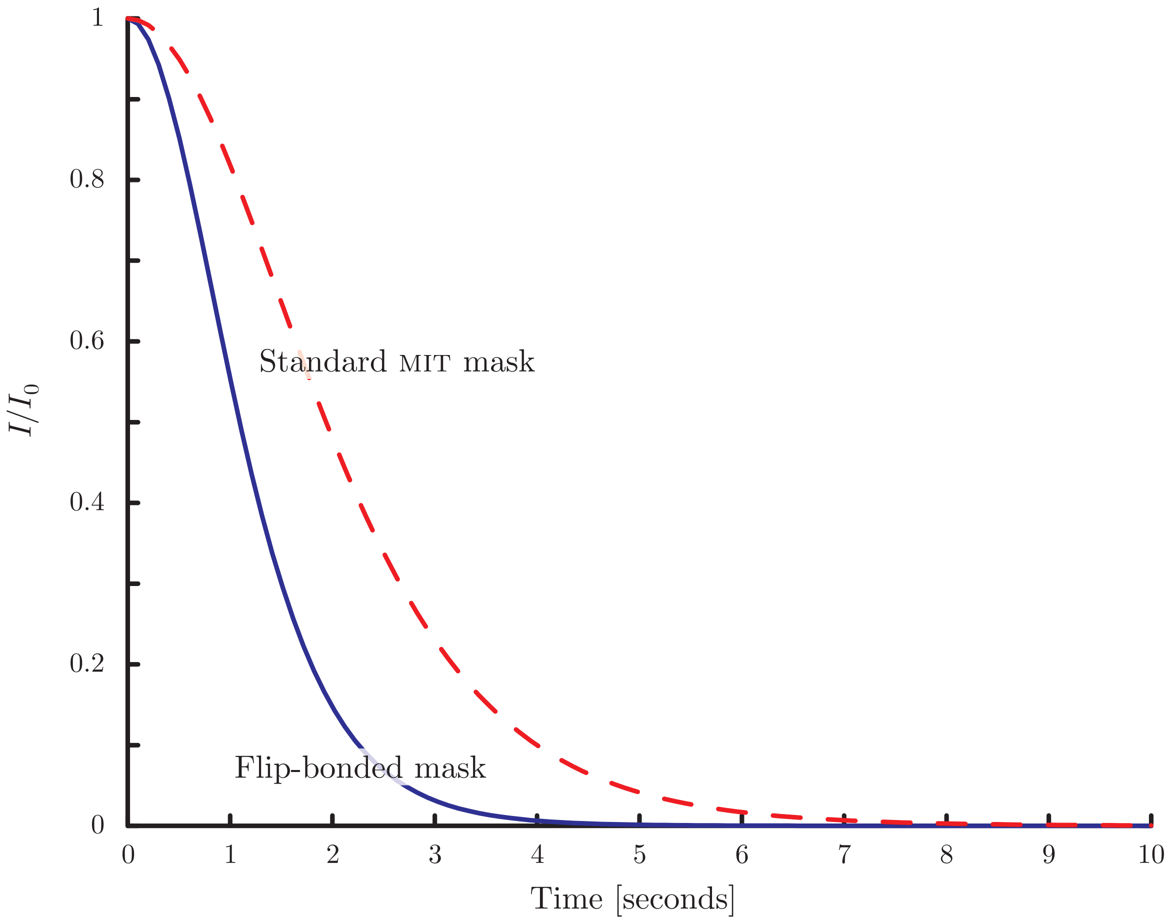

Figure B-4: A plot of equation B.6 using the values from table B.1. We assumed a charge density, ρ, of 2687 C/cm^2; this value takes into account both Na$^+$ and B$^+$ ions. The larger area of the standard MIT mask results in a slightly longer bonding time. Both time compare well to the observed bonding results.

Bibliography

[1] Khalid Ismail. *The Study of Electron Transport in Field-Induced Quantum Wells on GaAs/GaAlAs*. PhD thesis, Massachusetts Institute of Technology, June 1989. 1

[2] Chris Eugster. *Electron Waveguide Devices*. PhD thesis, Massachusetts Institute of Technology, June 1993. 1

[3] David Berman. *The Aluminum Single-Electron Transistor for Ultrasensitive Electrometry of Semiconductor Quantum-Confined Systems*. PhD thesis, Massachusetts Institute of Technology, June 1998. 1

[4] Partha P. Mitra and Jason B. Stark. Nonlinear limits to the information capacity of optical fibre communications. *Nature*, 411(6841):1027–1030, June 2001. 1

[5] Drowning in glass. *The Economist*, 22 March 2001. 1

[6] H. Kogelnik and C. V. Shank. Coupled-wave theory of distributed feedback lasers. *Journal of Applied Physics*, 453(5):2327–2335, May 1972. 1

[7] Andreas Othonos. Fiber bragg gratings. *Review of Scientific Instruments*, 68(12):4309–4628, Decemeber 1997. 1, 3

[8] H. A. Haus and Y. Lai. Theory of cascaded quarter wave shifted distributed feedback resonators. *IEEE Journal of Quantum Electronics*, 28(1):205–213, January 1992. 1

[9] V. V. Wong, Juan Ferrera, J. N. Damask, T. E. Murphy, Henry I. Smith, and H. A. Haus. Distributed bragg grating integrated-optical filters: synthesis and fabrication. *Journal of Vacuum Science and Technology B*, 13(5):2859–2864, November/December 1995. 1, 3.3.1, 3.3.1

[10] Y. Oowaki, M. Noguchi, S. Takagi, D.Takashima, M. Ono, Y. Matsunaga, K. Sunouchi, H. Kawaguchiya, S. Matsuda, M. Kamoshida, T. Fuse, S. Watanabe, A. Toriumi, S. Manabe, and A. Hojo. A sub-0.1 μm circuit design with substrate-over-biasing CMOS logic. In *IEEE International Solid-State Circuits Conference. Digest of Technical Papers*, pages 88–89, 1998. 1

[11] E. Toyota, T. Hori, M. Khan, and F. Cerrina. A new technique for 25 nm x-ray nanolithography. In *Electron, Ion, and Photon Beam and Nanofabrication Conference*, 2001. 1

[12] Juan Ferrera. *Nanometer-Scale Placement in Electron-Beam Lithography*. PhD thesis, Massachusetts Institute of Technology, June 2000. 1, 2.3.1, 8, 3.3.1

[13] Henry I. Smith. Japan could dominate industry with x-ray lithography. *Semiconductor International*, February 2001. 2

[14] S. Uchiyama, M. Oda, and T. Matsuda. X-ray mask distortion correction technology using pattern displacement simulator. *Journal of Vacuum Science and Technology B*, 14(6):4332–4335, Nov/Dec 1996. 2

[15] Toyoki Kitayama, Kenji Itoga, Yutaka Watanabe, and Shunichi Uzawwa. Proposal for a 50 nm proximity x-ray lithography system and extension to 35 nm by resist material selection. *Journal of Vacuum Science and Technology B*, 18(6):2950–2954, November/December 2000. 3

[16] M. Feldman. Thermal compensation of x-ray mask distortions. *Journal of Vacuum Science and Technology B.*, 17(6):3407–3410, Nov/Dec 1999. 4, 2.4

[17] B. L. Henke, E. M. Gullikson, and J. C. Davis. X-ray interactions: Photoabsorption, scattering, transmission, and reflection at E=50–30,000 ev, z=1–92. *Atomic Data and Nuclear Tables*, 54(2):181–342, 1993. 2.1.1

[18] P. A. Pella, Liangyuan Feng, and J. A. Small. An analytical algorithm for calculation of spectral distributions of x-ray tubes for quantitative x-ray fluorescence analysis. *X-Ray Spectrometry*, 14(3):125–135, 1985. 3

[19] William Chu. *Inorganic X-ray Mask Technology for Quantum-Effect Devices*. PhD thesis, Massachusetts Institute of Technology, May 1993. 3

[20] Y. Diawara, H. Lafontaine, M. Chaker, J.C. Keiffer, H. Pèpin, R.W. Cochrane, J.F. Currie, A.M. Haghiri-Gosnet, M.F. Ravet, and F. Rousseaux. Rapid thermal annealing for reducing stress in tungsten x-ray mask absorber. *Journal of Vacuum Science and Technology B*, 11(2):296–300, March/April 1993. 1

[21] Y.C. Ku. *Fabrication of Distortion Free X-ray Masks using Low Stress Tungsten*. PhD thesis, Massachusetts Institute of Technology, October 1991. 2.2.1

[22] Mark Mondol, Huiying Li, Gabrielle Owen, and Henry I. Smith. Uniform-stress tungsten on x-ray mask membranes via he-backside temperature homogenization. *Journal of Vacuum Science and Technology B*, 12(6):4024–4027, November/Decemebr 1994. 2.2.1

[23] Gabrielle Owen. Optical and mechanical characterization of thin membranes for x-ray lithography. Master's thesis, Massachusetts Institute of Technology, 1994. 2.2.1

[24] Y. C. Ku, Michael H. Lim, J. M. Carter, M. K. Mondol, A. Moel, and Henry I. Smith. Correlation of in-plane and out-of-plane distortion in x-ray lithography masks. *Journal of Vacuum Science and Technology B.*, 10(6):3169–3172, Nov/Dec 1992. 2.2.1, 2.3

[25] Scott Hector, Victor Pol, Azalia Krasnoperova, Juan Maldonado, Alex Flamholz, Dave Heald, Carl Stahlhammer, Dan Galburt, Ralph Amodeo, Tom Donohue, Shalom Wind, James Buchigniano, Raman Viswanathan, Mumit Khan, Srinivas Bollepalli, and Franco Cerrina. X-ray lithography for ≤ 100 nm ground rules in complex patterns. *Journal of Vacuum Science and Technology B*, 15(6):2517–2521, November 1997. 2.2.2

[26] J. H. Bruning, D. R. Herriott, J. E. Gallagher, D. P. Rosenfeld, A. D. White, and D. J. Brangaccio. Digital wavefront measuring interferometer for testing optical surfaces and lenses. *Applied Optics*, 13(11):2693–2703, November 1974. 2.3

[27] J. Ferrera, M. L. Schattenburg, and Henry I. Smith. Analysis of distortion in interferometric lithography. *Journal of Vacuum Science and Technology B.*, 14(6):4009–4013, Nov/Dec 1996. 2.3

[28] P. Hariharan, B. F. Oreb, and T. Eiju. Digital phase-shifting interferometry: a simple error-compensating phase calculation algorithm. *Applied Optics*, 26(13):2504–2505, July 1997. 2.3

[29] K. G. Larkin and B. F. Oreb. Design and assessment of symmetrical phase-shifting algorithms. *Journal of the Optical Society of America A*, 9(10):1740–1748, October 1992. 2.3

[30] R.M. Goldstein, H.A. Zebker, and C.L. Werner. Satellite radar interferometry: two-dimensional phase unwrapping. *Radio Science*, 23(4):713–720, 1988. 2.3

[31] R. Ruby, D. Baldwin, and M. Karnezos. The use of diffraction techniques for the study of in-plane distortions of x-ray masks. *Journal of Vacuum Science and Technology B.*, 5(1):272–277, Jan/Feb 1987. 2.3

[32] M. L. Schattenburg, R. J. Aucoin, and R. C. Fleming. Optically matched trilevel resist process for nanostructure fabrication. *Journal of Vacuum Science and Technology B*, 13(6):3007–3011, Nov/Dec 1995. 2.3.1

[33] Kevin B. Albaugh. Electrode phenomena during anodic bonding of silicon to sodium borosilicate glass. *Journal of the Electrochemical Society*, 138(10):3089–3094, October 1991. 2.3.1, B

[34] Kenichi Murooka, Michael H. Lim, and Henry I. Smith. Calculational study on membrane mask distortion and correction. *Journal of Vacuum Science and Technology B*, 19, 2001. to be publish. 5, A.2

[35] Kenichi Murooka, Michael H. Lim, and Henry I. Smith. The effect of thermal diffusion on a membrane-mask-distortion correction and compensation method. *Journal of Vacuum Science and Technology B*. submitted. 2.4.2

[36] B. Gates, S.H. Park, and Y. Xia. Self-assembly of colloidal particles into three-dimensionally ordered arrays and its applications. In *Proceedings of* SPIE, volume 3937, pages 36–43, 2000. 3

[37] Thomas E. Murphy. *Design, Fabrication and Measurement of Integrated Bragg Grating Optical Filters*. PhD thesis, Massachusetts Institute of Technology, February 2001. 1, 4.1, 4.1.2, 10, 10, 4-4

[38] H. A. Haus and Y. Lai. Narrow-band optical channel-dropping filter. *Journal of Lightwave Technology*, 10(1):57–62, January 1992. 7

[39] Juan Ferrera, J. N. Damask, V. V. Wong, H. I. Smith, and H. A. Haus. High-coherence qws gratings for optoelectronic devices: why spatial-phase-locked e-beam lithography is necessary. In *Optical Fiber Communications Technical Digest*, pages 139–141, 1994. 8

[40] Juan Ferrera. Highly coherent gratings for optoelectronics: An application of spatial-phase-locked electron beam lithography. Master's thesis, Massachusetts Institute of Technology, 1994. 8

[41] Chemical Rubber Company. *CRC handbook of chemistry and physics*. Cleveland Chemical Rubber Publishing Co., 1994. 3.1

[42] R. H. Burton and G. Smolinsky. CCl_4 and Cl_2 plasma etching of III-V semiconductors and the role of added O_2. *Journal of Electrochemical Society*, 129(7):1599–1604, July 1982. 3.2.1

[43] R. A. Gottscho, G. Smolinsky, and R. H. Burton. Carbon tetrachloride plasma etching of GaAs and InP: a kinetic study utilizing nonperturbative optical techniques. *Journal of Applied Physics*, 53(8):5908–5919, August 1982. 3.2.1

[44] R. A. Barker, T. M. Mayer, and R. H. Burton. Surface composition and etching of III-V semiconductors in Cl_2 ion beams. *Applied Physics Letters*, 40(7):583–586, 1 April 1982. 3.2.1

[45] E. L. Hu and R. E. Howard. Reactive-ion etching of GaAs and InP using $CCl_2F_2/Ar/O_2$. *Applied Physics Letters*, 37(11):1022–1024, December 1980. 3.2.1

[46] D. L. Flanders, L. D. Pressman, and G. Pinelli. Reactive ion etching of indium compounds using iodine containing plasmas. *Journal of Vacuum Science and Technology B*, 8(6):1990–1993, November 1990. 3.2.1

[47] U. K. Chakrabarti, S. J. Pearton, A. Katz, W. S. Hobson, and C. R. Abernathy. Dry etching of III-V semiconductors in CH_3I, C_2H_5I, and C_3H_7I discharges. *Journal of Vacuum Science and Technology B*, 10(6):2378–2385, November 1992. 3.2.1

[48] U. Niggebrugge, M. Klug, and Garus. A novel process for reactive ion etching on inp, using CH_4/H_2. In Adam Hilger, editor, *Gallium Arsenide and Related Compounds 1985. Proceedings of the Twelfth International Symposium.*, pages 367–372, 1986. 3.2.1

[49] D. L. Melville, J. Budinavicius, D. A. Thomson, and J. G. Simmons. Volatile products and endpoint detection in reactive ion etching of III-V compounds with a broad beam ECR source. *Nuclear Instruments and Methods in Physics Research B—Beam Interactions with Materials and Atoms*, B106(1–4):179–182, December 1995. 3.2.1, 3.2

[50] D. L. Melville, J. G. Simmons, and D. A. Thompson. Identification of volatile products in low pressure hydrocarbon electron cyclotron resonance reactive ion etching of inp and gaas. *Journal of Vacuum Science and Technology B*, 11(6):2038–2045, 1993. 3.2.1, 3.2

[51] E. M. Koontz, M. H. Lim, V. V. Wong, G. S. Petrich, L. A. Kolodzieski, Henry I. Smith, K. M. Matney, G. D. U'Ren, and M. S. Goorsky. Preservation of rectangular-patterned inp gratings overgrown by gas source molecular beam epitaxy. *Applied Physics Letters*, 71(10):1400, September 1997. 3.2.2

[52] Elisabeth Marley Koontz. PhD thesis, Massachusetts Institute of Technology, 1999. *The author feels that some of results contained in this reference are erroneous, but includes it for completeness.* 3.2.2, 3.2.2, 3.2.2

[53] Jalal Khan. Private communications. 3.2.2

[54] K. D. Choquette, R. J. Shul, A. J. Howard, D. J. Rieger, R. S. Freund, and R. C. Wetzel. Smooth reactive ion etching of GaAs using a hydrogen plasma pretreatment. *Journal of Vacuum Science and Technology B*, 13(1):40–42, January 1995. 3.2.2, 3.2.2

[55] S.J. Pearton, J.W. Lee, E.S. Lambers, C.R. Abernathy, F. Ren, W.S. Hobson, and R.J. Shul. Comparison of dry etching techniques for III-V semiconductors in ch_4/h_2/ar plasmas. *Journal of Electrochemical Society*, 143(2):752–758, February 1996. 3.2.2, 3.2.2

[56] J. E. Parmeter, R. J. Shul, A. J. Howard, and P. A. Miller. Treatment of inp surfaces in radio frequency H_2 and $H_2/CH_4/Ar$ plasmas: *In situ* compositional analysis, etch rates, and surface roughness. *Journal of Vacuum Science and Technology B*, 14(6):3563–3574, November 1996. 3.2.2, 3.2.2

[57] Charles Joyner. Private communications. 3.2.2, 3.2.2

[58] V. V. Wong, Juan Ferrera, J. N. Damask, J. M. Carter, E. E. Moon, H. A. Haus, Henry I. Smith, and S. Rishton. Spatial-phase-locked electron-beam lithography and x-ray lithography for fabricating first-order gratings on rib waveguides. *Journal of Vacuum Science and Technology B*, 12(6):3741–3745, November/December 1994. 3.3.1

[59] Juan Ferrera, V. V. Wong, S. Rishton, V. Boegli, E. H. Anderson, D. P. Kern, and H. I. Smith. Spatial-phase-locked electron-beam lithography: initial test results. *Journal of Vacuum Science and Technology B*, 11(6):2342–2345, November/December 1993. 3.3.1

[60] M. Jalal Khan. *To be determined*. PhD thesis, Massachusetts Institute of Technology. To be published. 3.4, 4.1.3

[61] Larry Coldren. *Semiconductor Lasers*. Wiley Interscience, 1999. 1

[62] Hermann A. Haus. *Waves and Fields in Optoelectronics*. Prentice-Hall, 1984. 10

[63] Jay N. Damask. *Integrated-Optic Grating-Based Filters for Optical Communication Systems*. PhD thesis, Massachusetts Institute of Technology, May 1996. 4.1.4

[64] A. W. Yanof, D. J. Resnik, C. A. Jankoshi, and W. A. Johnson. Electron-beam, x-ray, and ion-beam techniques for submicrometer lithographies V. In *Proceedings of the SPIE*, page 118, 1986. A

[65] L. D. Landau and E. M. Lifshitz. *Theory of Elasticity*. Pergamon Press Ltd., 1959. A.1

[66] Danieal I. Pomerantz. Anodic bonding. *United States Patent 3,397,278*, August 1968. B

[67] Daniel I. Pomerantz, George Wallis, and John J. Dorsey. Bonding electrically conductive metals to insulators. *United States Patent 3,417,459*, December 1968. B

[68] Kevin B. Albaugh. Irreversibility of anodic bonding. *Materials Letters*, 4(11):465–469, October 1986. B

[69] P. B. DeNee. Low energy metal-glass bonding. *Journal of Applied Physics*, 40(13):5396–5397, December 1969. B

[70] Kevin B. Albaugh and D. H. Rasmussen. Rate processes during anodic bonding. *Journal of the American Ceramics Society*, 75(10):2644–2648, October 1992. B, B